

From Pebbles and Planetesimals to Planets and Dust: the Protoplanetary Disk–Debris Disk Connection

JOAN R. NAJITA,¹ SCOTT J. KENYON,² AND BENJAMIN C. BROMLEY³

¹*NSF’s NOIRLab, 950 N. Cherry Avenue, Tucson, AZ 85719, USA*

²*Smithsonian Astrophysical Observatory, 60 Garden Street, Cambridge, MA 02138, USA*

³*Department of Physics & Astronomy, University of Utah, 201 JFB, Salt Lake City, DC 20006, USA*

(Received 5 August 2021; Revised 15 October 2021; Accepted 5 November 2021)

Submitted to ApJ

ABSTRACT

The similar orbital distances and detection rates of debris disks and the prominent rings observed in protoplanetary disks suggest a potential connection between these structures. We explore this connection with new calculations that follow the evolution of rings of pebbles and planetesimals as they grow into planets and generate dusty debris. Depending on the initial solid mass and planetesimal formation efficiency, the calculations predict diverse outcomes for the resulting planet masses and accompanying debris signature. When compared with debris disk incidence rates as a function of luminosity and time, the model results indicate that the known population of bright cold debris disks can be explained by rings of solids with the (high) initial masses inferred for protoplanetary disk rings and modest planetesimal formation efficiencies that are consistent with current theories of planetesimal formation. These results support the possibility that large protoplanetary disk rings evolve into the known cold debris disks. The inferred strong evolutionary connection between protoplanetary disks with large rings and mature stars with cold debris disks implies that the remaining majority population of low-mass stars with compact protoplanetary disks leave behind only modest masses of residual solids at large radii and evolve primarily into mature stars without detectable debris beyond 30 au. The approach outlined here illustrates how combining observations with detailed evolutionary models of solids strongly constrains the global evolution of disk solids and underlying physical parameters such as the efficiency of planetesimal formation and the possible existence of invisible reservoirs of solids in protoplanetary disks.

Keywords: protoplanetary disks — debris disks — planet formation — planetesimals — circumstellar matter

1. INTRODUCTION

Stars form surrounded by disks, the material from which planets form. Over the first Myr (or so) in the life of a disk, its solids are aggregated into planetesimals and protoplanets, and eventually into planets. The first step in this transformation may be hastened as disk solids collect in inhomogeneities—ring-like pressure bumps and other features—triggering processes such as the streaming instability, which create planetesimals. The planetesimals eventually grow into planets, which shape the disk gas and dust, producing rings, gaps, inner holes, and other structures. The concentration of solids in rings may spur further planetesimal (and planet) formation. After the disk gas dissipates, residual planetesimals “left behind” in the planet formation process may eventually reveal themselves, as they collide and produce disks of debris that glow in the reprocessed light from the central star.

Some of the most dramatic evidence in support of this picture comes from the millimeter continuum morphologies of Class II (protoplanetary) disks, many of which show the substructure that forming planets are expected to induce. When imaged at millimeter wavelengths and in scattered light, large disks (radii $\gtrsim 25$ –30 au) show rings, gaps, central cavities, and other features at distances of 20–200 au from the star (e.g., [Avenhaus et al. 2018](#); [Huang et al. 2018](#); [Long et al. 2019](#); [Cieza et al. 2019](#), and references therein). While central cavities have been imaged for more than a

decade (e.g., Andrews et al. 2010; Andrews 2015), the realization that narrow rings and gaps are common features of disks at large radii is a discovery of the ALMA era (ALMA Partnership et al. 2015). Whereas disk central cavities are thought to be created by a high mass giant planet that orbits within the cavity, the narrow rings and gaps can be created by lower mass (approximately Neptune-mass) planets (e.g., Bae et al. 2018; Lodato et al. 2019).

Emission associated with orbiting gas giant planets has also been detected in disks with central cavities through direct imaging techniques (Sallum et al. 2015; Keppler et al. 2018; Haffert et al. 2019; Zurlo et al. 2021) and spectroastrometry (e.g., Brittain et al. 2019). However, the lower mass ice giants thought to be responsible for narrow rings and gaps at large radial distances ($\gtrsim 25\text{--}30$ au) remain beyond our ability to detect directly. Because gas and ice giants at such large orbital radii have no counterpart in the Solar System, these protoplanetary disk structures appear to point to an even greater diversity of planet formation outcomes than previously contemplated.

Another valuable clue in support of this picture, that planetesimals—the hypothesized building blocks of planets—commonly form in protoplanetary disks, comes from debris disks, the dusty debris that is found around some post-T Tauri and main sequence stars. Best explained as the result of collisions between large parent bodies, and identified by their infrared and millimeter excesses, debris disks accompany stars over wide range of ages. At ages 10 Myr to beyond 1 Gyr, approximately 20% to 25% of FGK stars have detected cold excesses at $\sim 100\ \mu\text{m}$ (e.g., Carpenter et al. 2009; Bryden et al. 2009; Eiroa et al. 2013; Sibthorpe et al. 2018), corresponding to debris at distances of $\gtrsim 40$ au. When imaged at high angular resolution, the debris also commonly shows substructure such as rings and gaps (e.g., Marino et al. 2018; Hughes et al. 2018; Marino et al. 2020; Nederlander et al. 2021).

Here we explore the possible evolutionary connection between the rings and gaps observed in protoplanetary disks and those in debris disks. Given that both protoplanetary disks and debris disks show structured continuum emission in the form of rings and gaps over similar radial distances (20–200 au) around approximately solar-mass stars, it seems plausible that large protoplanetary disks evolve into the known cold debris disk population. We complement related work on this topic (e.g., Michel et al. 2021) using new models of the evolution of rings of solids on Myr to Gyr timescales. The new ring models contrast with earlier generations of models that explored extended disks of solids as the origin of debris disk emission (e.g., Kenyon & Bromley 2008, 2010).

Using the new models, we examine how the efficiency of planetesimal formation affects not only the outcome of planet formation, but also its associated debris production. By comparing the model results to observations of debris disk populations, we explore the disk conditions (total initial mass of solids, planetesimal formation efficiency) that can reproduce the properties of debris disks (their incidence rate and luminosity) as a function of stellar age. We also use the comparison to explore questions such as whether cold debris disks feature in the evolutionary histories of all disks or only a special subset.

In §2, we review observations that link protostellar disks to debris disks. After a brief review of planetesimal formation in §3.1, we set up a suite of numerical calculations in rings with populations of small and large solids (§3.2) and describe the formation of planets (§3.3), debris disks (§3.4), and gaps (§3.5). After discussing the calculations in the context of observations and other models (§4), we conclude with a brief summary (§5).

2. PROPERTIES OF PROTOPLANETARY DISKS AND DEBRIS DISKS

2.1. *Protoplanetary Disks*

The millimeter continuum emission from large, bright protoplanetary disks (continuum sizes $\gtrsim 50$ au) is often highly structured. In deep, high angular resolution ALMA images of the brightest disks in nearby star-forming regions, the continuum emission typically arises from multiple concentric rings with radii of $\sim 10\text{--}150$ au, widths of a few au to tens of au, and dust masses of $10\text{--}70\ M_{\oplus}$ (ALMA Partnership et al. 2015; Huang et al. 2018; Long et al. 2018; Dullemond et al. 2018). Within larger samples of protoplanetary disks that span a wider range in disk properties, including lower millimeter continuum flux, large resolved structures are less common. Of 147 disks in Ophiuchus studied by the ODISEA survey, the great majority have millimeter continuum emission restricted to radial distances < 15 au. Only $\sim 20\%$ of the sources show continuum emission larger than 20 au in radius (see Fig. 12 of Cieza et al. 2019). In a sample of 32 disks in Taurus–Auriga that cover a broad range of continuum brightness, only a modest fraction of disks show large rings (Long et al. 2019). Nine of the 27 sources studied with stellar masses $< 1.6M_{\odot}$ have rings with effective millimeter continuum sizes > 40 au; the remainder have more compact emission.

To extrapolate the results of Long et al. (2018, 2019) and estimate the fraction of Taurus sources with large rings, we consider what is known about the entire Taurus disk population (e.g., Luhman et al. 2010; Akeson et al. 2019). We follow the rough selection criteria of Long et al. (2019) and select the Taurus Class II sources with spectral types M3

or earlier and no companions at angular separations of $0''.14\text{--}1''$. We also impose an upper stellar mass limit of $1.6M_{\odot}$ to mirror the upper mass stellar limit of the debris disk samples. With these criteria, there is a parent sample of 77 sources. The fraction with large rings in this sample is at least $9/77 = 12\%$.

The actual fraction is likely to be larger. Beyond the 32 disks studied by Long et al. (2019), 17 additional Taurus T Tauri stars were known to have ALMA observations at the time the Long et al. paper was written. Several of these sources have rings on large scales, e.g., AA Tau (Loomis et al. 2017), LkCa 15 (Facchini et al. 2020), and DM Tau (Hashimoto et al. 2021). Others show smooth emission without rings, e.g., CW Tau, CY Tau, and DG Tau (Simon et al. 2017; Bacciotti et al. 2018). At least one source is compact without large rings (CX Tau; Facchini et al. 2019), and 5 other sources have binary companions within $1''$ and would be excluded from our sample. The morphology of the remaining 5 sources is unknown (unpublished).

As a result, of the 17 additional sources, 3 definitely have large rings; the remaining 5 sources of unknown morphology may also have large rings. If all of 8 of these sources do in fact have large rings, the fraction of Taurus Class II sources with large rings could be as high as $17/77$ or $\sim 22\%$. The true fraction of disks with large rings is larger if other (as yet unobserved) sources among the parent sample of 77 sources also have rings.

At the same time, a robust estimate of the fraction of young stars with large rings requires that we also account for the lack of rings among the population of (diskless) Class III sources with similar ages, stellar masses, and companion properties as the Class II sources. As a group, the Class III sources represent 25% of all T Tauri stars in Taurus (e.g., Luhman et al. 2010; Luhman 2018; Esplin & Luhman 2019). Accounting for these diskless sources reduces the fraction of young stars with large rings by a factor of $\sim 3/4$. In summary, the fraction of young stars in Taurus with large rings is plausibly $\sim 17\%$, although with significant uncertainty (J. Bae and A. Isella, private communication). Further ALMA imaging of a larger sample is needed for a robust estimate. Taking a similar approach, van der Marel & Mulders 2021 estimated a fraction of $\sim 16\%$ of structured disks in a sample study of almost 700 disks in nearby star forming regions.

Fig. 1 illustrates the range of sizes and widths of continuum emission rings observed in T Tauri disks (primarily from the DSHARP sample; Table 1 of Huang et al. 2018). In the left side of the diagram, the purple bars indicate the radial extent of bright rings; the blue bars indicate the rough radial extent of the dust continuum emission from the disk. The high angular resolution of the DSHARP observations (30–60 mas; equivalent to 5–8 au at the distance of the targets) probed structures at much smaller angular scales than was possible with the lower resolution, snapshot ALMA observations of Long et al. (~ 120 mas or ~ 16 au).

2.2. Debris Disks

Spatially resolved images of debris disks also show rings in scattered light and thermal emission (e.g., Hughes et al. 2018). Fig. 1 shows the radial extents of debris disks (light-colored bars) and their rings (dark-colored bars), as measured by direct imaging (Hughes et al. 2018). As shown in the Figure, much of the emission from debris arises from within $a = 10\text{--}150$ au of the star, similar to the orbital distances from which the millimeter continuum arises from protoplanetary disks. The fractional widths of the rings are typically $\Delta a/a = 0.1\text{--}0.6$, with Δa typically ranging from a few au to 30 au, overlapping the range of widths of protoplanetary disk rings.

While fine substructure (i.e., narrow rings) is reported more commonly for protoplanetary disks than debris disks, only a few debris disks have been imaged with sufficient sensitivity and angular resolution to detect such substructure (see discussion in Marino et al. 2020; Nederlander et al. 2021). Of the 6 sources studied to date at high sensitivity and angular resolution, 4 show gaps in their continuum emission, suggesting that finer substructure may be common among large debris disks, as in protoplanetary disks¹. Future ALMA imaging is needed to explore this possibility.

Surveys of varying sensitivities to dust temperature and fractional luminosity have reported detection rates of debris disk emission. As described in Hillenbrand et al. (2008), the FEPS Survey used the *Spitzer Space Telescope* to carry out a census of cool dust surrounding 328 solar-type stars in the age range 3 Myr – 3 Gyr located at distances of 10 pc – 200 pc. Over the age range 30 Myr to 3 Gyr, $\sim 10\%$ of solar-type stars show evidence for cold debris, with their rising spectral energy distributions toward $70\ \mu\text{m}$ indicating dust temperatures of $\sim 45\text{--}85$ K for dust in equilibrium with the stellar radiation field. The detected excesses are bright at young ages, with fractional excess luminosities of $L_d/L_* \sim 10^{-3}\text{--}10^{-4}$ at 30 Myr, declining with increasing stellar age to $L_d/L_* \sim 10^{-4}$ at 3 Gyr.

¹ The gaps are all located at ~ 70 au; these are HD 107146, HD 92945, HD 15115, HD 206893. The other two sources without reported gaps are beta Pic and AU Mic.

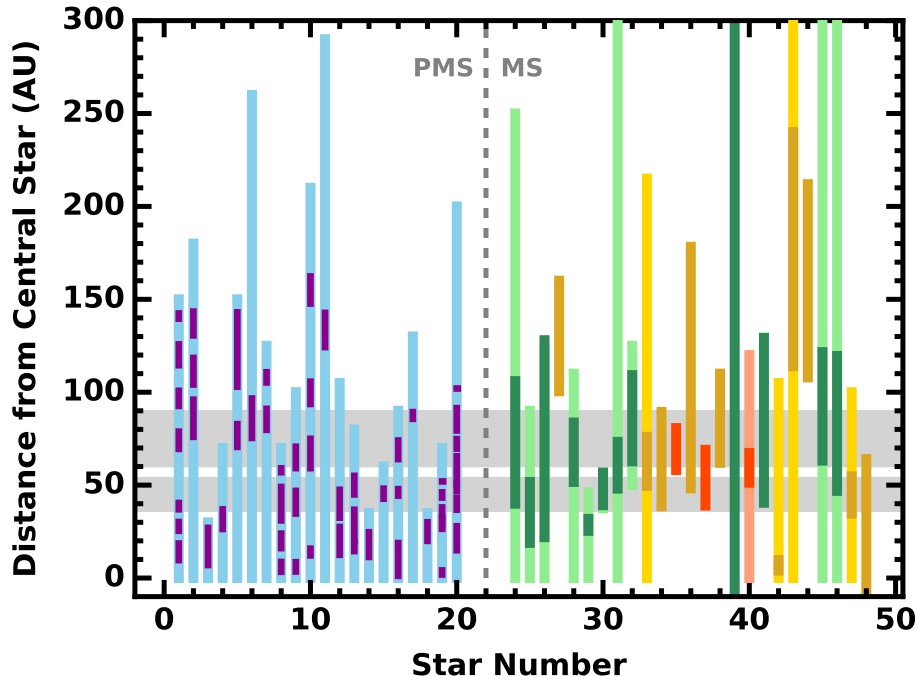


Figure 1. Comparison of the observed positions of bright rings in the continuum emission from protoplanetary disks around T Tauri stars (left side; Huang et al. 2018) to bright rings within extended dusty debris disks surrounding FGK main sequence stars (right side; Hughes et al. 2018). For each vertical bar, light (dark) regions indicate the extent of the disk (rings). Disks around main sequence stars are ordered by age, from 12 Myr for star 24 (HD 146897) to 8.2 Gyr for star 48 (τ Cet). Colors denote the spectral type—F (green), G (gold), or K (orange)—of the central star. The vertical grey dashed line separates pre-main-sequence (PMS) from main sequence (MS) stars. The horizontal grey bands represent the two grids used in the numerical calculations described in section 3.

While FEPS focused on the excess properties of FGK stars younger than 3 Gyr, other *Spitzer* surveys investigated the excess properties of older stars. Bryden et al. (2009) reported the excess properties of planet-bearing stars with spectral types F5–K5 that are known from radial velocity studies to harbor one or more planets; the majority of the stars are 4–10 Gyr old where, as in the case of most of the FEPS sources, the ages are based on chromospheric activity and the calibration of Mamajek & Hillenbrand (2008). The excess properties of the sample are statistically indistinguishable from those of a comparison sample of comparable nearby stars (i.e., similar in spectral type and age) without known planetary companions.

To illustrate the limits placed by these *Spitzer* results on possible evolutionary paths for disk solids, the upper panel of Fig. 2 shows detections (purple dots) and upper limits (smaller gray dots; Carpenter et al. 2009; Bryden et al. 2009) as a function of stellar age. Protoplanetary disk sources in the FEPS sample are excluded. Only the FEPS sources within 80 pc are shown to highlight the value of the constraints placed by the upper limits on the nearby sample. The full FEPS sample spans a large range in distance (out to ~ 150 pc) and upper limits on the distant sources are weak. For the few sources in common between the FEPS and Bryden et al. samples (HD38529 and HD150706), we adopted the excess properties reported by FEPS. A few sources with unusually high flux uncertainties and upper limits were removed from the Bryden et al. sample (HD 4203, HD 46375, HD168746, and HD330075).

To obtain the FEPS upper limits shown, we converted the 70 micron flux upper limits (typically ~ 10 mJy, $1-\sigma$) to upper limits on L_d/L_* assuming a typical ratio of $r = (L_d/L_*)/(F_d/F_*) = 10^{-5}$, a factor appropriate for the typical temperature of detected FIR excesses (60 K; Hillenbrand et al. 2008); the conversion factor is insensitive to temperature in the range 40–80 K (e.g., Figure 9 of Hillenbrand et al. 2008). Following (Carpenter et al. 2009) for both the FEPS sources discussed here and the *Herschel* sources discussed below, the plotted upper limits in Fig. 2 of $L_d/L_* = r(F_d/F_* + 3\sigma)$, use the reported value of F_d/F_* when its value is > 0 and 0 otherwise. The upper limits shown for the Bryden et al. survey are from their paper.

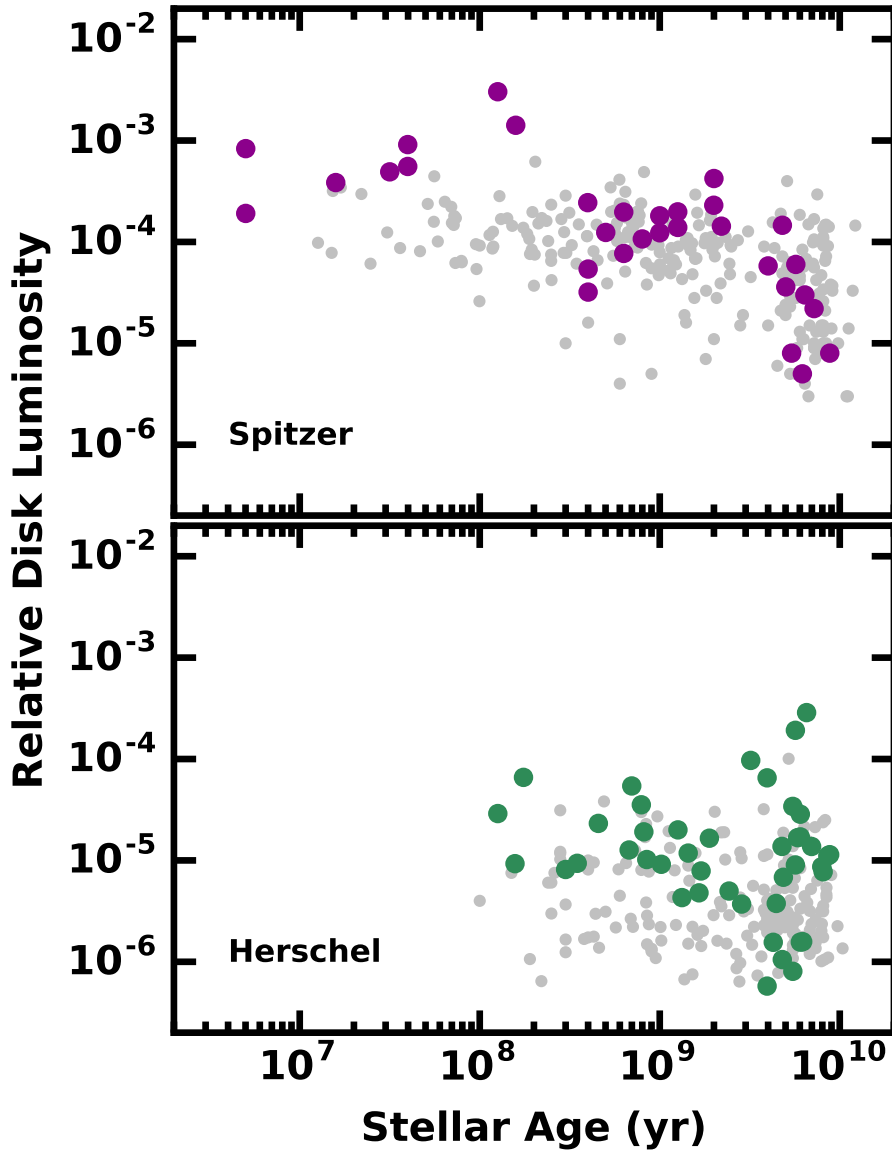


Figure 2. Relative disk luminosity for debris disks from *Spitzer* (upper panel; Carpenter et al. 2009; Bryden et al. 2009) and *Herschel* (lower panel; Eiroa et al. 2013; Sibthorpe et al. 2018) observations. Large filled circles indicate detections; small symbols indicate upper limits for all sources (*Herschel*) or those with $d \leq 80$ pc (*Spitzer*).

Following the *Spitzer* studies, the DEBRIS and DUNES surveys searched for infrared excess emission at $100 \mu\text{m}$ and $160 \mu\text{m}$ with the *Herschel Space Observatory* (Eiroa et al. 2013; Sibthorpe et al. 2018). Both programs observed several sources at $70 \mu\text{m}$; DUNES acquired additional data at $250\text{--}500 \mu\text{m}$. The surveys targeted 275 (DEBRIS) and 133 (DUNES) unique FGK stars with distances within 25 pc (DEBRIS; Sibthorpe et al. 2018) and 20–25 pc (DUNES; Eiroa et al. 2013). Stellar activity ages range from 1 Myr to 11 Gyr (100 Myr to 10 Gyr) for DEBRIS (DUNES), with median ages of ~ 3 Gyr.

The DEBRIS (DUNES) survey detected excess emission from debris disks around 47 (31) stars for a nominal detection rate of 17% (23%). In DEBRIS, the detection rate is similar across the age bins 0.1–1 Gyr, 1–3 Gyr, and 3–10 Gyr. Corrected for incompleteness, the incidence rate for FGK stars is $\sim 28\%$. For DUNES, the volume-limited detection rate is $\sim 20\%$ and is independent of spectral type for FGK stars (see also Montesinos et al. 2016).

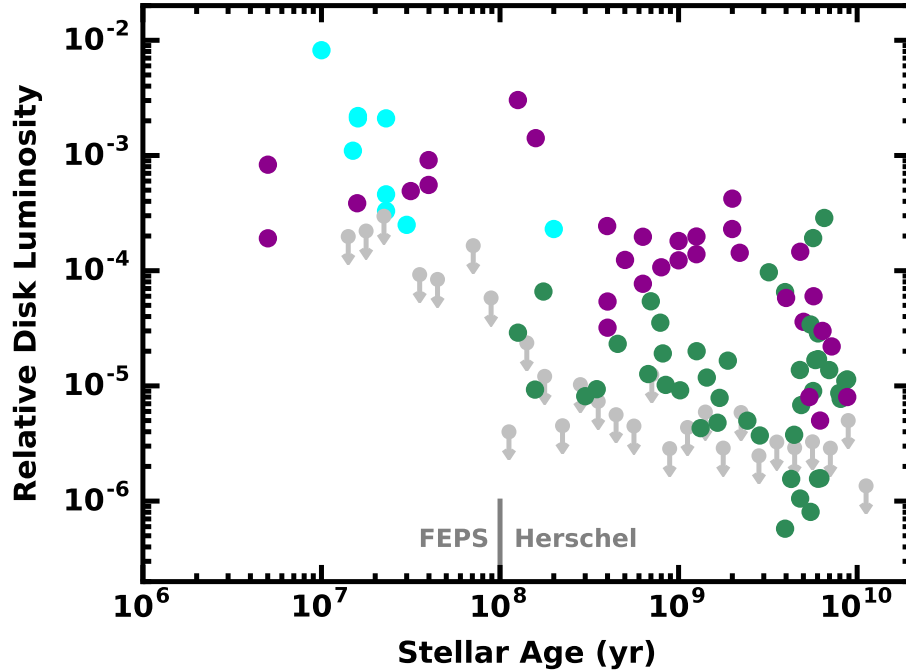


Figure 3. Relative disk luminosity for the full sample of debris disks summarized in the text. Filled circles indicate detections from [Matrà et al. \(2018\)](#), cyan), *Spitzer* (purple, Fig. 2, upper panel), and *Herschel* (green, Fig. 2, lower panel). Grey symbols indicate the median of upper limits in 0.1 intervals of log stellar age from FEPS (age ≤ 100 Myr) or *Herschel* (age ≥ 100 Myr) data.

For the combined set of DEBRIS and DUNES detections, the median L_d/L_* is roughly an order of magnitude smaller than the median dust luminosity of the *Spitzer* detections. For both *Herschel* programs, blackbody dust temperatures have a broad range, 16–300 K for DEBRIS and 20–100 K for DUNES; the median dust temperatures are 48 K (DUNES) and 63 K (DEBRIS). Inferred radii for the dust are 1–300 au with a median ~ 20 au for DEBRIS and 7–200 au with a median of ~ 30 au for DUNES. Assuming realistic dust properties would place the emission at larger radii.

The lower panel of Fig. 2 shows the *Herschel* detections (green dots) and upper limits (smaller gray dots) for the 43 sources with FGK spectral types (effective temperatures of 4000–7200 K) and ages as estimated from stellar activity (e.g., [Vican 2012](#)). To translate flux detection upper limits to L_d/L_* , the reported $3\text{-}\sigma$ upper limit on F_d/F_* at $100\ \mu\text{m}$ was converted to L_d/L_* assuming a ratio $r = (L_d/L_*)/(F_d/F_*) \simeq 10^{-5.4}$, the value appropriate for an excess at $100\ \mu\text{m}$ that has a temperature of ~ 55 K, the median temperature of detected excesses. The actual adopted value of r is appropriate for the stellar temperature of each source.

To illustrate a larger range of excess properties observed among debris disks, Fig. 3 supplements the *Spitzer* and *Herschel* detections (purple and green dots, respectively) with those from [Matrà et al. \(2018\)](#), which compiles properties of (bright) debris disks that have been spatially resolved at millimeter wavelengths. Sources with FGK spectral types not included in the *Spitzer* ([Carpenter et al. 2009](#); [Bryden et al. 2009](#)) and *Herschel* ([Eiroa et al. 2013](#); [Sibthorpe et al. 2018](#)) samples are shown. The grey arrows show the median upper limits from FEPS at ages ≤ 100 Myr and from *Herschel* at ages ≥ 100 Myr in 0.1 intervals of log stellar age.

Limits on L_d/L_* for younger stars with ages $\lesssim 4\text{--}5$ Myr are rare. [Lovell et al. \(2021\)](#) detected one source with cold debris in an ALMA survey of 6 class III T Tauri stars that are likely members of the 1–3 Myr Lupus association; the other sources in the [Lovell et al. \(2021\)](#) study are likely to be members of the Sco-Cen Association ([Michel et al. 2021](#)). Future observations of class III T Tauri stars in other star-forming regions would improve links between class II sources with $L_d/L_* \gtrsim 3 \times 10^{-2}$ (e.g., [Michel et al. 2021](#)) and debris disks with $L_d/L_* \lesssim 10^{-2}$.

Finally, parallax data from the *Gaia* satellite have revolutionized our knowledge of nearby moving groups of young stars (e.g., [Faherty et al. 2018](#); [Gagné et al. 2018, 2020](#); [Ujjwal et al. 2020](#)), leading to new membership catalogs that allow better probes of the frequency of cold debris disks in the 20–150 Myr age range where the *Spitzer* and *Herschel* surveys have poor statistics. Among the ~ 10 F stars within the 20–25 Myr old β Pic moving group, 50% (75%) have

dusty material at $a \gtrsim 40$ au ($a \gtrsim 1$ au; Pawellek et al. 2021). For F stars in older moving groups (20 stars in the Tucana/Horologium association and the Columba and Carina groups), the cold debris disk frequency declines to $\sim 30\%$ at 45 Myr and $\sim 15\%$ at 150 Myr². However, few of the new 45–150 Myr old debris disks have $a \gtrsim 30$ au.

With $L_d/L_\star \approx 2 \times 10^{-4}$ to 2×10^{-3} , the cold debris disks in the β Pic moving group have dust luminosities similar to the L_d/L_\star of stars with ages of 10–40 Myr in Fig. 3. The new systems with ages of 40–50 Myr from other moving groups have lower dust luminosities, $L_d/L_\star \approx 2 \times 10^{-5}$ to 10^{-4} , which roughly coincides with the FEPS upper limits in Fig. 2. These data thus follow the observed trend of decreasing L_d/L_\star with stellar age. Continued analysis of cold debris in 30–100 Myr old stars would provide essential connections between the younger more luminous debris disks and those much older than 100 Myr.

To summarize, debris disk detections fall along a broad swath in L_d/L_\star and decline with time (Fig. 3). The most stringent upper limits in L_d/L_\star are $\lesssim 10^{-5}$ at ages of 0.1–10 Gyr (from the *Herschel* surveys), and $\sim 10^{-4}$ at 10–100 Myr (from FEPS). Current data suggest the frequency of cold debris disks is roughly constant at $\sim 25\%$ for stellar ages of ~ 50 Myr to 10 Gyr. Within the much younger β Pic moving group (~ 20 –25 Myr), the frequency may be higher, $\sim 50\%$, based on the study of a small sample of stars. As discussed below, future observations that lead to greater certainty in the debris disk frequency and L_d/L_\star for stars with ages of 20–150 Myr will bear on the variety of ways in which protoplanetary disks evolve into debris disks (Section 4).

3. EVOLUTION OF RINGS OF SOLIDS

To understand whether the rings of solids observed at $a \approx 20$ –200 au in young stars could plausibly evolve into the rings of debris detected at similar a in much older stars, we perform a suite of multiannulus coagulation calculations. For the geometry of the rings, we rely on the observed properties outlined in §2. In previous calculations, Kenyon & Bromley (2008, 2010) considered the evolution of swarms of 1–100 km planetesimals in disks extending from 30–150 au. These calculations matched the time evolution of available data for L_d/L_\star rather well. However, for disks with the largest L_d/L_\star , the models predict that dust is produced at increasingly large distances from the central star at late times. This trend is not observed among known debris disks (e.g., Najita & Williams 2005; Kennedy & Wyatt 2010; Matthews et al. 2014; Hughes et al. 2018, see also Fig. 1). Moreover, theory currently favors scenarios where planets grow in seas of small and large solids (see below). Together, these observational and theoretical developments motivate an updated set of models of debris production. To support our choices for the initial mix of pebbles and planetesimals, we briefly review recent theoretical results. Following this summary, we outline the numerical procedures and then describe results of new calculations.

3.1. Background

In the core accretion model, planet formation is a three-step process. Within a circumstellar disk of gas and dust, micron-sized dust grains grow into cm-sized pebbles then km-sized or larger planetesimals then planets. Within each step, various uncertainties in the initial conditions, the physical properties of the gas and solids, and the important chemical and physical processes prevent a robust understanding of the path from grains to planets. For this discussion, we summarize the current picture of planet formation, highlighting several areas of significant uncertainty that we explore in our models.

Initially, the gas and dust are well-mixed (e.g., Chiang & Youdin 2010; Youdin 2010; Youdin & Kenyon 2013; Liu & Ji 2020). As the disk evolves, small grains collide slowly, stick together, and grow into larger and larger aggregates (e.g., Dominik & Tielens 1997; Wurm & Blum 1998; Blum & Wurm 2008; Birnstiel et al. 2016; Nimmo et al. 2018). As growth proceeds, collisions compactify particles significantly (e.g., Weidling et al. 2009). Particles with larger filling factors are less well-coupled to the gas. When grains uncouple from the gas, they settle to the midplane and collide at higher velocities. Interactions between particles become more elastic, which limits additional growth (e.g., Zsom et al. 2010; Kelling et al. 2014; Kruss et al. 2017). Detailed studies suggest that particles experience a ‘bouncing barrier’ at sizes ~ 1 –10 cm beyond which agglomeration effectively ceases (see also Brauer et al. 2008; Windmark et al. 2012; Gundlach & Blum 2015; Kruss & Wurm 2020; Teiser et al. 2021).

Although the presence of charged or organic grains may circumvent the bouncing barrier (e.g., Homma et al. 2019; Steinpilz et al. 2019), recent analyses have concentrated on the ‘streaming instability’ as a way to generate km-sized or larger planetesimals from ensembles of cm-sized ‘pebbles’ (Youdin & Goodman 2005). In this mechanism, aerodynamic

² At 45 Myr (150 Myr), 6 of 20 (1 of 7) stars in these samples have blackbody radii larger than 10 au.

drag concentrates pebbles into clumps with large overdensities compared to the typical solid-to-gas ratio throughout the disk (e.g., Johansen & Youdin 2007; Johansen et al. 2007, 2009). Continued concentration of pebbles within the clumps enables the formation of planetesimals with radii $r \approx 100\text{--}1000$ km (e.g., Birnstiel et al. 2016; Simon et al. 2016; Schäfer et al. 2017; Yang et al. 2017; Li et al. 2018; Sekiya & Onishi 2018; Lenz et al. 2019; Liu et al. 2019; Li et al. 2019; Chen & Lin 2020; Umurhan et al. 2020; Pan & Yu 2020; Gerbig et al. 2020; Squire & Hopkins 2020).

In recent numerical studies of the streaming instability, the size distribution of the largest planetesimals and the efficiency of planetesimal formation depend on the physical conditions of the gaseous disk and the size distribution of pebbles (e.g., Simon et al. 2016; Li et al. 2018; Abod et al. 2019; Carrera et al. 2020; Klahr & Schreiber 2020; Gole et al. 2020; Rucska & Wadsley 2021). Large solid-to-gas ratios generated by radial drift and low turbulence ($\alpha \lesssim 10^{-4}$) favor efficient concentration of mono-disperse (i.e., single-sized) sets of pebbles into much larger solids. High turbulence ($\alpha \gtrsim 10^{-3}$), smaller solid-to-gas ratios, and broader size distributions of pebbles appear to limit the ability of the streaming instability to form large planetesimals (however, see also McNally et al. 2021). Among calculations with identical starting conditions, local fluctuations in these and other physical conditions within the disk lead to variations in the maximum size r_{max} of a planetesimal and the fraction f of the initial solid mass in pebbles that is concentrated into massive planetesimals.

Among other options for planetesimal formation, such as turbulent clustering (e.g., Cuzzi et al. 2008; Pan et al. 2011; Hartlep & Cuzzi 2020) and the settling instability (Squire & Hopkins 2018), outcomes for f and r_{max} are also uncertain. For any instability mechanism, local chemistry, radial diffusion, and sublimation modify the growth of pebbles and the concentration of pebbles into planetesimals (e.g., Ida & Guillot 2016; Hyodo et al. 2019). Prior to the onset of instability, the porosity and compactness of pebbles are also uncertain (e.g., Okuzumi et al. 2012; Kataoka et al. 2013).

Once planetesimals form, the path to protoplanets is more certain. In systems with $f \approx 1$ (completely efficient planetesimal formation), the growth of massive protoplanets may be too slow to form super-Earth mass and larger planets during the likely lifetime of the gaseous disk (e.g., Kenyon & Bromley 2008; Lissauer et al. 2009; Kenyon & Bromley 2009, 2010; Kobayashi et al. 2010; Levison et al. 2010; D’Angelo et al. 2014; Mordasini et al. 2015; Bodenheimer et al. 2018; D’Angelo et al. 2021). From analytical considerations, Goldreich et al. (2004) and Rafikov (2005) demonstrated that a few large planetesimals in a sea of pebbles grow rapidly due to the small scale height of the pebbles. Subsequent numerical calculations of ‘pebble accretion’ yield $10 M_{\oplus}$ and larger ice giants on time scales of a few Myr (Kenyon & Bromley 2009; Bromley & Kenyon 2011a; Lambrechts & Johansen 2012). More recent studies with $r_{max} \gtrsim 100$ km and $f \lesssim 10^{-2}$ illustrate the ability of pebble accretion to form ice and gas giants in many circumstances on short time scales (e.g., Matsumura et al. 2017; Alibert et al. 2018; Lin et al. 2018; Bitsch et al. 2019; Johansen & Bitsch 2019; Lambrechts et al. 2019; Morbidelli 2020; Voelkel et al. 2020; Klahr & Schreiber 2020; Chambers 2021).

In contrast to the many studies of giant planet formation via pebble accretion, there have been few attempts to investigate the long-term evolution of the debris signatures produced by growing protoplanets in a sea of pebbles. Formation scenarios for a planet nine at $a \gtrsim 200$ au in the Solar System illustrate how systems with an initial $r_{max} = 100$ km and various f generate super-Earth mass planets and very luminous debris disks at 200–750 au around solar-type stars on time scales of 0.1–1 Gyr (Kenyon & Bromley 2015, 2016a). The debris disks in some model systems have properties similar to those observed in the bright debris disks orbiting HD 107146, HD 202628, and HD 207129 (Corder et al. 2009; Krist et al. 2010, 2012; Marshall et al. 2011; Ricci et al. 2015; Marino et al. 2018). In the next sections, we consider whether swarms of pebbles and planetesimals can produce debris disks similar to those in the *Herschel* and *Spitzer* samples described in section 2.

3.2. Initial Conditions

To follow the evolution of pebbles and planetesimals in a ring, we use the multiannulus coagulation routine within *Orchestra*, an ensemble of codes for planet formation. As outlined in the Appendix, the code uses a particle-in-a-box algorithm for collision rates and energy scaling for collision outcomes. Particles evolve dynamically with Fokker-Planck routines. To avoid the extra free parameters associated with the gaseous component of the ring, we ignore radial drift and circularization of solids by the gas. Kenyon & Bromley (2008, 2010, 2012) describe the formulation and procedures in more detail.

For this study, we perform calculations in two separate grids, each with 28 concentric annuli. With an inner radius of 36 au (60 au) and an outer radius of 54 au (90 au), the grids cover a reasonable subset of the rings observed in

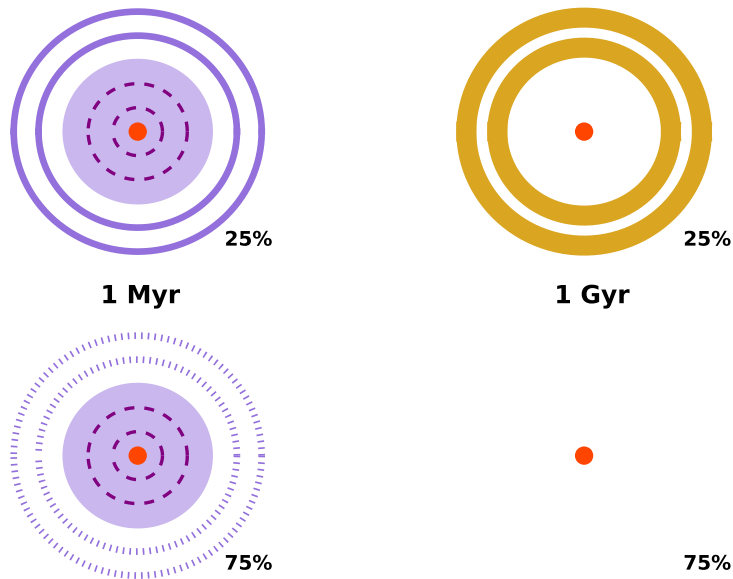


Figure 4. Schematic architectures for protoplanetary disks (left diagrams) and older main sequence stars (right diagrams). Each illustration includes the approximate percentage of stars with the sketched architecture. On the left, light purple filled circles indicate compact gaseous disks; dashed circles show possible locations of dense rings within the disk. Outside the compact disks, solid (dotted) circles illustrate locations of dense (invisible) rings of solids. On the right, the gold bands in the upper diagram mark the location of a debris disk.

protoplanetary and debris disks (Fig. 1). Within each annulus, particles occupy distinct mass bins with sizes ranging from $1 \mu\text{m}$ to 10^5 km , orbital eccentricity e , and inclination i . Initially, solids have sizes of 1 cm (residual pebbles) and 100 km (planetesimals produced by the streaming instability), eccentricity $e_0 = 10^{-3}$, and inclination $i_0 = e/2$. These parameters are appropriate for solids recently liberated from a protostellar disk with turbulence parameter $\alpha \sim 10^{-3}$.

Solids initially have a total mass M_0 , a surface density distribution $\Sigma(a)$, and a fraction f of mass in large planetesimals (see section 3.1). To select these parameters, we rely on the observational constraints described above and shown schematically in Fig. 4. Among class II sources with ages $\sim 1 \text{ Myr}$, roughly a quarter have a compact disk with an outer radius of $\sim 30 \text{ au}$ and bright rings of solids at larger distances (Fig. 4, top left; see also Fig. 1). The rings are well-fit with gaussian distributions of pebbles having total masses $\sim 10\text{--}60 M_\oplus$ and dispersions $\sigma \approx 4\text{--}8 \text{ au}$ (Dullemond et al. 2018). To span this range, we adopt upper limits of $M_0 = 10 M_\oplus$ at 45 au and $M_0 = 45 M_\oplus$ at 75 au . For $\Sigma(a)$, we adopt a fixed ratio $\sigma/a = 1/15$; solids then have a gaussian $\Sigma(a)$ centered at 45 au (75 au) with $\sigma = 3 \text{ au}$ (5 au). Defining P as the orbital period around the central star, the maximum M_0 and the gaussian $\Sigma(a)$ yield a similar ratio for P/Σ at 45 au and 75 au and therefore similar time scales for the growth of planets (e.g., Lissauer 1987).

In the majority of class II sources with compact disks and no bright rings (Fig. 4, bottom left), the lack of millimeter emission at large radii is consistent with the solids outside the compact disk having either (i) low mass if composed primarily of pebbles or (ii) higher mass if composed primarily of large planetesimals. These possibilities motivate a broad range in M_0 (from $0.01 M_\oplus$ to the adopted upper limits) and f ($0\text{--}1$).³ A plausible third option for the lack of millimeter emission in these sources is a small vertical scale height which prevents solids from intercepting a detectable fraction of light from the central star. For the calculations reported here, we do not consider this possibility but return to it in the discussion.

³ The lower mass limit is somewhat smaller than current mass estimates for the Kuiper belt ($0.02\text{--}0.06 M_\oplus$; Pitjeva & Pitjev 2018; Di Ruscio et al. 2020), which has a dust luminosity well below *Herschel* sensitivity limits (e.g., Backman et al. 1995; Vitense et al. 2012).

The observed properties of debris disks also motivate a range in M_0 and f . Among solar-mass stars with ages of ~ 1 Gyr, roughly 25% have bright rings of cold debris at $a \gtrsim 40$ au (Fig. 4, top right). In the remaining 75%, cold debris is absent or undetectable (Fig. 4, bottom right). The goal of the calculations is to identify the initial conditions and evolutionary paths that connect the protoplanetary disks (left) to the debris disks (right), while satisfying the constraints on the incidence rates and dust luminosities of known debris disks as a function of stellar age (e.g., Fig. 1 and Fig. 3). One simple hypothesis we explore is whether the massive rings of protoplanetary solids (upper left of Fig. 4) evolve into rings of debris at similar distances at Gyr ages (upper right of Fig. 4).

Other evolutionary scenarios are also plausible. If some of the 75% of class II sources that appear as compact disks at millimeter wavelengths possess substantial rings of solids that are invisible at millimeter wavelengths as a result of their lower mass or lack of pebbles, these may evolve into bright debris disks at late times (e.g., Wyatt 2008; Kenyon & Bromley 2010; Matthews et al. 2014; Krivov & Wyatt 2021, and references therein). To explore the evolution of these systems, we also follow the evolution of low mass rings of pebbles and more massive rings composed of large planetesimals.

Based on these considerations, we consider initial masses $M_0 = 0.01\text{--}45 M_\oplus$ for eight values of f between 0 and 1. As summarized in Appendix Tables 1 and 2, some combinations of M_0 and f are not physically realizable in a ring with pebbles and large planetesimals. For example, with $M_0 = 0.01 M_\oplus$ and $f = 10^{-3}$, the mass in a single 100 km planetesimal exceeds $M_0 \times f$, the total mass allocated for all larger bodies.

In identifying the relevant evolutionary path (or combination of paths) for protoplanetary and debris disks, we aim to ensure continuity between the starting and ending points outlined in Fig. 4. That is, if young stars simply move horizontally in Fig. 4, from bright rings at 1 Myr to bright rings at 1 Gyr *and* from compact disks into diskless main sequence stars, we are guaranteed to match the observed fraction of debris disks at every epoch from ~ 50 Myr to 10 Gyr. However, if some sources with compact disks and invisible rings of solids at 1 Myr evolve into observable debris disks at 1 Gyr, then a similar fraction of class II sources with bright rings must evolve into diskless main sequence stars. In this case, we need to ensure that the fraction of class II sources that evolve diagonally upward in the figure matches the fraction that evolve diagonally downward.

If the high fraction of cold debris disks in the β Pic moving group is typical of all 20–25 Myr-old stars (50%; Pawellek et al. 2021), then a large fraction of class II sources without bright rings need to evolve into bright debris disks at 20–25 Myr and then fade below current detection limits for stellar ages of 50–100 Myr. An additional goal of this study is to understand the physical properties of protoplanetary disks that lead to this type of evolution.

The following sections describe the growth of the largest objects (§3.3), the evolution of the dust luminosity from collisional debris (§3.4), and the impact of the largest objects on the radial distribution of the debris and gap formation (§3.5).

3.3. Growth of Planets

As each calculation proceeds, pebbles and planetesimals collide and merge into larger objects. Along with mergers, debris from collisions deposits mass into other mass bins. At first, the low initial e and i limits collisions between particles within different annuli. Evolution of e and i allows more interactions among all particles; these interactions disperse collision debris throughout the grid. Most collisions yield some debris with particle sizes smaller than 1 μm . This material is assumed ejected by radiation pressure from the central star. Over 10 Gyr of evolution, the amount of lost material ranges from less than 1% to more than 90% (see Appendix Tables 1 and 2). Ejected solids do not interact with other solids in the grid.

To set some expectations for the calculations, we estimate the time scale for the growth of planets in rings at 45 au and 75 au. In Kenyon & Bromley (2010), 100 km planetesimals grow into Pluto-mass planets on a time scale $t_{1k} \sim 10$ Gyr at 80 au in a disk with the solid surface density distribution of a minimum mass solar nebula. In these calculations, $t_{1k} \propto P/\Sigma$, where P is the orbital period and Σ is the initial surface density (see also Lissauer 1987; Goldreich et al. 2004; Rafikov 2005; Kenyon & Bromley 2008). Scaling these results to 45 au and 75 au,

$$t_{1k} \approx 2 \text{ Gyr} \left(\frac{M_{ref}}{M_0} \right) \quad (1)$$

where $f = 1$ and $M_{ref} = 10 M_\oplus$ (45 M_\oplus) is the mass contained in rings at 45 au (75 au). When $f < 1$, analytical estimates suggest $t_{1k} \propto f^n$, with $n \approx 0.5\text{--}1.0$ (Goldreich et al. 2004; Rafikov 2005). The calculations here provide good tests of these estimates, as discussed in the Appendix.

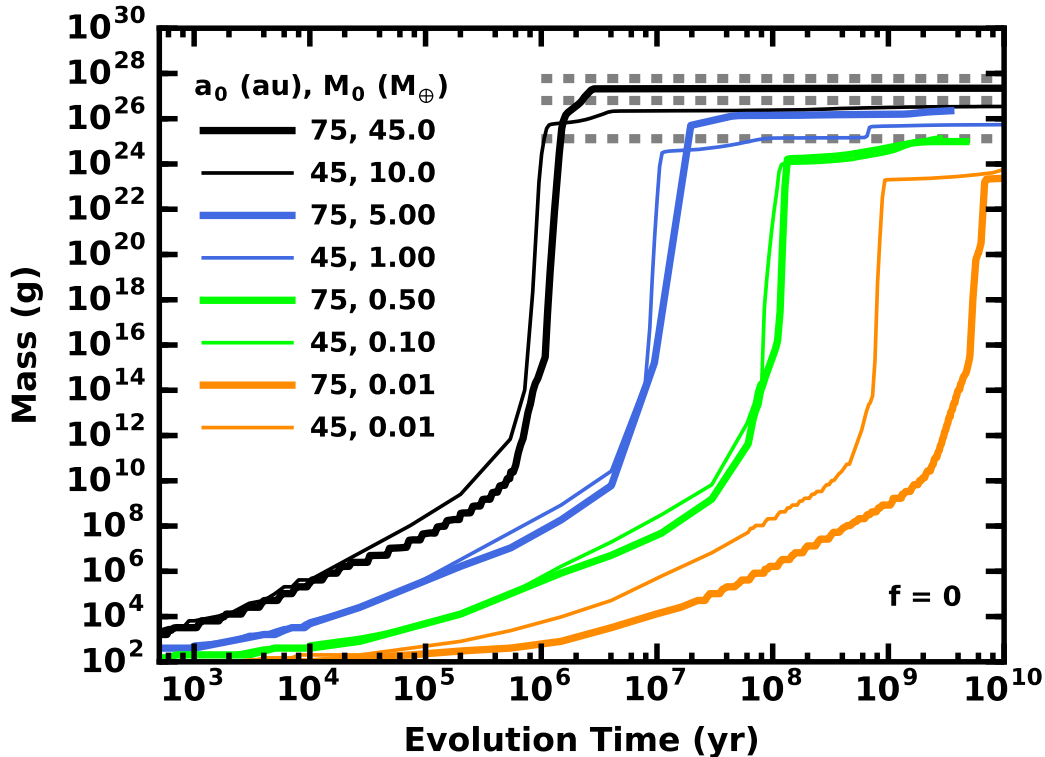


Figure 5. Time evolution of the mass of the largest object in rings of solids with initial $f = 0$ and the values for a_0 and M_0 indicated in the legend. Dashed horizontal lines indicate the mass of Pluto (lower), Mars (middle), and Earth (upper). At 45–75 au, massive rings of solids produce super-Earths in 1 Myr ($M_0 = 45 M_\oplus$ at 75 au, thick purple curve), Mars mass planets in 10–100 Myr ($M_0 = 5\text{--}10 M_\oplus$ at 45–75 au, thin purple and thick dark green curves), and Plutos in 100 Myr to 1 Gyr ($M_0 = 0.01\text{--}0.5 M_\oplus$ at 45–75 au, light green and orange curves).

In the full set of calculations, outcomes are sensitive to M_0 and f . Systems with more mass in solids tend to evolve more rapidly and form the largest planets and the brightest debris disks. For fixed initial mass, rings with more of their initial mass in planetesimals evolve more slowly. When f is large, planetesimals compete for pebbles. As the initial population of pebbles declines, growth depends on infrequent planetesimal–planetesimal collisions and the evolution stalls. When f is small, planetesimals do not compete for pebbles; growth is then rapid.

Fig. 5 illustrates the growth of the largest object in systems with $f = 0$. At the start of each calculation, gravitational focusing is negligible; pebbles grow roughly linearly with time. Slow pebble growth allows collisional damping to reduce e and i by an order of magnitude. As the largest particles approach km sizes, collision velocities remain low despite increased dynamical friction and viscous stirring by the largest objects. Larger gravitational focusing factors initiate an explosive phase of runaway growth, where planetesimals with maximum radii $r_{max} \sim 1$ km rapidly reach much larger sizes, $r_{max} \gtrsim 1000$ km. After the runaway, a few protoplanets continue to accrete more and more material from the smaller objects and to stir up the velocities of the leftovers. At first, collisional damping among the pebbles counters stirring by protoplanets. Eventually, stirring overcomes damping and initiates a collisional cascade, where km-sized and smaller objects are ground into smaller and smaller particles. The cascade robs protoplanets of remaining small solids; growth ceases.

Aside from the time scale and the final mass, the evolution of the mass of the largest protoplanet is amazingly independent of a and M_0 . All of the curves in Fig. 5 have the same linear phase for $M \lesssim 10^{12}$ g followed by a nearly vertical rise to a maximum planet mass that scales with M_0 . During runaway growth, planets accrete nearly all of the mass in their annulus (and sometimes in adjacent annuli). With more mass in protoplanets than pebbles, stirring reduces gravitational focusing factors. The evolution is then oligarchic, where the largest protoplanets slowly accumulate leftover pebbles (e.g., Kokubo & Ida 1998; Ormel et al. 2010). Once pebbles are exhausted, growth ceases. In the most massive rings, Earth mass planets form in 3–10 Myr. When M_0 is smaller, growth takes longer and results

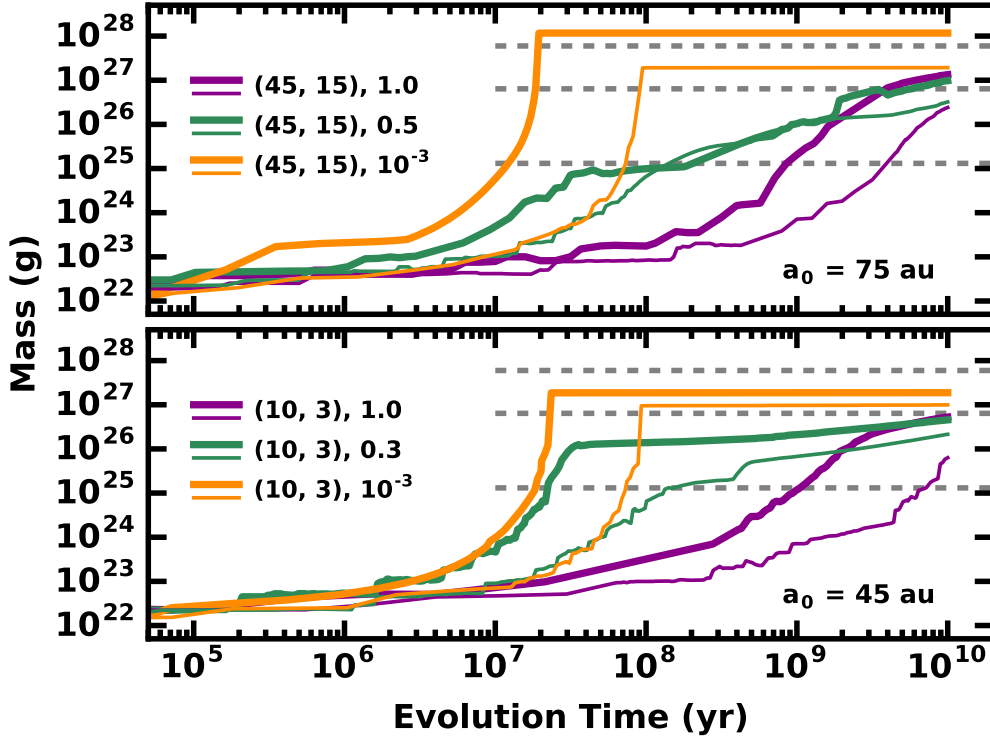


Figure 6. As in Fig. 5 for calculations at 45 au (lower panel) and at 75 au (top panel) with various M_0 and f . The legend in the upper left of each panel indicates a pair of M_0 for thick (first M_0) and thin (second M_0) lines and the value of f for each curve. Dashed horizontal lines indicate the masses of Pluto (lower), Mars (middle), and Earth (upper). Runaway growth is more dramatic in rings with small f . At 75 au, massive rings with small f produce super-Earths in 20–30 Myr (thick orange curve). Rings with smaller f generate Mars-mass planets on much longer times scales, 1–10 Gyr (thick purple, thick green, and thin green curves) At 45 au, rings with $M_0 = 3\text{--}10 M_\oplus$ and $f \approx 10^{-1} - 10^{-4}$ produce Mars mass planets in 20–100 Myr. Models with $f \approx 0.3\text{--}1.0$ yield Plutos to Mars-mass planets in 1–10 Gyr..

in lower mass protoplanets. In the lowest mass rings we consider, Pluto mass planets form on Gyr or longer time scales. The progression of longer time scales to produce lower mass planets when M_0 is small is characteristic of coagulation calculations (eq. 1).

When $f > 0$, the final planet mass correlates well with M_0 and f . At 75 au (Fig. 6, upper panel), rings with $f \approx 10^{-2} - 10^{-5}$ have a similar explosive growth phase as systems with $f = 0$. Initially, 100 km planetesimals slowly accrete pebbles and the occasional planetesimal. Once their masses exceed $10^{23} - 10^{24}$ g, the runaway quickly carries them to super-Earth ($M_0 = 45 M_\oplus$, thick orange curve) to super-Mars ($M_0 = 15 M_\oplus$, thin orange curve) masses. Unlike the systems in Fig. 5, the lack of solids with masses intermediate between planetesimals and pebbles allows protoplanets to accrete a large fraction of the mass in their respective annuli. Oligarchic growth is limited. Protoplanets maintain roughly constant masses for the rest of the calculation.

As the initial mass in pebbles drops, protoplanets grow more slowly and just manage to reach the mass of Mars (Fig. 6, green and purple curves in the upper panel). Systems with $f \approx 0.5$ produce many Pluto-mass planets in 10–100 Myr. Continued accretion of pebbles and leftover planetesimals during an extended oligarchic growth phase enables protoplanets to match the mass of Mars. When $f \approx 1$, it takes 1–3 Gyr for several protoplanets to exceed the mass of Pluto. This time scale is close to the estimate derived from scaling previous calculations in 30–150 au disks of solids (eq. 1). Oligarchic growth eventually carries some of these to the mass of Mars.

At 45 au, the behavior of rings with $3\text{--}10 M_\oplus$ and $f = 10^{-5}$ to $f = 1$ closely follows the evolution at 75 au (Fig. 6, lower panel). Although time scales are similar, the lower mass rings at 45 au prevent planets from reaching the same masses as the higher mass rings at 75 au. Thus, Mars-mass (Earth-mass) planets form in $3\text{--}10 M_\oplus$ ($15\text{--}45 M_\oplus$) rings at 45 au (75 au) in 30–100 Myr when $f \approx 10^{-4}\text{--}0.1$. For $f = 0.5$, time scales to reach Pluto-mass planets at 45 au are somewhat longer than at 75 au; Mars-mass planets take much longer, $\sim 3\text{--}10$ Gyr (green curves). Calculations with

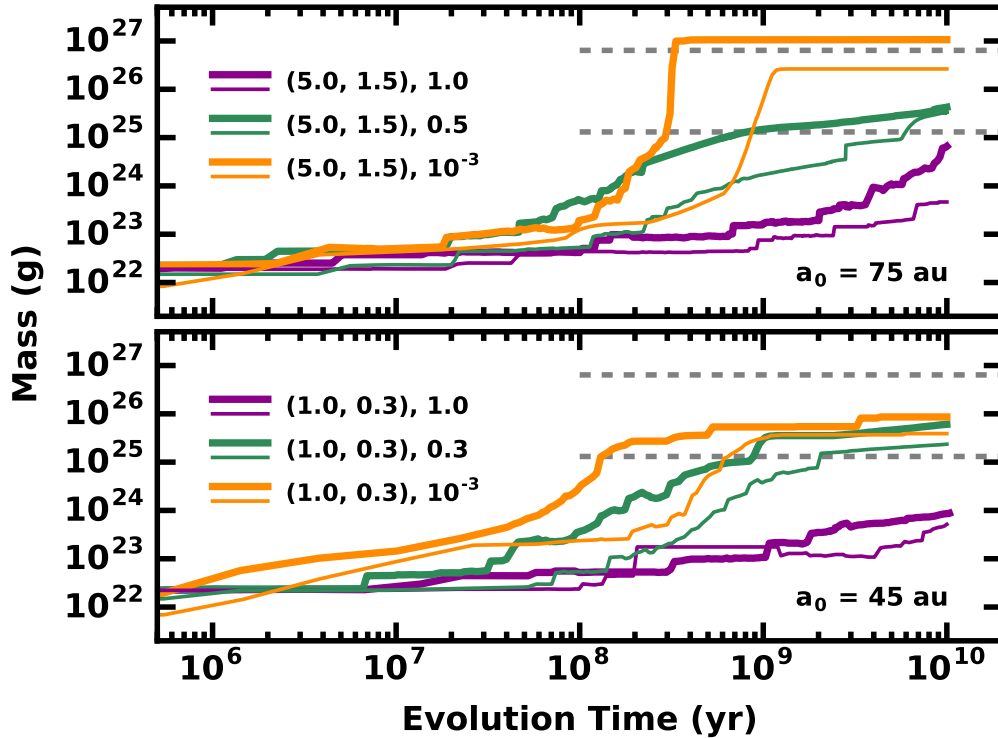


Figure 7. Growth of the largest objects in medium mass rings of solids at 45 au (lower panel) and at 75 au (upper panel). The legend associates M_0 and f for each curve. Numbers in parentheses indicate initial mass in M_\oplus for thick (first number) and thin (second number) lines. Horizontal dashed lines indicate the mass of Pluto (lower) and Mars (upper). The final mass of the largest object and the time scale to reach this mass scale inversely with M_0 : lower mass rings produce lower mass planets.

$f = 1$ (purple curves) yield a few Mars-mass planets only at the highest mass considered; lower mass systems manage to form planets with 3–5 M_P (Pluto masses).

When rings have less mass than the examples in Fig. 6, lower-mass planets form on longer time scales (Fig. 7). At 45 au (lower panel), rings with $M_0 = 1 M_\oplus$ ($0.3 M_\oplus$) and $0 < f < 1$ produce Pluto-mass planets on time scales of 100 Myr to 1 Gyr (green and orange curves). After 10 Gyr, the planets in these systems have masses of 2–10 M_P . Growth is negligible when $f = 1$ (purple curves); maximum masses are $\sim 0.1 M_P$. The more massive systems at 75 au easily generate Mars mass planets in 300 Myr to 1 Gyr when f is very small (Fig. 7, upper panel, orange curves). In each of these systems, planetesimals accrete nearly all of the available pebbles during runaway growth and then maintain a roughly constant mass for the rest of the calculation. As f increases, growth slows; the mass of the largest planets drops by several orders of magnitude (green and purple curves). When $f = 0.5$, Pluto mass planets form on 1–10 Gyr time scales. Very efficient planetesimal formation ($f = 1$) leads to the growth of Pluto mass planets at late times when $M_0 = 5 M_\oplus$; in lower mass rings, large planets fail to form after 10 Gyr.

Very low mass rings produce much smaller planets. Mixes of solids and pebbles with $M_0 = 0.01$ – $0.1 M_\oplus$ in rings at 45 au struggle to make a single Pluto. For any $f \neq 1$, the $M_0 = 0.1 M_\oplus$ models have a modest runaway that converts 200 km planetesimals into 900 km dwarf planets. Rings with a factor of three (ten) less mass produce several Charon-mass objects (Kuiper belt objects) with radii of 500 km (250 km). Rings with no pebbles barely evolve over 10 Gyr.

At 75 au, the lowest mass rings in our study show a little more activity. Models with $M_0 = 0.5 M_\oplus$ and $f \lesssim 0.1$ begin a robust runaway at 1 Gyr. After 3 Gyr, these rings have a modest set of dwarf planets with masses 5–10 times the mass of Pluto. When $f \approx 0.5$, the delay in the runaway to 3–6 Gyr fails to produce a Pluto-mass dwarf planet, but generates a few Charon-mass objects. As M_0 drops to 0.01– $0.1 M_\oplus$, growth is modest, yielding a few 200–300 km objects in $0.1 M_\oplus$ rings and many 150 km planetesimals in $0.01 M_\oplus$ rings. Once again, systems with $f = 1$ barely evolve over the age of the universe.

To collate some results from the calculations in a convenient form, Tables 1–2 in the Appendix list the time scale to form at least one Pluto-mass planet, t_{1k} ; the maximum radius r_{max} of the largest planet at 10 Gyr, the final mass in solids M_f at the end of each calculation, and other useful parameters. In addition to examining the relation between t_{1k} , M_0 , and f , the discussion in the Appendix includes several examples of collisional damping and some comparisons with previous calculations.

3.4. Evolution of Dust Luminosity

Throughout each calculation, the dust luminosity depends on the vertical scale height and the surface area of small solids. Initially, pebbles and planetesimals have the same typical orbital inclination, $i_0 = 5 \times 10^{-4}$. At large distances $a = 30\text{--}90$ au, the upper and lower surfaces of the swarm intercept a negligible fraction of stellar flux (e.g., Kenyon & Hartmann 1987; Chiang & Goldreich 1997). The maximum stellar luminosity intercepted by pebbles is then the fraction of solid angle subtended by a ring with vertical scale height H above and below the midplane at distance a from the central star: $L_{d,max} = H/a = 5 \times 10^{-4}$ for the adopted $i_0 = 5 \times 10^{-4}$. Ignoring the negligible contribution from large planetesimals for rings with any f the initial dust luminosity is:

$$L_{d,0}/L_\star \approx \begin{cases} 7.3 \times 10^{-4} (1-f) \left(\frac{M_0}{M_\oplus}\right) & a = 45 \text{ au}, M_0 \lesssim 0.7 M_\oplus \\ 1.9 \times 10^{-4} (1-f) \left(\frac{M_0}{M_\oplus}\right) & a = 75 \text{ au}, M_0 \lesssim 2.6 M_\oplus \end{cases} \quad (2)$$

When M_0 exceeds the limits quoted in eq. 2, $L_{d,0}/L_\star = 5 \times 10^{-4}$.

These expressions for L_d/L_\star establish clear constraints on plausible evolutionary paths for rings of pebbles and planetesimals. To exceed the FEPS upper limits of $L_d/L_\star \approx 10^{-4}$ for young stars with ages $\lesssim 100$ Myr, rings at 45 au (75 au) must have initial masses $M_0 \gtrsim 0.15 M_\oplus$ ($0.5 M_\oplus$). Lower mass disks require additional dust production from a collisional cascade. Among older stars, exceeding the *Herschel* upper limits of $L_d/L_\star \approx 3 \times 10^{-6}$ requires much less mass, $M_0 \gtrsim 0.005 M_\oplus$ ($0.02 M_\oplus$) at 45 au (75 au). If the time evolution of L_d/L_\star is slow, the small *Herschel* upper limits allow a broader set of rings to match observed systems.

As each calculation proceeds, the dust luminosity responds to changes in H and the surface area of small solids. When $f \lesssim 10^{-2}$, collisional damping initially reduces H by a factor of 2–5. Debris production is minimal; L_d/L_\star drops as H falls. As planetesimals accrete more and more pebbles, stirring (damping) becomes more (less) efficient. Debris production and H begin to grow; L_d/L_\star rises. Rings of solids with larger f have more stirring from growing planetesimals and less damping. The dust luminosity then rises at the start of each calculation. In all systems, H eventually reaches a maximum; debris generated from collisions of protoplanets and planetesimals falls below the loss of small particles from the collisional cascade. The dust luminosity then fades with time.

The top panel of Fig. 8 illustrates the smooth evolution of the relative dust luminosity L_d/L_\star for a set of calculations with $f = 0.5$ at 75 au. When half of the initial mass is in pebbles, the initial L_d/L_\star ranges from $L_d/L_\star \sim 10^{-6}$ for $M_0 = 0.01 M_\oplus$ to 5×10^{-4} for $M_0 = 2.6\text{--}45 M_\oplus$ (eq. 2). As the most massive rings evolve (15–45 M_\oplus , black and purple curves), stirring overcomes collisional damping; H increases. Despite the lack of debris production from planetesimal growth, L_d/L_\star grows with time. Over the next 10–30 Myr, increased debris production roughly balances losses from the collisional cascade; L_d/L_\star remains roughly constant. As protoplanet growth slows considerably at 100–200 Myr, stirring initiates a stronger cascade that removes more and more of the remaining small solids. The dust luminosity then begins a roughly linear decline. With more massive protoplanets that form earlier and stir solids more strongly, the 45 M_\oplus rings begin to decline before the 15 M_\oplus rings. Once the strong cascade begins, L_d/L_\star follows the same roughly linear decline in both systems.

Lower mass models have a similar behavior. In rings with 0.5–5 M_\oplus (light green, dark green, and blue curves), the dust luminosity slowly declines with time during most of the first 100 Myr to 1 Gyr of evolution. During this decline, protoplanets gradually reach the mass of Pluto. Stirring from these large solids increases H . Larger relative velocities enhance debris production, but mass removal from the cascade keeps L_d/L_\star falling. Eventually, stirring becomes more effective; the cascade strengthens and removes more and more small solids from the ring. The dust luminosity then declines more rapidly, joining the roughly linear decline of the higher mass models.

In the lowest mass models (0.01–0.1 M_\oplus , beige and orange curves), the evolution is extremely slow. Over 10 Gyr, planetesimal masses grow by a factor of 3 (0.01 M_\oplus) to 30 (0.1 M_\oplus). The collisional cascade is equally weak; the dust luminosity changes little over 10 Gyr. Early in the evolution (1–10 Myr), these systems show a small rise in L_d/L_\star due to the extra production of small dust grains relative to the loss of pebbles. The systems then begin a protracted

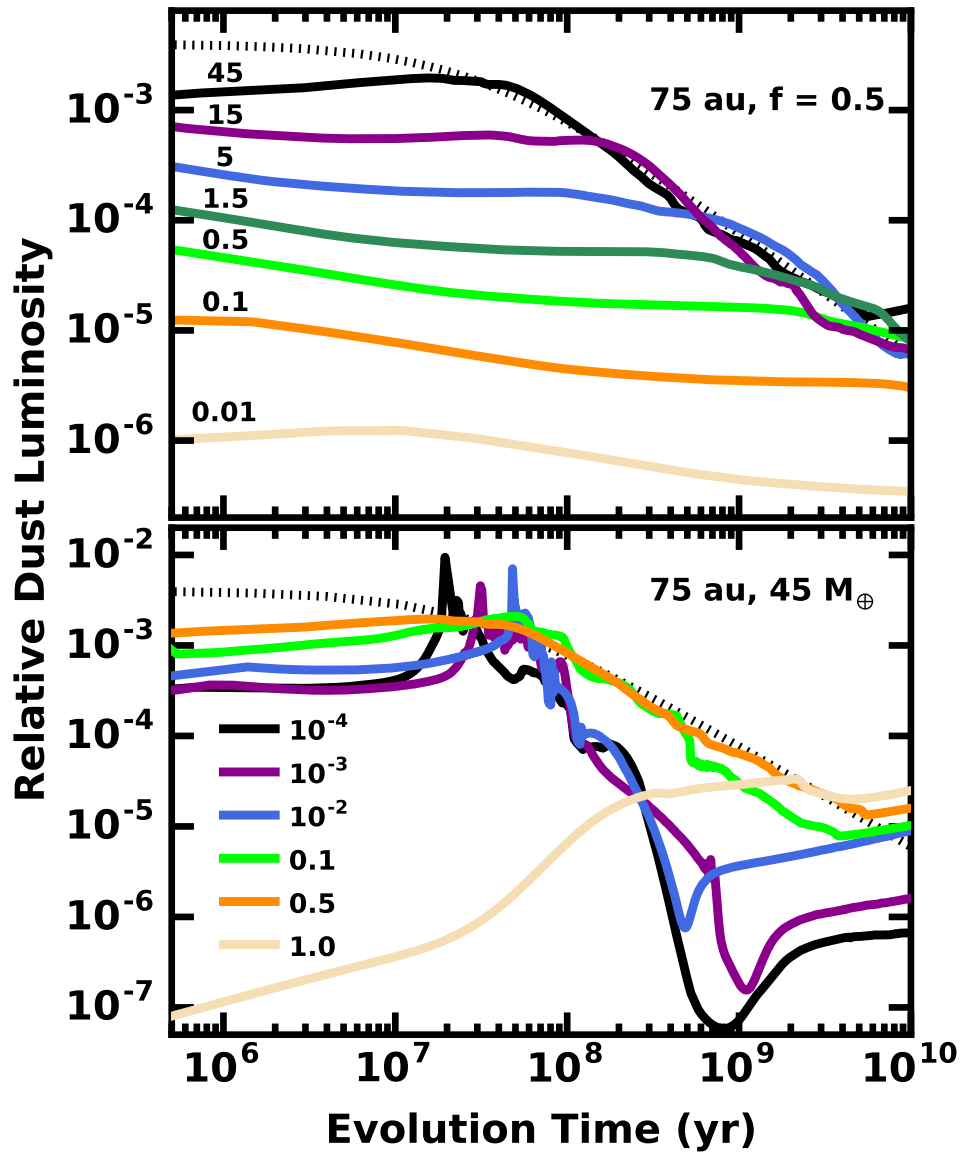


Figure 8. Evolution of the relative dust luminosity L_d/L_* for rings at 75 au. In each panel, the dotted line shows the evolution predicted by an analytical model where $L_d/L_* \propto L_0(1 + t/t_0)^{-\alpha}$ with $\alpha = 1.12$ (Kenyon & Bromley 2017). *Upper panel:* For models with $f = 0.5$, the value for M_0 is listed to the left of each curve. Systems with $M_0 \gtrsim 1.5 M_\oplus$ have a period of constant L_d/L_* followed by a t^{-1} decline. In lower mass systems, L_d/L_* is roughly constant over 10 Gyr. *Lower panel:* For models with $M_0 = 45 M_\oplus$, the legend lists f for each curve. Systems with $f = 1$ evolve slowly to a maximum $L_d/L_* \sim 10^{-5}$. When $f \approx 0.1$ – 0.5 , L_d/L_* gradually drops from $\sim 10^{-3}$ to 10^{-5} . Rings of solids with $f \lesssim 10^{-2}$ start fainter, abruptly rise to $L_d/L_* \approx 10^{-2}$ and then dramatically fall to $L_d/L_* \lesssim 10^{-6}$. Collisions between pairs of protoplanets occasionally produce spikes in L_d/L_* .

decline. Were the calculations extended to 20–30 Gyr, the decline in L_d/L_* would speed up and eventually join the other models on a roughly linear decline of L_d/L_* with time.

Compared to the models with $f = 0.5$, systems with small f undergo a more erratic evolution (Fig. 8, lower panel). When massive rings have $f \approx 10^{-4}$ – 10^{-2} , runaway growth is explosive; protoplanets rapidly reach super-Earth masses (Figs. 5–6). The dust luminosity echoes this behavior (black, purple, and blue curves). Initially, L_d/L_* drops by a factor of ~ 2 – 5 as collisional damping among pebbles reduces the scale height of the smallest solids. After the runaway

begins, protoplanets stir up smaller solids; the cascade starts to produce copious amounts of debris. With more debris and a larger scale height, the dust luminosity rises dramatically to $\sim 10^{-2}$ and then drops precipitously as the cascade depletes the rings of pebbles and smaller solids. During the steep decline, protoplanet–protoplanet collisions replenish the debris and produce additional brief rises in L_d/L_\star . After a nearly Gyr-long decline, a few large collisions create enough debris to fuel a final, modest rise in the dust luminosity, $L_d/L_\star \sim 10^{-6} - 10^{-5}$ that lasts until ~ 10 Gyr.

Calculations with $f \lesssim 10^{-4}$ behave in a similar fashion. Early on, damping is more important; L_d/L_\star declines by a factor of 10–20. As km-sized planetesimals evolve into super-Earths, rapid growth of H allows L_d/L_\star to reach $\sim 10^{-2}$ somewhat earlier than models with $f = 10^{-4} - 10^{-2}$. In these systems, the drop in L_d/L_\star is more dramatic, falling well below 10^{-7} , and the recovery is smaller than displayed by the black, purple, and blue curves in the lower panel of Fig. 8.

Rings with a larger initial mass in planetesimals, $f = 0.1\text{--}0.5$, evolve more smoothly (light green and orange curves). In these systems, L_d/L_\star rises by a factor of four during the first 10–20 Myr when planetesimals grow into Pluto-mass planets (Fig. 6). While protoplanets continue to accrete pebbles, the dust luminosity levels off and begins to decline. The systems then enter an extended oligarchic growth phase from ~ 100 Myr to 10 Gyr, where the dust luminosity declines roughly linearly with time, from $L_d/L_\star \sim 10^{-3}$ to $L_d/L_\star \sim 10^{-5}$. Near the end of this epoch, both calculations exhibit a small rise in L_d/L_\star from several collisions among the remaining planetesimals and protoplanets.

When $f = 1$, the ponderous evolution of L_d/L_\star closely parallels the slow growth of planetesimals into Mars-mass planets (Fig. 8, beige curve). During the first 30 Myr, L_d/L_\star rises slowly from $\sim 10^{-9}$ to $\sim 10^{-6}$. Growth of planetesimals and a rise in debris production powers a more rapid rise to $L_d/L_\star = \text{a few } \times 10^{-5}$ at 200–300 Myr. The system then enters oligarchic growth, where protoplanets continue to grow and the cascade grinds leftovers to dust. Unlike other systems with smaller f , these rings maintain a roughly constant luminosity from 300 Myr to 10 Gyr. Eventually, the dust luminosity will decline; however, the decline will occur after the central star leaves the main sequence.

When the initial mass in solids is smaller than $45 M_\oplus$, the evolution of the dust luminosity in models with $f \lesssim 10^{-2}$ is slower and less dramatic. The overall shape in the $L_d(t)/L_\star$ curve follows the examples in the top panel of Fig. 8, with a fairly constant L_d/L_\star at the start of the calculation followed by a nearly linear decline. Superimposed on this generic evolution is a series of spikes in L_d/L_\star generated by debris from occasional giant collisions between protoplanets and planetesimals. The amplitudes of these spikes decline with decreasing initial mass in solids. Rings with $M_0 = 10 M_\oplus$ at 45 au and $M_0 = 15 M_\oplus$ at 75 au have large spikes as in the black, purple, and blue curves in the lower panel of Fig. 8, while rings with $0.3\text{--}1 M_\oplus$ at 45 au and $0.5\text{--}1.5 M_\oplus$ at 75 au have modest spikes. Lower mass systems have insignificant spikes in L_d/L_\star during the overall decline.

In systems with $f = 1$, the evolution in L_d/L_\star becomes less and less interesting with decreasing M_0 . Rings with $M_0 \gtrsim 1 M_\oplus$ ($5 M_\oplus$) at 45 au (75 au) have $L_d/L_\star \gtrsim 10^{-6}$ at 5–10 Gyr. As M_0 decreases from these limits, the maximum dust luminosity also drops. At 45 au, the maximum dust luminosity falls to 3×10^{-7} for $0.3 M_\oplus$ rings to less than 10^{-7} for $0.01 M_\oplus$ rings. Low mass rings at 75 au are equally invisible with current technology; all systems with $M_0 \lesssim 0.5 M_\oplus$ have a maximum L_d/L_\star smaller than 10^{-7} . The tables in the Appendix include the maximum L_d/L_\star for all calculations and allow for a more extensive comparison among the calculations.

To connect these results to previous studies, we compare with published analytical models of collisional cascades (e.g., Wyatt & Dent 2002; Dominik & Decin 2003; Krivov et al. 2008; Löhne et al. 2008). In a cascade at 75 au where the radius r_c of the largest object participating in the cascade does not change, the dust luminosity is constant at early times and then falls linearly with time, $L_d/L_\star = L_0/(1 + t/\tau_0)$. However, numerical models demonstrate that r_c also declines with time (e.g., Kenyon & Bromley 2017). Including this behavior in the analytical model yields a steeper decline in the dust luminosity, $L_d/L_\star = L_0/(1 + t/\tau_0)^{1.12}$, where $\tau_0 = 1.12\alpha t_0$ and $t_0 = r_c \rho P / 12\pi \Sigma$ is the collision time (Kenyon & Bromley 2017). The α term is a function of the ratio of the collision energy to the binding energy of planetesimals.

The dotted line in each panel of Fig. 8 shows the luminosity evolution for $L_0 = 4 \times 10^{-3}$ and $t_0 = 30$ Myr. The dust luminosity is nearly constant for 5–10 Myr and then declines. Although the analytical model has a somewhat larger L_d/L_\star at early times, it matches numerical models for massive disks with $f = 0.1\text{--}0.5$ at late times. Tracking the behavior of the numerical models for less massive disks requires smaller L_0 and larger t_0 .

In the Kenyon & Bromley (2017) analytical model, the reference luminosity L_0 and the time scale τ_0 depend primarily on M_0 and r_c : $L_0 \propto M_0 r_c^{-1/2}$ and $\tau_0 \propto r_c M_0^{-1}$. For the cascade in Fig. 8, the collision velocity is just large enough to shatter objects with $r \approx r_c$; then, $r_c \approx 0.2\text{--}0.5$ km and $M_0 \approx 50\text{--}55 M_\oplus$. For fixed r_c , reducing L_0 by a factor of 100

yields $M_0 \approx 0.5 M_\oplus$ and $t_0 \approx 3$ Gyr. This model provides a reasonable match to numerical calculations with $M_0 \approx 0.1\text{--}0.5 M_\oplus$.

Analytic cascade models with the larger planetesimals expected from streaming instability models, e.g., $r_c \approx 100\text{--}200$ km, require unreasonably large M_0 to approximate the evolution in Fig. 8 (see also Shannon & Wu 2011; Krivov & Wyatt 2021). Adopting $r_c \approx 100$ km instead of $r_c \approx 0.3$ km requires ~ 17 times more mass to achieve $L_0 \approx 4 \times 10^{-3}$. To match the short collision time, $\tau_0 \approx 30$ Myr, collision velocities must be $\sim 3\text{--}4$ times larger than the minimum required to shatter 100 km objects. While this model provides a reasonable match to the simulation, the high mass in solids, $M_0 \approx 800\text{--}900 M_\oplus$, makes this solution unattractive compared to the analytical model with small planetesimals or the numerical model with a mix of pebbles and large planetesimals.

Although not shown in Fig. 8, analytic models also match the results of numerical models at 45 au. For $M_0 = 10 M_\oplus$ and $r_c = 0.2$ km, an analytical model with $L_0 \approx 2 \times 10^{-3}$ and $\tau_0 \approx 25$ Myr tracks the numerical models of disks with $f = 0.1\text{--}0.3$ for evolution times exceeding 30–40 Myr. Lower mass disks with larger τ_0 also match the simulations. Compared to calculations at 75 au, the analytic model prefers a somewhat smaller r_c and shorter τ_0 to track the numerical results adequately at 45 au. Once again, much larger r_c requires unreasonably large M_0 .

3.5. Gap Formation

In addition to the dust luminosity, the coagulation calculations provide a quantitative measure of the radial distribution of dust as a function of time. For low mass rings that generate little dust luminosity, $L_d/L_\star \lesssim 10^{-4}$, final protoplanet masses are typically less than the mass of Mars. These planets tend to follow the initial surface density distribution and cluster near the center of the ring. With little mass in planets, the dust also has a gaussian distribution in surface density with a peak in the center of the ring, e.g., at 45 au and at 75 au.

More massive rings have more obvious features in the radial surface density of the dust. The planets in these calculations do not follow the initial surface density distribution and are more evenly distributed among the 28 annuli in each ring. Super-Earth mass planets tend to eliminate all solids from their annuli and sometimes from adjacent annuli. These systems thus have 1–3 au gaps in the surface density of dust along the orbits of the super-Earths. Rings with several super-Earths have multiple gaps.

Predicting the structure of these gaps requires a parallel set of coagulation and n -body calculations to allow the gravity of planets to open gaps with sizes that depend on the mass of the planet and the remaining mass in smaller solids within the ring (e.g., Kokubo & Ida 1995; Rafikov 2001; Bromley & Kenyon 2011b, 2013, and references therein). These calculations are computationally expensive (e.g., Bromley & Kenyon 2020; Kenyon & Bromley 2021); we defer them to a later study. Here, we use previous results to infer the likely structure of gaps in the dust distribution of rings with massive planets.

For this initial exploration of gap formation, we compare the relative separation of protoplanet orbits to the Hill radius, $r_H = a(M/M_\star)^{1/3}$. From analytic and numerical calculations, planets clear out a ‘ring of influence’ with a radial extent $\delta a \approx 2\sqrt{3}r_H$ on either side of their orbits (e.g., Gladman 1993; Kokubo & Ida 1995; Rafikov 2001). Among pairs of protoplanets, those separated by more than $4 r_H$ in semimajor axis do not interact dynamically (e.g., Kokubo & Ida 1995; Chambers et al. 1996; Weidenschilling et al. 1997; Chambers 2001; Bromley & Kenyon 2006; Kenyon & Bromley 2006); each carves out its own gap with an extent comparable to δa . Protoplanets on closer orbits interact dynamically and produce large gaps in an ‘interaction region’ defined by the extent of their chaotic orbits prior to a merger or ejection event. This region has a width of $2\text{--}3\delta a$.

Fig. 9 illustrates the evolution for a calculation with $M_0 = 45 M_\oplus$ and $f = 0.01$. With a surface density maximum in the middle of the ring, planets grow fastest (slowest) at 75 au (60–65 au and 85–90 au). Once 500–600 km protoplanets form at 30 Myr, runaway growth begins. Over the next 70 Myr, the five fastest-growing protoplanets each surpass the mass of Mars. Smaller protoplanets have much smaller masses, $\sim 1\text{--}30 M_P$. The horizontal lines in the figure illustrate the extent of the rings of influence for each of the five largest protoplanets. Rings of influence for the two most massive protoplanets at 73–75 au overlap and contain a lower mass protoplanet at 72 au. Rings of influence for the other two protoplanets at 67 au and at 81 au contain several much smaller planetesimals but no other massive protoplanet.

The close proximity of the two largest protoplanets in Fig. 9 has two observable outcomes. Initially, the two central protoplanets interact dynamically, scattering smaller solids out of their orbits and trying to move to a larger separation. This interaction involves the protoplanet at 72 au and begins a period of chaotic growth, where the three protoplanets at 72–75 au move chaotically through the grid and sweep up smaller objects along their orbits. Eventually, this process

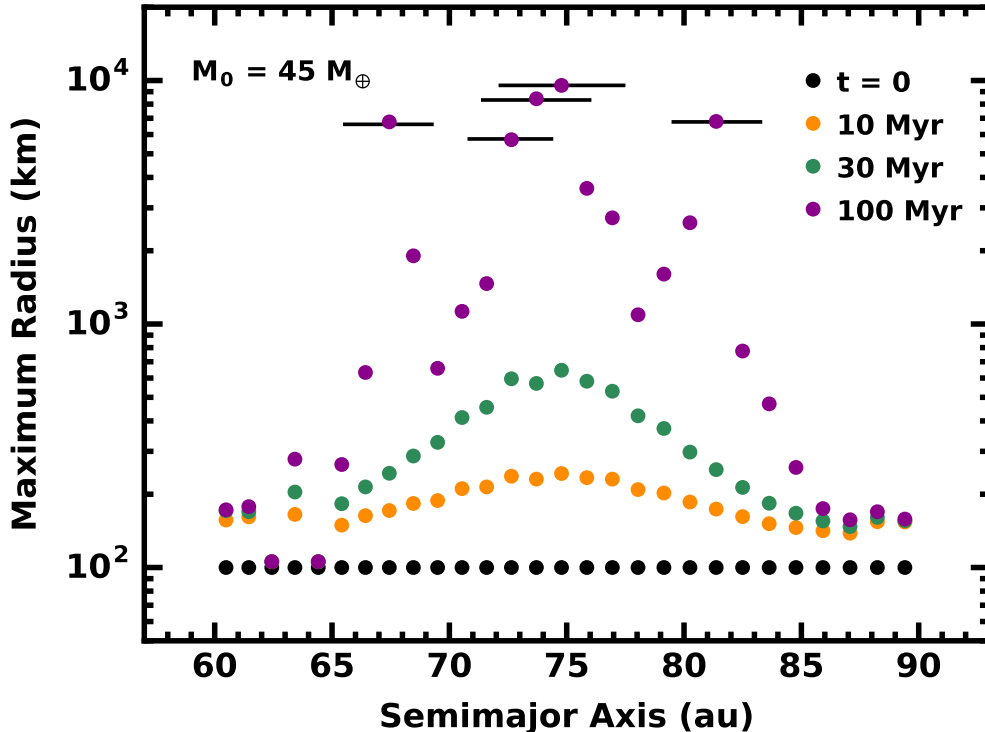


Figure 9. Radius of the largest object in each annulus for rings of solids with $M_0 = 45 M_\oplus$ and $f = 0.01$ for times listed in the legend. Horizontal lines extending from several points in each panel indicate the extent of the ‘ring of influence’, which has a radial extent of $3.5 r_H$ around the orbit of each planet. Rings of influence for all protoplanets are omitted for clarity. At the center of the grid, the largest planetesimals slowly grow from 100 km to 200 km (10 Myr) to 700 km (30 Myr). Runaway growth leads to the formation of four protoplanets with $M \gtrsim 0.1 M_\oplus$ and another with $M \approx 0.05 M_\oplus$. The overlapping rings of influence suggest dynamical interactions will begin a phase of chaotic growth where the largest protoplanets merge into one or two super-Earths.

involves the outer two protoplanets at 67 au and 81 au. Subsequent collisions and mergers among the five largest protoplanets, the smaller protoplanets with radii $\sim 1000\text{--}4000$ km, and the smaller planetesimals are likely to leave behind one or two super-Earth mass planets (e.g., Goldreich et al. 2004; Kenyon & Bromley 2006). Throughout chaotic growth, the ring of smaller solids expands radially inward and outward. Thus, at $\gtrsim 200$ Myr, ALMA observations would reveal thermal emission from a larger ring of small solids with a central depression where the remaining super-Earths orbit.

In this example, it seems likely that the size of the gap will be larger than the standard $4\sqrt{3}r_H$ expected for a *single* massive planet in a ring of small solids. The five protoplanets at 67–82 au would experience chaotic growth within an ‘interaction region’ extending from ~ 65 au to ~ 83 au. Once chaotic growth ends, this region would have few small solids. Instead of the $\sim 50 M_\oplus$ single planet required to create such a large gap, this gap would contain 1–2 super-Earths with a total mass $\sim 5 M_\oplus$.

Among the suite of calculations with $M_0 = 10 M_\oplus$ at 45 au and $M_0 = 15\text{--}45 M_\oplus$ at 75 au, many have protoplanets with overlapping rings of influence (Fig. 10). At 45 au (left panel), two systems have as many as a half dozen protoplanets within an interaction region (top left and middle left panels). Another system has ~ 20 large objects in an interaction region that takes up most of the ring. Calculations at 75 au yield similar systems where a few or many massive objects will interact chaotically. Some may yield 1-2 super-Earths; others may produce many Mars-mass planets.

In each of these calculations, we expect that chaotic evolution will produce gaps and perhaps narrow rings of small solids within broader, more diffuse rings. With many massive protoplanets evolving within the interaction region, the final sizes of dark gaps may be much larger than expected from the final masses of protoplanets.

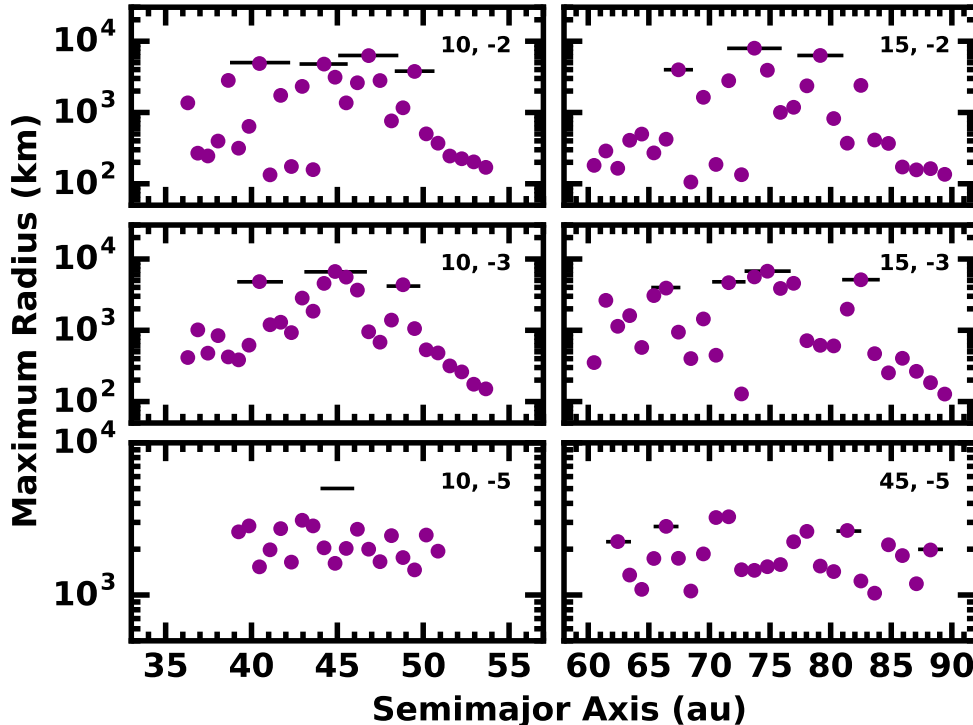


Figure 10. Snapshots of the largest protoplanets in each annulus at 1–10 Gyr for rings at 45 au (left panels) and at 75 au (right panels). The upper right corner of each panel lists M_0 and $\log f$. Horizontal lines indicate rings of influence for several protoplanets in each panel. Rings of influence for all protoplanets are omitted for clarity.

Lower mass rings are unlikely to have much structure. The protoplanets in these systems are not massive enough to scatter small solids out of their orbits and cannot generate a significant gap in the ring. With little scattering, the final extent of the ring should be similar to the initial extent.

4. DISCUSSION

The models described in Section 3 illustrate how the collisional evolution of rings of solids—composed of pebbles and planetesimals—follow diverse evolutionary histories depending on the efficiency of planetesimal formation (f) and the initial mass in solids (M_0). These parameters establish whether rings can grow Pluto-, Mars-, or super-Earth-mass planets in 1 Myr to 10 Gyr (Section 3.3; Figs. 5–7; see also Appendix Tables 1–2). Diverse dust luminosity histories result (Section 3.4; Fig. 8). The growing planets should create gaps in the radial distribution of solids that reflect their mass and growth history (Section 3.5; Figs. 9–10).

Here we compare the model results from Section 3 with observations of debris disks to identify the plausible initial conditions and evolutionary paths that connect protoplanetary disks to debris disks (Fig. 4). We also associate planet formation outcomes—Pluto, Mars, or (super-)Earth—with the various paths to debris disks. Fig. 11 compares the fractional luminosity L_d/L_\star of the ring models (colored lines) with the observed L_d/L_\star values of debris disks described in Section 2. In each panel, the colored dots from Fig. 3 are reproduced as black dots; grey arrows repeat the median upper limits from Fig. 3. The comparison demonstrates that the evolution of massive rings of pebbles and planetesimals at 45–75 au plausibly explains the observed dust luminosities of known debris disks with stellar ages of 10 Myr to 10 Gyr.

4.1. Bright young disks

As shown in the two panels of Fig. 11, the population of bright young disks ($L_d/L_\star \gtrsim 10^{-3}$ at 10–100 Myr) is best matched by models of high mass rings (3–45 M_\oplus) with a wide range of planetesimal formation efficiencies ($f = 0$ –0.5). In models with $f \lesssim 10^{-2}$, occasional collisions among large protoplanets create copious debris and pronounced spikes in L_d/L_\star (Fig. 11, purple curve in the lower panel). The largest spikes rival the observed L_d/L_\star of the brightest debris

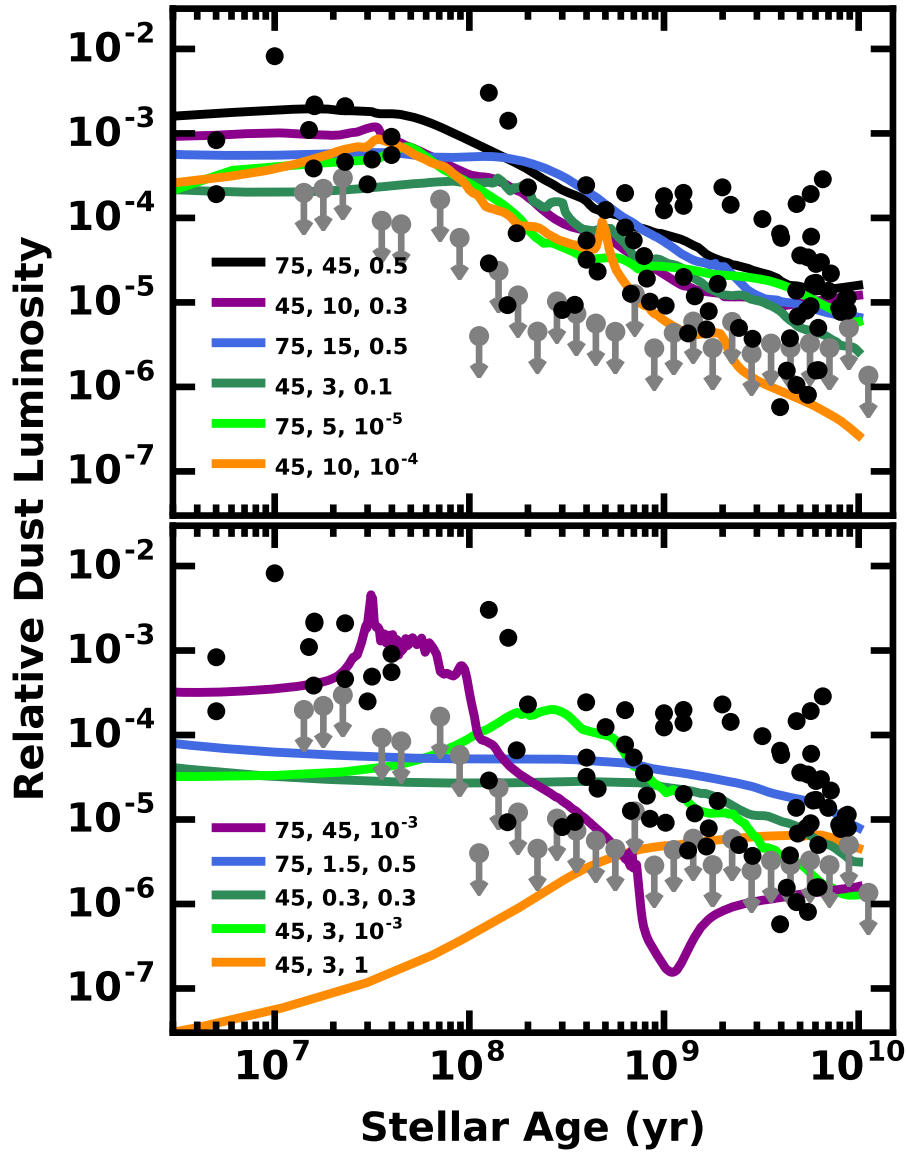


Figure 11. Comparison of the relative dust luminosity derived from the numerical calculations (solid lines) with detections (black points, instead of blue, green and purple points) and upper limits (grey symbols) from Fig. 3. The legend associates values of a_0 , M_0 , and f with each model curve. In the upper panel, a set of ‘bright stalwart’ models passes through the ensemble of data points. In the lower panel, ‘early flare’ (purple curve), ‘steady glow’ sources (blue, light green, and dark green curves), and ‘late bloomers’ (orange curve) pass through the data for young stars (ages $\lesssim 100$ Myr, early flare) or old stars (ages $\gtrsim 100$ Myr, steady glow sources and late bloomers) but not both.

disks with ages of 10–100 Myr (upper panel; 75 au). Fainter debris systems in this age range are well matched by rings with smaller masses, smaller radii, or smaller f (Fig. 11, upper panel).

In contrast to these evolutionary paths, rings with similar or larger masses, but completely efficient planetesimal formation ($f=1$) produce very little debris at early times (Fig. 11, orange curve in the lower panel). If planetesimals form with such high efficiency, matching the observed fractional luminosities of the bright young disks requires very large initial masses ($\sim 1000 M_{\oplus}$; Shannon & Wu 2011; Krivov & Wyatt 2021). As shown here, such large masses are

unnecessary; more modest planetesimal formation efficiencies and the typical masses of observed protoplanetary disk rings can account for the observed properties of bright young disks.

4.2. Fainter old disks

Debris disks trend fainter with age, with $L_d/L_\star \sim 10^{-5}$ at ages beyond 1 Gyr (Figs. 2, 3, and 11). The downward trend of L_d/L_\star with age is readily explained by the simple fading of the bright young disks of Section 4.1. Rings with $f \approx 0.01$ – 0.5 follow the classical evolution in dust luminosity of $L_d/L_\star \propto t^{-1}$ (see also Wyatt & Dent 2002; Dominik & Decin 2003; Krivov et al. 2008; Löhne et al. 2008; Wyatt 2008; Kenyon & Bromley 2017) via the evolutionary pathway illustrated by nearly all of the curves in the upper panel of Fig. 11. We identify this evolution as the “bright stalwart” pathway shown in Fig. 12. This interpretation of the known debris disks—that they arise from the fading of a population of initially massive disks partially composed of pebbles and planetesimals—is consistent with the similar fraction of debris disks and protoplanetary disk rings at each evolutionary age ($\sim 25\%$; Section 2). Thus, the bright stalwart pathway accounts for both the incidence rates and luminosities of the known debris disks in the age range ~ 50 Myr to 10 Gyr.

The general agreement of this evolutionary path with the observed properties of debris disks potentially limits the possible role of other evolutionary histories. For example, the fainter old disks could also be explained with a population of low mass rings ($\sim 1 M_\oplus$) with modest f that are moderately bright at early times ($L_d/L_\star \sim 10^{-4}$) and evolve more horizontally in Fig. 11, reaching $L_d/L_\star \sim 10^{-5}$ at 10 Gyr. This pathway—which we refer to as ‘steady glow’—is illustrated by the green and blue curves in the lower panel of Fig. 11 (also the gold curve in Fig. 12). Alternatively, high mass disks (10 – $40 M_\oplus$) made entirely of planetesimals pursue a stealthy evolutionary path that is extremely faint at early times ($L_d/L_\star < 10^{-6}$) and brightens at late times to currently observable levels of $L_d/L_\star \sim 10^{-5}$. The orange curve in the lower panel of Fig. 11 (also in Fig. 12) shows this ‘late bloomer’ pathway.

If we assume that $\sim 25\%$ of stars start out with massive protoplanetary disk rings (Section 2) and subsequently follow the bright stalwart path, we can account for the observed luminosities and incidence rates of debris disks with age; this assignment leaves little room for significant contribution from the steady glow and late bloomer pathways. If these were important pathways, each populated roughly equally to the classical bright stalwart pathway, the incidence rate of debris disks at early times (from the bright stalwart pathway) would be three times smaller than the rate at late times when the steady glow and late bloomer populations become detectable with $L_d/L_\star \sim 10^{-5}$ at ~ 1 Gyr. We can further rule out a significant steady glow population, because it would also overproduce sources at ages of 0.1–1 Gyr with $L_d/L_\star \approx 10^{-4}$. The debris disk incidence rate in this age and luminosity range is restricted by the *Herschel* survey upper limits (Section 2). Future debris disk surveys that reach fainter luminosity limits at ages 10–300 Myr can provide additional, direct constraints on the steady glow ($L_d/L_\star \sim 10^{-5}$) and late bloomer ($L_d/L_\star \sim 10^{-6}$) populations.

One can imagine combining the evolutionary tracks from Section 3 in other ways. For example, if the incidence of cold debris disks at 10–30 Myr is as large as the 50% rate derived for the small population of F stars in the 20–25 Myr old β Pic moving group (Pawellek et al. 2021), a significant population of disks must rise to high dust luminosity within a few tens of Myr before fading significantly beyond 100 Myr. This behavior, which we identify as the ‘early flare’ pathway, could explain the high incidence rate of cold debris disks at young ages and the much lower rate among stars with ages $\gtrsim 50$ Myr. In the calculations, this behavior occurs in rings with high masses and $f \lesssim 10^{-3}$, where the combined impact of damping, rapid planet growth, and an efficient cascade results in a system where L_d/L_\star rises from $\lesssim 10^{-4}$ to $\sim 10^{-2}$ and declines back down to $\lesssim 10^{-4}$ on time scales of 100 Myr (Fig. 8, lower panel, black, purple, and blue curves; Fig. 12, green curve). The late decline in L_d/L_\star in these models is as fast or faster than the $L_d/L_\star \propto t^{-2}$ required to eliminate the descendants of the β Pic stars from the DEBRIS and DUNES samples at ages of ~ 1 Gyr (Pawellek et al. 2021).

We might further imagine that in addition to the early flare pathway producing the vast majority of the luminous debris disks at ages $\lesssim 40$ – 50 Myr, we also have the steady glow and late bloomer pathways dominating among much older stars. With this combination, nearly all of the early flares need to fall below current detection limits before rings in the steady glow and late bloomer pathways begin to contribute to the population. Contributions from the classical bright stalwart pathway could ‘smooth over’ the transition between these pathways.

Invoking three pathways—early flare, steady glow, and late bloomer—faces several hurdles. Selecting the proper mix to ensure a high incidence rate at the youngest ages and to maintain a roughly constant rate of $\sim 25\%$ for all older stars would require some fine tuning for ages where early flares are fading away and the other pathways first become detectable. In addition, the required mix of initial conditions: massive disks with $f \approx 0$ for early flares, massive disks

with $f = 1$ for late bloomers, and intermediate-mass disks with $f \approx 0.1$ – 0.5 for steady glow sources seems unlikely, unless there are physical mechanisms that can produce such dramatically different planetesimal efficiencies in different disks. The larger parameter space of f that produces the classical bright stalwart sources seems more plausible and more in line with the predictions of simulations of the streaming instability (e.g., Rucsa & Wadsley 2021).

We can also distinguish these pathways with a different approach, by quantifying the disk substructure created by any massive, embedded planets that form. Massive rings (10 – $40 M_{\oplus}$) that follow the classical bright stalwart pathway ($f=0.1$ – 0.5 ; Fig. 12, blue curve) or the late bloomer path ($f = 1$; Fig. 12, orange curve) would build Mars-mass planets by 10 Gyr. In contrast, massive rings with lower f that “burn bright, fade fast” (the early flare pathway; $f \lesssim 10^{-3}$; Fig. 12, green curve) would create more massive objects—super-Mars to super-Earth mass planets—in 20–30 Myr (Fig. 6). Modest-mass rings that follow the roughly horizontal steady glow pathway (~ 1 – $5 M_{\oplus}$, $f=0.3$ – 0.5 ; Fig. 12, gold curve) would only build Pluto-mass objects by 10 Gyr (Fig. 7).

The gaps created by the more massive planets could be resolved spatially. If a ring with a radius of 75 au creates a planet with the mass of Earth, Mars, or Pluto, the planet would open a gap with a fractional width of at least $2da/a = 4\sqrt{3}(M_p/M_{\odot})^{1/3}$ (Section 3), which corresponds to an angular width of 54 mas, 24 mas, and 8 mas at a distance of 140 pc. In comparison, the ngVLA is anticipated to deliver angular resolutions of 0.5 mas to 50 mas at wavelengths of 2.6 mm to 25 cm (e.g., Matthews et al. 2018; Tobin et al. 2018; Chalmers et al. 2020, and references therein).

Thus, future observations could test the hypothesis that the classical bright stalwart evolution is the primary pathway for debris disks, with few systems pursuing either the late bloomer or the steady glow paths. In other words, observations could probe whether protoplanetary disks are born with massive, initially dark rings of planetesimals (late blooming rings) or initially modest-mass rings of pebbles and planetesimals (steady glow rings).

4.3. *The Story of Solids in Disks*

If bright stalwarts dominate the evolutionary pathways for debris disks, one simple interpretation of the results described here is that extended and compact protoplanetary disks evolve differently, i.e., disks evolve horizontally in Fig. 4. The 25% of T Tauri systems with large ringed protoplanetary disks produce detectable debris throughout their lives, from ~ 10 Myr to 10 Gyr, and are the showy, attention-grabbing celebrities of the debris disk world. In contrast, the majority of T Tauri systems with compact protoplanetary disks live quieter, tidier lives. Few of them are born with ‘late-blooming’ massive, initially dark rings of planetesimals or ‘steady’ modest-mass rings of pebbles and planetesimals. That is, if rings are typically a mixture of pebbles and planetesimals at the end of the protoplanetary disk phase, then compact disks typically leave behind $< 1M_{\oplus}$ of solids at large radii, a small reservoir that produces little debris over the lifetime of the star. Instead of each disk evolving along the classical path of Class 0/I/II/III sources into debris disks (e.g., Cieza et al. 2007; Wahhaj et al. 2010; Williams & Cieza 2011; Hardy et al. 2015), this interpretation implies that the ‘known debris disks are a chapter in the history of only a subset of low mass stars.

While most current observations support this simple picture, the true story may be more complex if the high incidence rate of cold debris disks among the small sample of F stars in the β Pic moving group is typical of all 20–25 Myr old solar-type stars. As noted earlier, a high incidence rate of debris that persists for a short time may imply that a significant fraction of the compact protoplanetary disks actually possess massive rings of solids with very small f that are also undetectable because of their very small initial scale height (section 3.2). These disks would evolve into bright early flare sources that appear suddenly on the debris disk stage and quickly fade below current detection limits.

This potential complexity aside, the divergent debris-production histories of large and small protoplanetary disks connect back to the more fundamental question of what sets the initial distribution of solids in protoplanetary disks. One possibility is that some protoplanetary disks are born large and others small, a consequence of the initial angular momentum of the cloud core and the extent to which angular momentum is shed (or transported) as collapse proceeds (e.g., Terebey et al. 1984; Matsumoto et al. 1997; Basu 1998; Yorke & Bodenheimer 1999; Nakamura 2000; Krasnopolsky & Königl 2002; Tscharnuter et al. 2009; Joos et al. 2012; Tomida et al. 2015; Hennebelle et al. 2016; Zhao et al. 2020, and references therein). Alternatively, most disks may be born with similar (large) sizes, but some experience greater inward migration of solids and others do not. Disks that create planets (or other disturbances) early on, at large radii, can induce pressure bumps that trap solids and prevent inward migration (e.g., Pinilla et al. 2012; Zhu & Stone 2014; van der Marel et al. 2018). If bright stalwarts dominate the production of debris disks, one or more of these scenarios are efficient in concentrating or placing a significant solid mass (10 – $40 M_{\oplus}$) in rings at large radii in about 20%–25% of disks.

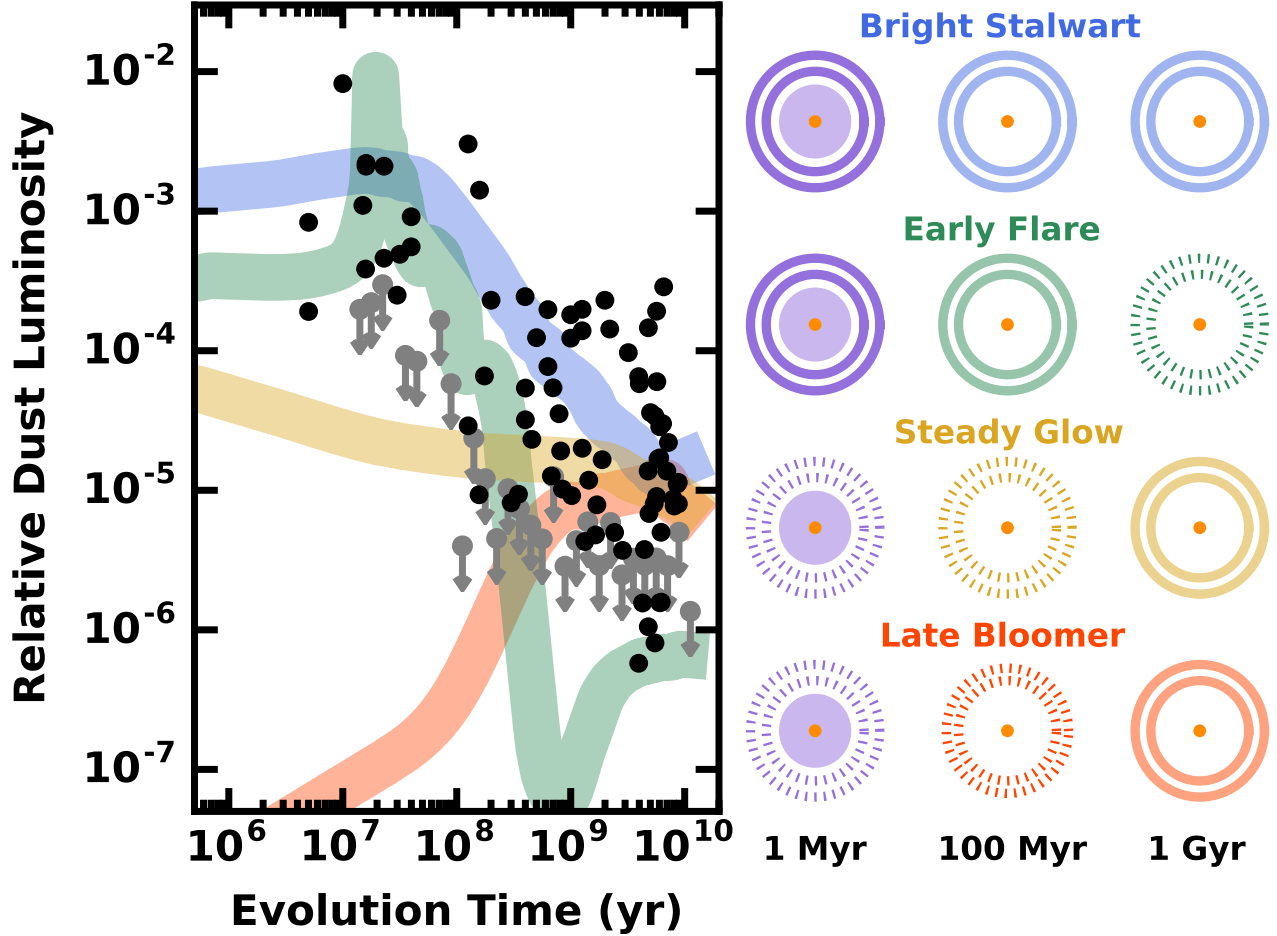


Figure 12. The four generic pathways to produce cold debris disks around solar-type stars with $a \gtrsim 40$ au. *Left Panel:* filled black circles and grey symbols plot observed dust luminosities from Fig. 3. Four thick solid curves illustrate the evolution of L_d/L_* for four types of models. In the ‘bright stalwart’ path, models with $M_0 \gtrsim 5 M_\oplus$ and $f \approx 0.1\text{--}0.5$ approximately match debris disk observations at any stellar age. Massive disks with $f \lesssim 10^{-2}$ (the ‘early flares’) match observations well for young systems with ages $\lesssim 50\text{--}100$ Myr but fade into obscurity for older stars. Massive disks with $f = 1$ (‘late bloomers’) have very small L_d/L_* until stellar ages $\gtrsim 1$ Gyr and gradually rise to an observable level at later times. In the ‘steady glow’ pathway, low mass disks have L_d/L_* just below detectable levels for stellar ages $\lesssim 100$ Myr; their relatively constant L_d/L_* over time allows them to match observations for older stars. *Right panel:* schematic evolution in the four pathways. At 1 Myr, bright stalwarts and early flares have bright rings at $a \gtrsim 40$ au; steady glow sources have low masses of solids in rings at large a that are undetectable with current instrumentation. Debris rings in late bloomers have much smaller L_d/L_* than steady glow sources and are also invisible. At 100 Myr, bright stalwarts and early flares have bright debris disks; late bloomers and steady glow sources have undetectable debris rings. At 1 Gyr, the debris rings in late bloomers, steady glow sources, and Bright stalwarts are bright; early flares have undetectable amounts of debris in rings.

Our analysis and results complement ideas discussed in the literature. In a recent examination and interpretation of the dust masses and luminosities of protoplanetary and debris disk sources, Michel et al. (2021) proposed a similar picture to the one described here: they hypothesized that debris disks are the descendants of large structured protoplanetary disks, which preserve their solids against inward radial drift through the action of dust trapping in pressure bumps. Their compact protoplanetary disk counterparts result from disks without such pressure bumps, whose solids drift inward to small disk radii. In support of their picture, they noted the similar sizes of protoplanetary disk structures (e.g., the central cavity radii of transition disks) and the blackbody radii of debris disks. However, they also offered the caveat that their protoplanetary and debris disk samples did not span the same spectral types,

with the debris disks skewed to earlier-type stars. They also asked for modeling that would support their hypothesized scenarios.

Our study complements this work by assembling protoplanetary and debris disk data sets that are matched in stellar mass and by comparing orbital distances (of protoplanetary rings and debris) and their incidence rates as a function of age. Our study also provides the detailed modeling that supports the hypothesis of Michel et al. We confirm that rings of solids with the properties inferred for protoplanetary disk rings (sizes, solid masses) can indeed evolve to produce the observed luminosities of known debris disks. Moreover, the approximately constant incidence rates of protoplanetary rings and debris disks as a function of age, when combined with our models, leaves little room for non-structured (i.e., compact) protoplanetary disks to sustain distant reservoirs of solids $> 1M_{\oplus}$. This result supports the underlying assumption in Michel et al. (and many other studies) that “what you see is what you get”, i.e., that protoplanetary disks with compact millimeter *emission* have a compact solid *mass* distribution.

Our results also overlap—but may be less compatible—with the picture described by van der Marel & Mulders (2021). If they are correct that giant planets create protoplanetary disk rings and eventually migrate in close to the star where they are detected as transiting and radial velocity planets, the radial distribution of the planetesimals that result may not be ring-like. That is, if a giant planet creates a pressure bump outside its orbit where small solids collect and planetesimals form, the pressure bump moves with the planet as it migrates inward, whereas the planetesimals are poorly coupled to the gas and are left behind. If small solids are continually captured by the pressure bump and planetesimals form, the radial distribution of planetesimals is broadened as the pressure bump migrates. If the giant planets migrate from ~ 40 au to < 1 au and planetesimals form continuously behind the migrating planet, a very broad disk of planetesimals can result (e.g., Figure 2 of Shibaike & Alibert 2020).

Such a broad distribution of planetesimals would eventually generate debris at increasing orbital distance with age (e.g., Kenyon & Bromley 2008, 2010), a trend that is not observed in the debris disk population (e.g., Najita & Williams 2005; Kennedy & Wyatt 2010; Matthews et al. 2014; Hughes et al. 2018, see also Fig. 1). In addition, if small solids migrate inward with the pressure bump, away from the planetesimals they create, the planetesimal-pebble mixture (i.e., the planetesimal mass fraction) will be altered. The scenario we explore relies on the longevity of narrow rings (of planetesimals and pebbles with an appropriate mixture) at large radii to account for the properties and demographics of the known debris disk population.

4.4. Connection to Planetesimal Formation

To place the results of Fig. 12 in the context of planetesimal formation theories, we classify each calculation in terms of the four evolutionary pathways. Fig. 13 summarizes the results. Rings with (i) $M_0 \lesssim 0.03 M_{\oplus}$ and any f or (ii) $M_0 = 0.1\text{--}0.3 M_{\oplus}$ and $f = 1$ never generate dust in amounts detectable with *Herschel* (gray symbols). More massive rings ($M_0 \gtrsim 1 M_{\oplus}$) with $f = 1$ follow the late bloomer pathway (orange symbols). Although the maximum dust luminosity of late bloomers grows with M_0 , L_d/L_{\star} never reaches detectable levels before ~ 1 Gyr.

Among the (M_0, f) combinations considered here, steady glow and bright stalwart outcomes are the most numerous. Rings with $M_0 = 0.1\text{--}1 M_{\oplus}$ and any $f \neq 1$ usually follow the steady glow pathway (gold symbols). More massive systems ($M_0 \gtrsim 3 M_{\oplus}$) with $f = 0.01\text{--}0.5$ are bright stalwarts (blue symbols). The boundary between these two outcomes depends on a_0 . When the ring is closer to the host star (e.g., $a_0 \sim 45$ au), dust intercepts a larger fraction of stellar radiation and brightens earlier in the evolutionary sequence. The dust in more distant rings (e.g., $a_0 \sim 75$ au) intercepts less stellar radiation; this lower dust luminosity falls below *Spitzer* detection limits for stellar ages of 10–100 Myr. Somewhat more massive rings, $\sim 3 M_{\oplus}$ at 75 au, are more luminous at 10–100 Myr and remain detectable throughout their evolution.

For rings with $M_0 \gtrsim 3\text{--}5 M_{\oplus}$ and $f \lesssim 10^{-2}$, the early evolution of massive solids is stochastic. Sometimes, ensembles of 1000–2000 km protoplanets undergo a series of mergers that produce several super-Earths and generate a rapid rise in L_d/L_{\star} on time scales of 10–30 Myr. However, this early flare evolution (green symbols) depletes the system of the intermediate mass solids that fuel the collisional cascade; L_d/L_{\star} then drops quickly. When mergers of protoplanets are uncommon, the system maintains a plentiful supply of intermediate mass solids, which power a more slowly evolving cascade where the dust luminosity rises and then declines more slowly. On time scales $\lesssim 50\text{--}100$ Myr, this bright stalwart evolution generates super-Mars-mass planets but not super-Earths.

A preference for the bright stalwart pathway instead of the early flare and late bloomer tracks is consistent with current understanding of planetesimal formation. In recent numerical studies of the streaming instability (e.g., Simon et al. 2016; Li et al. 2018; Abod et al. 2019; Carrera et al. 2020; Klahr & Schreiber 2020; Gole et al. 2020; Rucska &

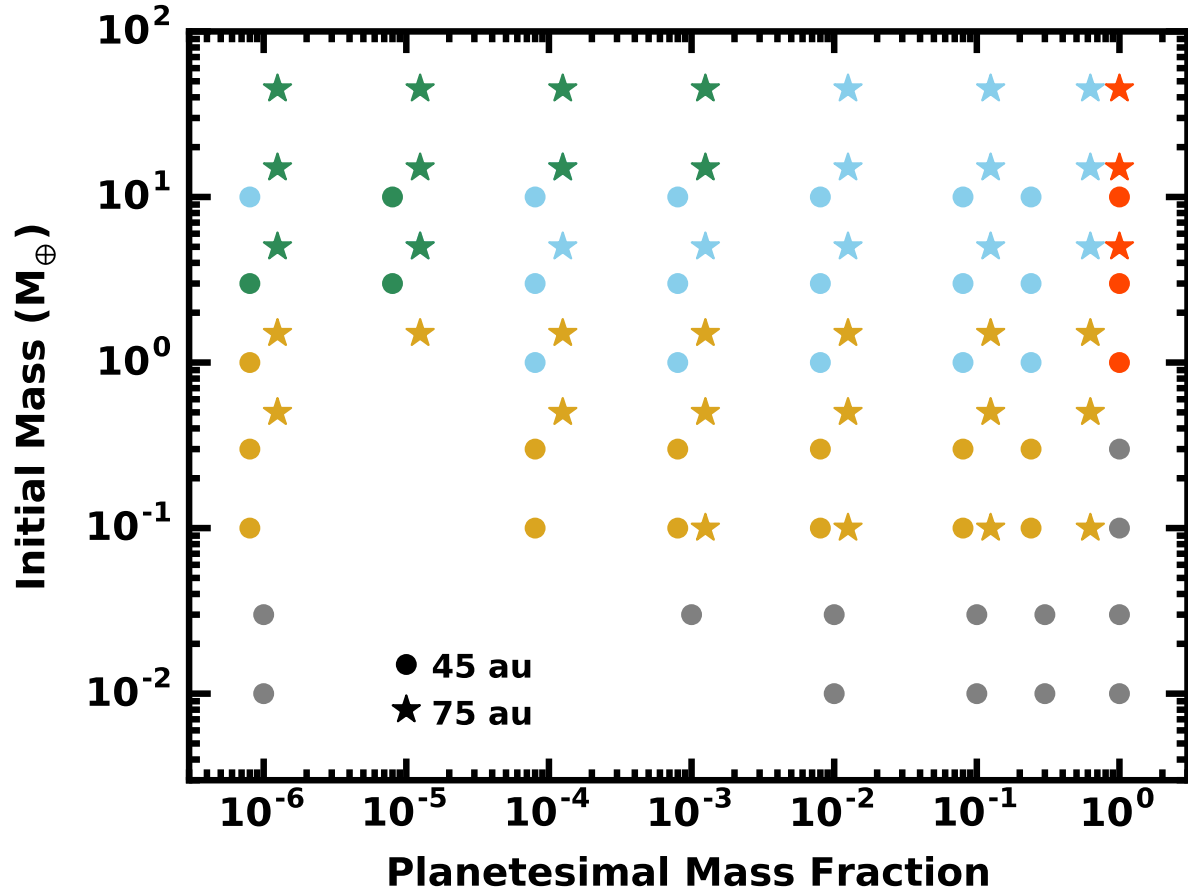


Figure 13. Classification of model results as a function of the planetesimal mass fraction f and the initial mass in solids M_0 . The legend links symbols to a_0 for each calculation. Colors refer to the four debris disk pathways summarized in Fig. 12: early flare (green), bright stalwart (blue), steady glow (gold), and late bloomer (orange). Grey symbols indicate models that failed to produce an observable L_d/L_* with *Herschel* (see also Tables 1–2). To avoid overlap, some points have been displaced horizontally.

Wadsley 2021), the planetesimal formation efficiencies required for bright stalwarts ($f \approx 0.1$ – 0.5) are more common than either $f \lesssim 10^{-2}$ (early flare) or $f \approx 1$ (late bloomer). Simulations that provide stronger constraints on f would enable better estimates of the importance of each of the four pathways outlined in Fig. 12.

The results derived here suggest a way to test numerical simulations observationally. Although rings with a broad range of f can match a specific measurement of L_d/L_* , robust detection of substructure within a ring may provide useful limits on f . For example, if bright debris disks ($L_d/L_* \sim 10^{-3}$) at an age of 10–30 Myr commonly have a gap that is wide enough to require a several Earth-mass planet, the numerical calculations discussed here require $f \lesssim 0.01$ in order to form so massive an object so quickly (Fig. 8, lower panel; Fig. 17 in the Appendix).

If future observations find a consistent lack of gaps in bright, young debris disks, the results would point to the larger $f \gtrsim 0.01$ of bright stalwarts, which can form Earth-mass planets at much later times (~ 100 Myr; Fig. 6, upper panel). As a result, finding both a lack of gaps in bright, young debris disks and robust detections of gaps in older debris disks would provide strong support for $f \gtrsim 0.01$ and the bright stalwart pathway.

4.5. Caveats and Open Questions

The calculations considered here employ standard well-tested techniques and begin with starting conditions that are consistent with observations (M_0) and theory (f). In a gaussian ring with a constant gas to dust ratio, neglect of radial drift from gas drag has little impact as drift velocities are small. The initial orbital parameters, $e = 10^{-3}$ and $i = 5 \times 10^{-4}$, are plausible; however, other options are possible. If cm-sized pebbles are well-coupled to the gas, they

would have a large vertical scale-height and a larger initial inclination than considered here (e.g., Chiang & Youdin 2010; Riols & Lesur 2018; Krapp et al. 2020). As the gas dissipates over several Myr, pebbles decouple from the gas; damping from collisions and residual gas would then act rapidly and reduce e and i to values similar to the starting conditions considered here. The growth of larger solids and the evolution of L_d/L_* in the four pathways would differ little from our description.

If interactions with the gas or other physical processes should produce smaller e and i than considered here, outcomes could change dramatically. Except for models with $f = 1$, all sequences would begin with smaller L_d/L_* . Solids in rings following the late bloomer and steady glow pathways would adjust on 10–100 Myr time scales and then follow the evolution described above. Within the bright stalwart and early flare pathways, planetesimals would have larger gravitational focusing factors and grow more rapidly. While it would take a little extra time for L_d/L_* to begin to rise, these systems might produce larger planets and brighter debris disks. The early flare tracks might be more peaked and fade more rapidly; the bright stalwart tracks might be somewhat brighter but would fade on time scales similar to those described above. In both pathways, it might be easier for high resolution observations of the debris to identify dark gaps and bright rings due to the more energetic early stages of planet formation.

Aside from including the n -body component of *Orchestra*, other changes to the approach (e.g., fragmentation parameters, number of annuli per ring, or number of mass bins per annulus) are unlikely to change the outcomes significantly. As discussed in the Appendix (section B), modifying the fragmentation parameters yields factor of two changes in L_d/L_* . Previous tests of the coagulation code demonstrate that improving the mass and spatial resolution of a calculation produces similarly small changes in outcomes as a function of evolution time (e.g., Kenyon & Bromley 2016b, 2017).

5. SUMMARY

Rings of solids at $a \gtrsim 30$ –40 au offer a way to resolve a long-standing disconnect between detailed evolutionary models of debris disks and their observed properties. The lack of a strong trend in the orbital distance of debris with age (e.g., Najita & Williams 2005; Kennedy & Wyatt 2010; Matthews et al. 2014; Hughes et al. 2018, see also Fig. 1), which is predicted by earlier generations of planet formation models, is readily explained if the parent bodies that produce the debris are initially distributed in discrete rings rather than over a broad range of orbital radii. The prominent rings that are commonly observed in T Tauri (protoplanetary) disks, which have an incidence rate similar to that of cold debris disks around low mass stars (~ 20 –25%), suggest a compelling starting point for debris disk evolution (Section 2).

We have explored the potential connection between protoplanetary rings and debris disks, using a new set of evolutionary calculations that follow the evolution of rings of solids spanning a range of initial properties. The results show that diverse evolutionary histories are possible as a function of planetesimal formation efficiency f and initial solid mass M_0 (Section 3). Depending on these parameters, rings of solids can grow Pluto-, Mars-, or super-Earth planets in 0.01–10 Gyr (Section 3.3). The resulting dust luminosity histories are also diverse and fall into four main pathways (Fig. 12): an always-bright classical evolutionary pathway that encompasses the known debris disks (“bright stalwart”); tracks that burn bright and fade fast (“early flare”); those that maintain a relatively constant, lower luminosity from 10 Myr to 10 Gyr (“steady glow”); and those that brighten dramatically at late times to a detectable luminosity (“late bloomer”). The largest objects that form via these pathways are expected to clear detectable gaps in the radial distribution of the accompanying debris (Figs. 9–10; Section 3.5).

When compared with the model tracks, the known population of bright young debris disks ($L_d/L_* \gtrsim 10^{-3}$ at 50–100 Myr) is well matched by rings that start out with high initial mass ($M_0 = 5$ –40 M_\oplus). As they evolve, these systems pass through the L_d/L_* distribution of known debris disks as a function of age, an outcome that is consistent with a large range in planetesimal formation efficiency ($f \lesssim 0.5$). Thus, if $\sim 25\%$ of stars start out with massive protoplanetary rings and follow this classical “bright stalwart” evolutionary path, we can readily account for the observed luminosities and incidence rates of debris disks over time (Section 4.2).

Although most current observations are consistent with this simple picture, the debris disk incidence rate in the 10–50 Myr age range is not well known. The true story may be more complex if the high incidence rate of cold debris disks among the small sample of F stars in the β Pic moving group is typical of 10–50 Myr old stars. A large population of such sources may indicate that a significant fraction of disks follow the “early flare” pathway, in which massive rings of solids with very small f that are also undetectable because of their very small initial scale height brighten dramatically into observable debris disks, then quickly fade below current detection limits. Future observations that

constrain the debris disk frequency and L_d/L_* of stars in the 10–50 Myr age range are needed to understand how often protoplanetary disks pursue this evolutionary pathway.

Constraints from an even earlier stage of evolution, from the Class III phase, are also important to understand the evolutionary pathways of solids in disks. The recent work of Lovell et al. (2021), which studies a small sample of Class III sources in Lupus, is a good start in this direction. Larger samples and deeper observations are needed to understand whether most Class III sources follow the approximately constant luminosity evolution of the “bright stalwart” disks at early times, and/or if disks populate the fainter “steady glow” evolutionary tracks.

This uncertainty aside, the ability of the classical “bright stalwart” pathway to explain the known debris disks appears to limit the role of the other generic pathways in producing known debris disks. The inferred strong evolutionary connection between the ~ 20 –25% of protoplanetary disks with large rings and the ~ 20 –25% of mature stars with cold debris disks implies that the majority population of compact protoplanetary disks (~ 75 –80% of all disks) leave behind only modest masses of residual solids at large radii ($\lesssim 1 M_\oplus$) and evolve primarily into mature low-mass stars without detected debris at $a \gtrsim 30$ –40 au (Fig. 4 and 12). In other words, the cold debris disks studied to date are a chapter in the history of a minority of low mass stars (Section 4.3).

We can test this interpretation by looking for dynamical evidence of the planets predicted to form under these conditions. Planets should produce gaps in the accompanying debris, which may be resolvable spatially with facilities such as the ngVLA (Section 4.2). Resolving gaps in young disks can also place constraints on the efficiency of planetesimal formation (Section 4.3). Improved debris disk demographics can also test this picture. More sensitive surveys that probe L_d/L_* down to 10^{-5} – 10^{-6} in the 10–300 Myr age range can directly constrain the extent to which disks follow the “steady glow” and “late bloomer” paths. It is also important to study larger samples of young stars (< 100 Myr) and to characterize the incidence rate of bright cold debris disks ($L_d/L_* \sim 10^{-4}$ – 10^{-2}) to infer whether they represent $\sim 20\%$ of low mass stars or a much larger fraction. A much larger fraction (Pawallek et al. 2021) would indicate a more complex situation and a possibly significant role for the “early flare” pathway.

Although the picture we have described motivates and awaits new tests, our analysis illustrates how models of the evolution of rings of solids, when combined with observational constraints on the demographics of debris disks (e.g., their incidence rate as a function of luminosity and age), can strongly constrain the global evolutionary pathways of debris disks and place constraints on current important unknowns, such as the efficiency of planetesimal formation and the masses of possible dark reservoirs of solids in young disks.

ACKNOWLEDGMENTS

We thank Meredith Hughes and Gaspard Duchêne for sharing the data from their ARAA article; Grant Kennedy for sharing summaries of the *Herschel* survey results; and Jaehan Bae and Andrea Isella for sharing some results from their upcoming review article. We also acknowledge a thorough and helpful report from an anonymous reviewer. Portions of this project were supported by the *NASA Emerging Worlds* program through grant NNX17AE24G. Useful data from the numerical calculations are available at a publicly-accessible repository (<https://hive.utah.edu/>) with the url <https://doi.org/10.7278/S50d-znrw-973k>. Other portions of this work were supported by *NASA* under Agreement No. NNX15AD94G to the “Earths in Other Solar Systems” program. The results reported herein also benefited from collaborations and/or information exchange within *NASA*’s Nexus for Exoplanet System Science (NExSS) research coordination network sponsored by *NASA*’s Science Mission Directorate.

APPENDIX

A. THE ORCHESTRA CODE

To derive the evolution of solid particles within a disk or a ring, we perform sets of numerical calculations with *Orchestra*, an ensemble of computer codes designed to track the accretion, fragmentation, and orbital evolution of solid particles ranging in size from a few microns to thousands of km (Kenyon 2002; Bromley & Kenyon 2006; Kenyon & Bromley 2008; Bromley & Kenyon 2011a, 2013; Kenyon & Bromley 2016b,a). For the calculations described here, we establish a radial grid of 28 or 56 concentric annuli distributed in equal intervals of $a^{1/2}$ between a_{in} and a_{out} . Each

annulus has 140 mass bins; the interval between adjacent bins is $\delta = m_{i+1}/m_i = 2$. The minimum particle radius is $r_{min} = 1 \mu\text{m}$; the largest possible object in the grid has a mass of roughly $50 M_{\oplus}$.

Within each calculation, solids have initial mass density ρ , orbital eccentricity e_0 , orbital inclination i_0 , and total mass M_0 . Each annulus in the grid has initial surface density of solids $\Sigma_0 \propto a^{-3/2}$ (disks) or $\Sigma_0 \propto e^{-((a-a_0)/\Delta a)^2}$ (rings). As the calculations proceed, collisions between particles modify the number and masses of objects in each mass bin. Collisional damping and gravitational interactions between solids change the orbital parameters e and i .

To evolve the size and velocity distributions of solids in time, *Orchestra* derives collision rates and outcomes with standard particle-in-a-box algorithms (Kenyon & Bromley 2012). Systems start with an initial size distribution $n(r)$. When a pair of solids collides, the mass of the merged object is

$$m = m_1 + m_2 - m_{esc} , \quad (\text{A1})$$

where m_1 and m_2 are the masses of the colliding particles. The mass of debris ejected in a collision is

$$m_{esc} = 0.5 (m_1 + m_2) \left(\frac{Q_c}{Q_D^*} \right)^{b_d} . \quad (\text{A2})$$

where $Q_c = m_1 m_2 v^2 / (m_1 + m_2)^2$ is the center-of-mass collision energy, v is the collision velocity, and the exponent b_d is a constant of order unity (e.g., Davis et al. 1985; Wetherill & Stewart 1993; Kenyon & Luu 1999; Benz & Asphaug 1999; O'Brien & Greenberg 2003; Kobayashi & Tanaka 2010; Leinhardt & Stewart 2012). The binding energy of solids, Q_D^* , is the energy require to disperse half of the combined mass, $m_1 + m_2$, to infinity:

$$Q_D^* = Q_s r^{e_s} + Q_g \rho r^{e_g} , \quad (\text{A3})$$

where $\rho = 1.5 \text{ g cm}^{-3}$ is the mass density and (Q_s, Q_g, e_s, e_b) are model parameters (e.g., Benz & Asphaug 1999; Leinhardt & Stewart 2012). In this expression, the first (second) term is the strength (gravity) component of the binding energy. We choose parameters for normal ice: $Q_s = 4 \times 10^6 \text{ erg cm}^{0.4} \text{ g}^{-1}$, $e_s = -0.4$, $Q_g = 0.3 \text{ erg cm}^{1.65} \text{ g}^{-1}$, and $e_g = 1.35$ (Schlichting et al. 2013; Kenyon & Bromley 2020).

To place the debris in the grid of mass bins, we set the mass of the largest collision fragment as

$$m_{max,d} = m_{l,0} \left(\frac{Q_c}{Q_D^*} \right)^{-b_l} m_{esc} , \quad (\text{A4})$$

where $m_{l,0} \approx 0.01\text{--}0.5$ and $b_l \approx 0\text{--}1.25$ (Wetherill & Stewart 1993; Kenyon & Bromley 2008; Kobayashi & Tanaka 2010; Weidenschilling 2010). When b_l is large, catastrophic (cratering) collisions with $Q_c \gtrsim Q_D^*$ ($Q_c \lesssim Q_D^*$) crush solids into smaller fragments. Lower mass objects have a differential size distribution $N(r) \propto r^{-q_d}$ with $q_d \approx 3\text{--}4$. After placing a single object with mass $m_{max,d}$ in an appropriate bin, we place material in successively smaller mass bins until (i) the mass is exhausted or (ii) mass is placed in the smallest mass bin. Any material left over is removed from the grid.

To follow the orbital evolution of solids, we derive collisional damping from inelastic collisions and elastic (gravitational) interactions. For inelastic and elastic collisions, we follow the statistical, Fokker-Planck approaches of Ohtsuki (1992) and Ohtsuki et al. (2002), which treat pairwise interactions (e.g., dynamical friction and viscous stirring) between all objects. We also compute long-range stirring from distant oligarchs (Weidenschilling 1989).

We assume the surface density of gas is zero throughout the grid and ignore interactions between solids and gas. Previously published calculations with *Orchestra* (e.g., Kenyon & Bromley 2008, 2009, 2010) demonstrate that gas drag tends to circularize the orbits of particles with radii $r \lesssim 1 \text{ km}$ on time scales of several Myr at 30–150 au (see Adachi et al. 1976; Weidenschilling 1977; Rafikov 2004). In parallel, dynamical friction between these particles and much larger solids gradually reduces the e and i of the larger solids. Once runaway growth begins, the largest solids then have much larger gravitational focusing factors and grow much more rapidly than ensembles of solids where gas drag is neglected (see also Youdin & Kenyon 2013). Because our interest is in the evolution of solids on Gyr time scales, the lack of gas drag probably has little impact on our results. We consider several comparisons below.

Aside from circularization of orbits, the gas causes intermediate-sized solids to drift radially relative to the gas (Adachi et al. 1976; Weidenschilling 1977; Rafikov 2004). The smallest solids drift with the gas; the largest solids are not affected by the gas. Here, we avoid the complications of evolving the surface density of the gas (e.g., Alexander &

Armitage 2009; Oka et al. 2011; Bromley & Kenyon 2011a; Martin & Livio 2012, 2014; Bitsch et al. 2015; Zhang & Jin 2015; Xiao et al. 2017; Shadmehri & Ghoreyshi 2019) and ignore radial drift of the solids. For our focus on long-term evolution, this assumption is a reasonable starting point.

Our solutions to the evolution equations conserve mass and energy to machine accuracy. Typical calculations require several 12 hr runs on a system with 56 cpus; over the 10^6 – 10^8 timesteps in a typical 2–4 Gyr run, calculations conserve mass and energy to better than one part in 10^{10} .

B. BINDING ENERGY PARAMETERS

In previous studies, Kenyon & Bromley (2008, 2010) demonstrate that outcomes of coagulation calculations are remarkably independent of initial conditions. Although the growth time for large objects scales inversely with mass, collisions rapidly erase the initial eccentricity and inclination of the solids (see also Kenyon & Bromley 2004, 2012, 2016b). The pace of growth also depends on the initial size distribution and the maximum size of the solids at the start of a calculation. However, the final radius of the largest object in an annulus is rather insensitive to these starting conditions.

Growth of the largest objects is much more sensitive to the bulk properties of solids. Solids with larger binding energy Q_D^* generate less debris during a collision and therefore grow larger with time than solids with smaller Q_D^* . In a suite of coagulation calculations at 15–150 au, weak solids reach typical sizes of 3000–7000 km in 10 Gyr (Kenyon & Bromley 2010, 2012). Stronger solids achieve radii somewhat larger than 10^4 km on similar time scales. Despite these differences in final planet radii, large changes in the binding energy produce factor of $\lesssim 2$ variations in the maximum surface area of small particles (Kenyon & Bromley 2010).

As an illustration of the sensitivity of the stellar luminosity reprocessed by small particles, L_d , we consider calculations in a single annulus at 30–60 au from the Sun (Kenyon & Bromley 2020). Calculations begin with $45 M_\oplus$ in solids. Particles have a range of sizes $r \approx 100$ –500 km; 100 km particles initially contain most of the mass. To initiate a collisional cascade at the start of the calculation, particles have initial collision velocities of 1 km s^{-1} , which guarantees that collisions among 100 km particles are destructive. Although there are no particles smaller than 100 km at the start of the calculation, destructive collisions rapidly create them.

In addition to the parameters appropriate for normal ice listed above, we perform calculations with ‘weak’ ($Q_s = 2 \times 10^5 \text{ erg cm}^{0.4} \text{ g}^{-1}$) and ‘strong’ ($Q_s = 7 \times 10^7 \text{ erg cm}^{0.4} \text{ g}^{-1}$) ice. For the gravity component of Q_D^* , we examine results for the Benz & Asphaug (1999) approach (BA, $Q_g = 2.1 \text{ erg cm}^{1.81} \text{ g}^{-1}$ and $e_g = 1.19$) and the Leinhardt & Stewart (2012) approach (LS, $Q_g = 0.3 \text{ erg cm}^{1.81} \text{ g}^{-1}$ and $e_g = 1.35$).

To have a sense of how coagulation calculations react to these choices, we briefly outline how collision outcomes depend on Q_D^* . When solids are weak (strong), they are easier (harder) to fragment during a high velocity collision. As the largest objects grow, more (fewer) collision fragments generate a faster (slower) rise in the dust luminosity. If collisional damping is important, a larger mass in small fragments may accelerate the growth of the largest objects (e.g., Kenyon & Bromley 2015, 2016a). Over time, systems of weaker solids lose somewhat more mass and contain somewhat less mass in small solids than those with stronger solids (see also Kenyon & Bromley 2016b).

Fig. 14 shows the evolution of the dust luminosity for the single annulus calculations (Kenyon & Bromley 2020). Starting with most of the mass in 100 km objects, solids have initial collision velocities of 1 km s^{-1} and no dynamical evolution. Starting conditions are set to initiate a cascade of collisions that gradually grind 100 km objects into fine dust grains that are ejected by radiation pressure from the central star (see also Wyatt 2008). For the chosen parameters, the binding energy of 100 km objects is fairly independent of Q_s , Q_g , and e_g . Collisions between pairs of these objects produce the same amount of mass in fragments; fragments also have the same size distribution. Across the five different calculations, large objects generate fragments at the same rate throughout 4.5 Gyr of evolution. Thus, the mass loss rate of the system is the same in all five calculations. After 4.5 Gyr, all systems have the same final mass in solids.

Differences arise when the 1–10 km fragments collide. At the smallest sizes in these calculations (1–10 μm), the dust luminosity depends on the rate mass flows from the fragments to smaller and smaller sizes. For systems with the same binding energy at the largest sizes, the mass flow is largest for ‘weak’ ice systems and is then progressively smaller as the bulk strength grows from weak to normal to strong (see also Wyatt et al. 2011; Kenyon & Bromley 2016b, 2017). With a constant production rate of 1–10 km fragments, strong ice systems retain a larger fraction of this mass than weak ice systems and therefore have a larger dust luminosity. In addition to the bulk strength, the mass flow down the cascade depends on the gravity component of the binding energy. For particle radii $r \gtrsim 10$ –100 m,

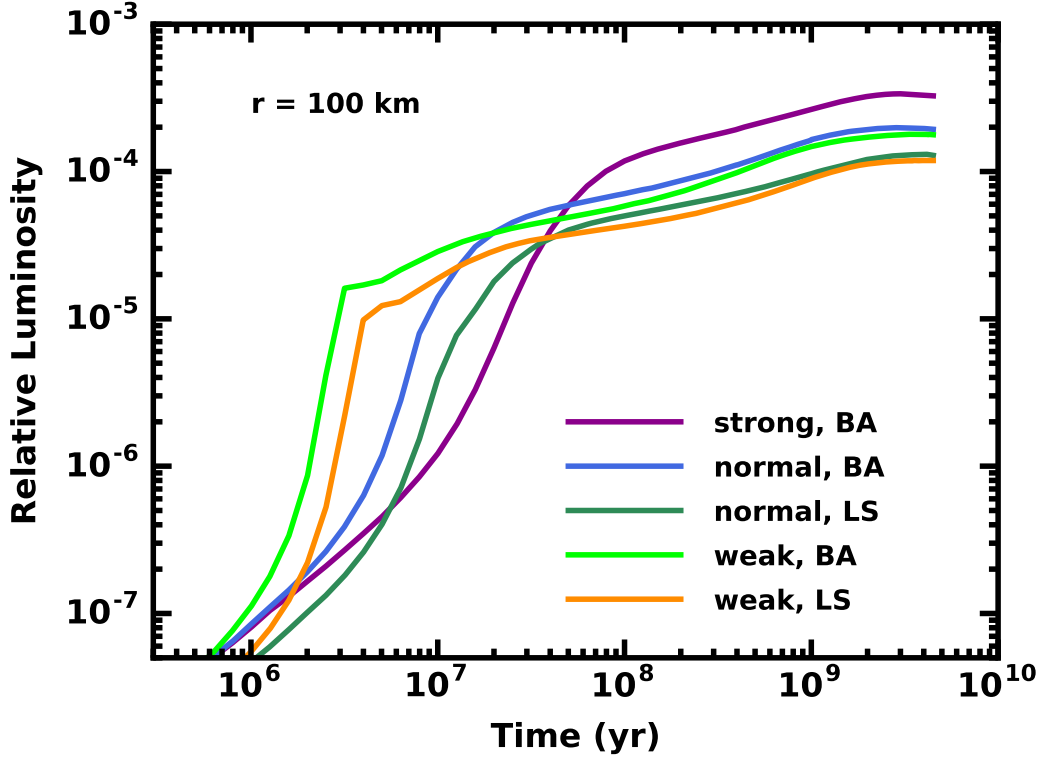


Figure 14. Time evolution of the dust luminosity for single-annulus calculations using different approaches for the binding energy of solids. In systems with ‘weak’ (‘strong’) solids, the dust luminosity rises more rapidly (slowly) than in systems with solids composed of ‘normal’ ice. At late times, solids with the BA expression for the binding energy generate more dust than solids with the LS formulation. Despite a factor of 300 spread in the strength of small objects among these approaches, the range in the dust luminosity is only a factor of three.

self-gravity dominates bulk strength. In the BA formalism, 0.1–2 km fragments are stronger than in the LS formalism. Independent of the bulk strength, the mass flow rate in a system of BA solids is then smaller than in a system of LS solids. BA systems retain more small solids and have larger L_d than LS systems.

In Fig. 14, all five systems follow the same evolution. During the first 1–10 Myr, the dust luminosity rises rapidly as large object collisions produce the first fragments which in turn produce the first small dust grains. Because weaker fragments make more dust, the luminosity rises faster in systems of weak particles. At 10–100 Myr, the rapid rise in L_d from the initial set of collisions slows. Systems enter a plateau phase, where the dust luminosity slowly rises. After 3–4 Gyr, collision rates among leftover 100 km objects begin to drop, dust production slows, and the dust luminosity falls.

At late times, the evolution of the dust luminosity falls into three groups with only a factor of ~ 3 range in L_d . Systems with the LS gravity component of the binding energy have the largest mass flow down the cascade, the smallest dust mass, and the lowest dust luminosity. Although LS systems with ‘weak’ ice initially evolve more rapidly than those with normal ice, they converge on nearly the same L_d at late times. In these two examples, collisions between 0.1–10 km objects set the mass flow rate down the cascade. For a collision velocity of 1 km s^{-1} , the bulk strength of 1 cm and smaller particles has little impact on the population of small particles. Thus, weak and normal ice calculations with the LS gravity component yield the same dust luminosity at late times.

In cascades with smaller collision velocities, the difference between weak and normal bulk strength might lead to different dust luminosities at late times. However, we expect these differences to be smaller than those from adopting different relations for the gravity component of Q_D^* .

Systems with strong ice and the BA gravity component have the smallest mass flow rate down the cascade and the largest L_d . At intermediate L_d , systems with the BA gravity component and either weak or normal ice have roughly the same L_d at late times. In these systems, the rate of mass flow down the cascade is the same as the strong BA

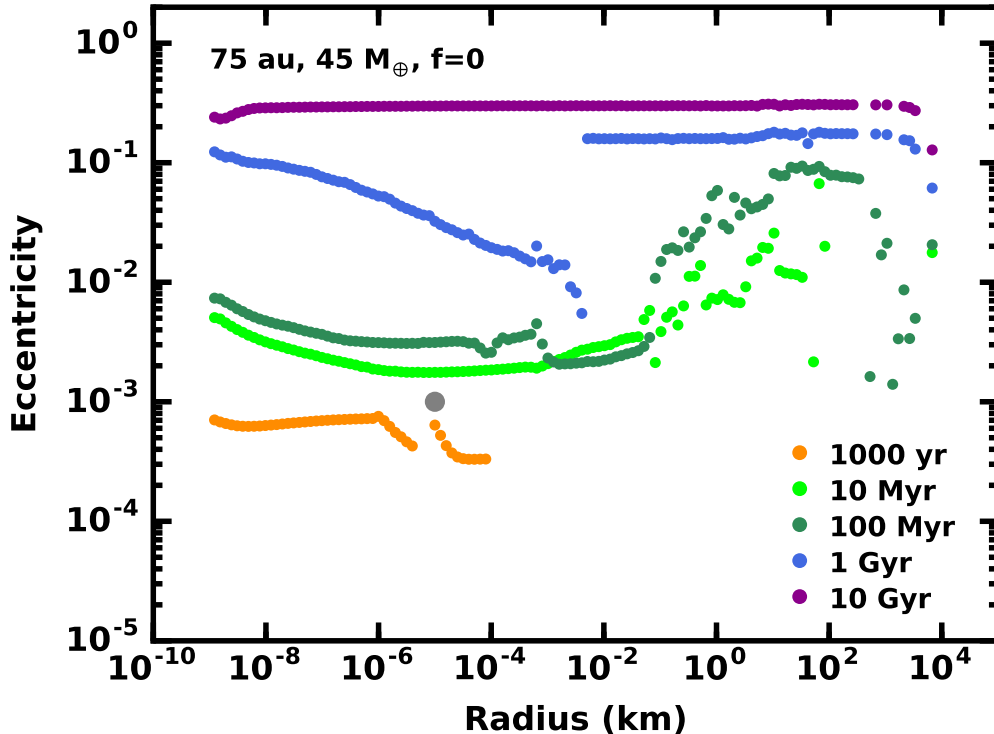


Figure 15. Snapshots of the eccentricity distribution of solids in a model with $a_0 = 75$ au, $M_0 = 45 M_\oplus$, and $f = 0$ at five epochs as listed in the legend. The large grey dot at $r = 1$ cm and $e = 10^{-3}$ shows the starting point for a system composed only of pebbles.

model from 100 km to 0.1 km. Below 0.1 km, the mass flow rate grows substantially compared to the strong BA model and reaches roughly the same level in both calculations. Thus, these models have roughly the same L_d at late times.

The small variation in maximum L_d among these calculations suggests that the binding energy parameters are not critical components for predictions of the luminosity (see also Kenyon & Bromley 2010, 2012). To facilitate comparisons with previous studies, we perform calculations with the normal ice and LS binding energy parameters. From Fig. 14, this choice produces a smaller dust luminosity than the BA binding energy parameters.

The maximum sizes of the largest objects are also somewhat smaller. Expressed another way, the normal ice bulk strength with the LS gravity component of the binding energy requires the largest mass to generate an observed maximum L_d and a maximum size for the largest objects. If the suite of calculations discussed in the main text explains observations without violating mass budget constraints (e.g., Najita & Kenyon 2014), then simulations with other choices for the binding energy parameters will match observations with lower initial masses in solids.

C. SUPPLEMENTAL RESULTS

In §3.3–3.5, we describe the time evolution of (i) the largest objects with a broad range in M_0 and f (Figs. 5–7), (ii) L_d/L_\star for selected values of M_0 and f (Fig. 8, and (iii) the radial distribution of the largest objects within the rings (Figs. 9–10). To illustrate several other aspects of the calculations, we describe the importance of collisional damping on runaway growth and show the relation between the growth time, the initial mass in solids, and f . For completeness, this section also includes Tables of results for the full set of calculations.

Eccentricity Evolution. Collisional damping, dynamical friction, and viscous stirring are central features of all calculations with $f < 1$. In a system with a mix of pebbles and planetesimals, collisions among pebbles are inelastic and circularize the orbits of pebbles (see also Goldreich et al. 2004, and references therein). Gravitational interactions between pebbles and planetesimals try to equalize the kinetic energy of both species. With the large mass ratio between pebbles and planetesimals, this process excites the eccentricities of pebbles and damps the eccentricities of planetesimals. Viscous stirring transfers angular momentum from planetesimals to pebbles, raising e for the pebbles.

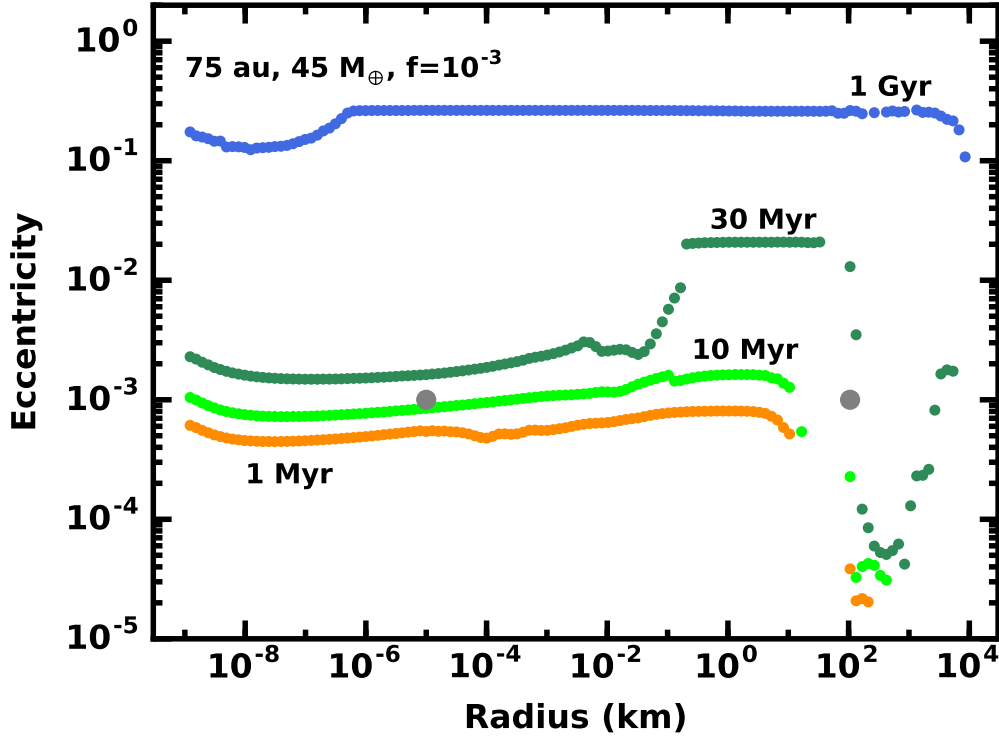


Figure 16. As in Fig. 15 for a system with $f = 10^{-3}$. The two grey dots indicate the initial e for pebbles and planetesimals.

Fig. 15 illustrates the impact of these processes for a calculation with $m_0 = 45 M_{\oplus}$ and $f = 0$ at 75 au. Initially, all pebbles have $e = 10^{-3}$. During the first 1000 yr of evolution, collisions among pebbles create 10 cm rocks and debris with $r \lesssim 1$ mm. Damping reduces the eccentricity of 1–100 μm (3–10 cm) particles to $\sim 5 - 6 \times 10^{-4}$ ($\sim 3 \times 10^{-4}$). As pebbles continue to grow, modest stirring by m-sized to km-sized planetesimals tries to raise e ; pebble damping continues to keep e low.

This balance between the smallest and largest solids in the ring continues until the runaway produces large protoplanets. At 10 Myr, several $0.25 M_{\oplus}$ planets try to stir all of the lower mass solids. Solids with $R \approx 100$ m to 10 km have little mass; protoplanets effectively stir them to larger e . Among smaller solids, damping maintains low e . At 100 Myr, the smallest solids continue to resist viscous stirring by the largest objects. Although 100 m and larger objects now have $e \sim 0.01$ – 0.1 , small solids maintain $e \sim 2 - 4 \times 10^{-3}$. Small fluctuations in e for 0.1–1 m solids result from variations of the mass contained in each mass bin: bins with smaller e have more mass.

As the evolution proceeds to 1–10 Gyr, the cascade gradually reduces the population of solids with $r \lesssim 1$ m. With less mass among pebbles, damping is less effective. For nearly all solids with $r \gtrsim 4$ m, $e \approx 0.1$ – 0.2 . Among the 1–4 m solids, damping maintains a small e . The linear rise in the e distribution from 1 m to 1 μm results from the smaller mass in these objects: damping maintains small e for 1–4 m objects but damping is less and less effective at smaller and smaller sizes. By 10 Gyr, nearly all solids have roughly the same eccentricity, $e \approx 0.3$; the largest protoplanets have $e \approx 0.1$.

Fig. 16 shows snapshots of the eccentricity evolution for a massive ring with planetesimals and pebbles. During the first Myr, growth is slow: mergers produce a few objects with $r \approx 200$ – 300 km and a swarm of smaller solids with $r \lesssim 10$ km. Collisional damping reduces e by 10–20% for the smaller solids; dynamical friction lowers e by almost a factor of 100 for the largest solids.

Over the next 30 Myr, the largest solids grow dramatically to nearly 10,000 km. With most of the mass, protoplanets stir themselves to larger and larger e . Solids with $R \approx 0.1$ – 10 km have little mass and are stirred to even larger e . Despite having less mass, pebbles maintain smaller e through collisional damping. The combined effects of damping and stirring yield an eccentricity distribution where the largest and the smallest solids have $e \approx 2 \times 10^{-3}$. Dynamical friction between pebbles and 100–300 km solids keep the larger solids at very small $e \approx 10^{-4}$.

As the collisional cascade continues, pebbles contain less and less mass. Damping and dynamical friction are less effective; viscous stirring dominates. Eccentricities for all solids grow from 10^{-3} to 0.1–0.3. At either end of the distribution, e drops by a factor of 2–3. For the large solids, dynamical friction with the rest of the solids reduces e . The smallest solids have just enough mass for damping to reduce and maintain the smaller e .

These two examples illustrate how damping among pebbles fuels runaway growth of the largest planetesimals. Without damping, pebbles have a factor of 10–100 larger eccentricity. Larger eccentricity lowers gravitational focusing factors and reduces the growth rate of the largest planetesimals. Runaway growth is delayed and is much weaker. Instead of reaching super-Earth masses on 1–10 Myr time scales, systems with no damping would produce super-Earths on 100 Myr to Gyr time scales. Delaying the runaway allows smaller planetesimals to accrete more pebbles, reducing the dust luminosity to levels below observed systems at 10–100 Myr. Once the runaway begins, a delayed collisional cascade would probably raise the dust luminosity to levels well above those observed at 1–10 Gyr. In this way, the lack of collisional damping would challenge our ability to match observations with an evolving swarm of pebbles and planetesimals.

Tables of Results. To facilitate comparisons between these calculations and those in other studies, Tables 1–2 summarize results for each calculation. The first two columns list M_0 and f . In the third column the ratio of the final mass M_f to M_0 provides a measure of the mass ejected in the form of 1 μm and smaller particles. In energetic (weak) cascades, M_f/M_0 is small (large). Rings with small f lose much more material than those with large f . The next columns measure the ability of collisional growth to concentrate solids into massive planets. The variable t_{1k} in column 4 quantifies the time scale for the growth of Pluto-mass planets; r_{max} in column 5 lists the radius of the largest protoplanet at 10 Gyr. Rings that generate super-Earths (Plutos) have large (small) r_{max} and small (large) t_{1k} . The next two columns quantify the amount of mass in the largest objects at the end of each calculation: N_L (M_L) is the number (mass) of objects with masses no less than 10% of the mass of the largest object. Sometimes, the calculation produces 1–3 large protoplanets; others with similar amounts of mass in large objects generate many much smaller protoplanets. These two quantities allow a comparison of systems with similar initial masses but very different r_{max} . Finally, the last column quantifies the maximum dust luminosity throughout the calculation. As noted in the main text, more massive rings have more luminous debris disks. This column quantifies that statement.

Among the published numerical calculations of pebble accretion, only [Shannon et al. \(2015\)](#) consider the 1–10 Gyr evolution of a swarm of pebbles and planetesimals. Starting with $M_0 = 0.01 M_\oplus$ in a ring at 42–48 au with $f = 10^{-3}$ for pebbles and km-sized planetesimals, they follow the growth of larger solids with a single annulus coagulation calculation. With a much smaller initial eccentricity $e_0 = 10^{-6}$ and binding energy for solids (Q_D^* , eq. A3), large objects in these models grow more slowly and fail to reach $r_{max} \gtrsim 1000$ km in 10 Gyr. In contrast, for the initial conditions considered here, results are similar: $r_{max} \approx 1000$ km at 1–2 Gyr and ~ 2000 km at 10 Gyr.

Growth Time as a Function of Initial Mass. To conclude this sub-section, Fig. 17 plots values for t_{1k} in Tables 1–2 as a function of M_0 for rings at 45 au (lower panel) and 75 au (upper panel). The data show clear relations between t_{1k} and M_0 . For calculations with the same f , the time scale to form Pluto-mass protoplanets scales inversely with the initial mass of solids, $t_{1k} \propto M_0^{-1}$. Among the full ensemble, there are three trends. Systems with $f = 1$ ($f \lesssim 10^{-5}$) have the longest (shortest) formation times, with a three order of magnitude difference independent of M_0 . Midway between, systems with $10^{-4} \lesssim f \lesssim 0.5$ have a factor of ~ 30 shorter (longer) formation time than those with $f = 1$ ($f \lesssim 10^{-5}$). The short formation times with small f is a hallmark of pebble accretion ([Goldreich et al. 2004](#); [Rafikov 2005](#)).

The relation for the slow growth rates for systems with $f = 1$ is straightforward to derive. In any swarm of solids, the growth time for a solid of radius r is $t_c \propto (rP/\Sigma)[1 + (v_{esc}/v)^2]^{-1}$, where P is the orbital period, Σ is the surface density of solids, v_{esc} is the escape velocity of the pair of colliding solids, and v is their collision velocity (e.g., [Safronov 1969](#); [Lissauer 1987](#); [Wetherill & Stewart 1993](#); [Goldreich et al. 2004](#); [Rafikov 2005](#); [Kenyon & Bromley 2008](#)). When $f = 1$, $v_{esc} \approx v$; $t_c \propto rP/\Sigma$. Compared to the prediction in eq. 1 derived from scaling results in [Kenyon & Bromley \(2008\)](#), the growth time scales listed in Tables 1–2 are a factor of two smaller. Analysis of each calculation suggests a simple explanation: in the ring-like geometries considered here, planetesimals are concentrated in the middle of the ring. Collisions with other planetesimals outside the central annuli tend to concentrate additional material in these annuli. This additional material increases the surface density and lowers the growth time. In the full suite of calculations, the typical increase in Σ is a factor of two, accounting for the factor of two smaller growth time.

Although the smaller growth times for systems with $f < 1$ are simple to understand, deriving a quantitative relation is a challenge. In a system of pebbles and planetesimals, damping reduces collision velocities. With $v \ll v_{esc}$,

Table 1. Results for Coagulation Calculations at 36–54 au^a

M_0 (M_\oplus)	f	M_f/M_0	t_{1k} (Myr)	r_{max} (km)	N_L	M_L (M_\oplus)	$L_{d,max}/L_\star$
0.01	1.0	1.000	...	167.5	8017	0.01	<0.01
0.01	0.3	0.979	...	257.0	98	<0.01	0.50
0.01	0.1	0.986	...	192.8	869	<0.01	0.58
0.01	10 ⁻²	0.993	...	295.1	75	<0.01	0.61
0.01	0.0	0.993	...	453.9	5	<0.01	0.62
0.03	1.0	1.000	...	199.5	23714	0.03	0.01
0.03	0.3	0.933	...	639.7	9	<0.01	1.02
0.03	0.1	0.940	...	638.3	15	<0.01	1.04
0.03	10 ⁻²	0.885	...	540.8	178	0.01	1.04
0.03	10 ⁻³	0.545	7067.8	1049.5	17	0.01	1.05
0.03	0.0	0.962	...	736.2	7	<0.01	1.05
0.10	1.0	1.000	...	206.1	78705	0.10	0.01
0.10	0.3	0.828	8851.2	1047.1	8	<0.01	2.15
0.10	0.1	0.625	3143.6	1538.2	2	0.01	2.01
0.10	10 ⁻²	0.495	5601.9	1039.9	37	0.01	1.63
0.10	10 ⁻³	0.312	2293.1	1207.8	40	0.02	2.37
0.10	0.0	0.468	1402.8	1367.7	17	0.02	2.05
0.30	1.0	1.000	...	434.5	1683	0.02	0.03
0.30	0.3	0.774	1453.5	1552.4	10	0.01	4.95
0.30	0.1	0.587	820.4	2113.5	9	0.03	4.30
0.30	10 ⁻²	0.319	659.9	2387.8	3	0.02	5.16
0.30	10 ⁻³	0.254	550.4	1836.5	12	0.03	6.34
0.30	10 ⁻⁴	0.341	95.4	2138.0	15	0.04	8.32
0.30	0.0	0.752	317.4	1625.5	5	0.01	2.51
1.00	1.0	0.998	...	517.6	6295	0.17	0.20
1.00	0.3	0.750	427.6	2128.1	11	0.05	13.30
1.00	0.1	0.547	229.0	3076.1	9	0.09	10.57
1.00	10 ⁻²	0.272	149.8	3639.2	5	0.12	17.22
1.00	10 ⁻³	0.217	129.5	2393.3	6	0.04	20.04
1.00	10 ⁻⁴	0.186	30.6	3191.5	2	0.04	26.61
1.00	0.0	0.267	39.4	2055.9	10	0.04	7.57
3.00	1.0	0.993	4818.2	2157.7	49	0.11	0.66
3.00	0.3	0.676	98.7	3243.4	3	0.06	32.21
3.00	0.1	0.520	87.5	4385.3	4	0.16	29.65
3.00	10 ⁻²	0.234	66.6	5407.5	5	0.28	65.61
3.00	10 ⁻³	0.168	51.9	5211.9	2	0.16	65.92
3.00	10 ⁻⁴	0.136	19.6	2747.9	46	0.22	86.50
3.00	10 ⁻⁵	0.094	0.6	3396.3	17	0.27	110.41
3.00	0.0	0.118	3.1	4335.1	6	0.15	44.16
10.00	1.0	0.962	716.9	4375.2	22	0.66	2.18
10.00	0.3	0.561	19.8	4168.7	20	0.50	119.40
10.00	0.1	0.468	24.9	4405.5	13	0.48	132.74
10.00	10 ⁻²	0.211	14.5	6280.6	5	0.58	154.17
10.00	10 ⁻³	0.143	15.8	6683.4	6	0.85	350.75
10.00	10 ⁻⁴	0.140	6.2	3784.4	22	0.28	239.88
10.00	10 ⁻⁵	0.091	0.3	3097.4	75	0.81	340.41
10.00	0.0	0.047	1.0	3810.7	4	0.23	127.94

^a The columns list the initial mass M_0 for each calculation, the initial fraction f of mass in large planetesimals, the ratio of the final mass in the grid M_f to the initial mass, the time scale t_{1k} to produce the first protoplanet with $r \geq 1000$ km, the final radius r_{max} of the largest planet, the final number N_L of protoplanets with masses at least as large as 10% of the mass of the largest planet, the total mass M_L in these large protoplanets, and the maximum relative dust luminosity L_d/L_\star in units of 10^{-5} .

Table 2. Results for Coagulation Calculations at 60–90 au^a

M_0 (M_\oplus)	f	M_f/M_0	t_{1k} (Myr)	r_{max} (km)	N_L	M_L (M_\oplus)	$L_{d,max}/L_*$
0.01	1.0	1.000	...	152.4	8035	0.01	<0.01
0.01	0.5	0.995	...	153.8	4121	0.01	0.12
0.01	0.1	0.998	...	153.1	914	<0.01	0.21
0.01	10 ⁻²	0.998	...	195.9	81	<0.01	0.23
0.01	0.0	1.000	...	333.4	2	<0.01	0.23
0.10	1.0	1.000	...	157.8	79616	0.10	<0.01
0.10	0.5	0.959	...	358.9	272	<0.01	1.20
0.10	0.1	0.973	...	474.2	49	<0.01	1.49
0.10	10 ⁻²	0.979	...	421.7	411	0.01	1.51
0.10	10 ⁻³	0.916	...	901.6	43	0.01	1.51
0.10	0.0	0.984	...	772.7	2	<0.01	1.51
0.50	1.0	1.000	...	209.4	433511	0.05	<0.01
0.50	0.5	0.883	...	863.0	56	0.01	4.46
0.50	0.1	0.820	4135.2	1548.8	7	0.01	4.06
0.50	10 ⁻²	0.361	3203.7	2249.1	5	0.03	3.79
0.50	10 ⁻³	0.277	2164.2	1927.5	3	0.01	3.82
0.50	10 ⁻⁴	0.207	685.6	2393.3	8	0.03	5.51
0.50	0.0	0.962	1174.9	1188.5	6	0.01	2.65
1.50	1.0	1.000	...	304.8	54576	0.29	0.07
1.50	0.5	0.804	2807.4	1745.8	21	0.02	10.54
1.50	0.1	0.659	2629.0	2118.4	5	0.03	8.79
1.50	10 ⁻²	0.217	716.6	3372.9	2	0.04	9.33
1.50	10 ⁻³	0.194	838.4	3475.4	1	0.04	10.79
1.50	10 ⁻⁴	0.180	601.2	2306.7	36	0.09	15.67
1.50	10 ⁻⁵	0.585	3.7	2685.3	6	0.06	11.04
1.50	0.0	1.000	...	304.8	54576	0.29	0.07
5.00	1.0	0.998	...	691.8	6209	0.34	0.33
5.00	0.5	0.743	401.8	1892.3	133	0.20	25.41
5.00	0.1	0.521	272.1	4405.5	7	0.20	20.51
5.00	10 ⁻²	0.229	245.7	5533.5	4	0.46	31.05
5.00	10 ⁻³	0.153	185.7	5546.3	2	0.22	50.47
5.00	10 ⁻⁴	0.106	73.5	2831.4	86	0.33	43.75
5.00	10 ⁻⁵	0.081	1.4	3507.5	22	0.27	69.34
5.00	0.0	0.256	10.1	3499.5	8	0.13	20.65
15.00	1.0	0.995	2753.5	3404.1	11	0.27	1.14
15.00	0.5	0.671	95.1	3715.4	10	0.25	62.95
15.00	0.1	0.459	79.8	5081.6	5	0.22	76.74
15.00	10 ⁻²	0.180	79.3	7979.9	4	0.92	137.72
15.00	10 ⁻³	0.116	69.2	6745.3	7	0.98	233.88
15.00	10 ⁻⁴	0.099	29.8	3435.6	45	0.40	153.82
15.00	10 ⁻⁵	0.076	0.7	3396.3	110	1.11	163.68
15.00	1.0	0.152	4.7	4285.5	11	0.34	70.63
45.00	1.0	0.979	853.7	4909.1	18	1.53	3.37
45.00	0.5	0.667	28.9	5382.7	16	0.97	195.88
45.00	0.1	0.962	...	861.0	3289	0.35	163.31
45.00	10 ⁻²	0.986	35.7	1253.1	7	0.01	103.04
45.00	10 ⁻³	0.100	19.0	9397.2	7	2.23	457.09
45.00	10 ⁻⁴	0.085	10.1	12302.7	2	2.82	941.89
45.00	10 ⁻⁵	0.083	0.3	3265.9	279	3.36	613.76
45.00	0.0	0.025	1.5	7079.5	5	0.86	309.03

^a The columns list the initial mass M_0 for each calculation, the initial fraction f of mass in large planetesimals, the ratio of the final mass in the grid M_f to the initial mass, the time scale t_{1k} to produce the first protoplanet with $r \geq 1000$ km, the final radius r_{max} of the largest planet, the final number N_L of protoplanets with masses at least as large as 10% of the mass of the largest planet, the total mass M_L in these large protoplanets, and the maximum relative dust luminosity L_d/L_* in units of 10^{-5} .

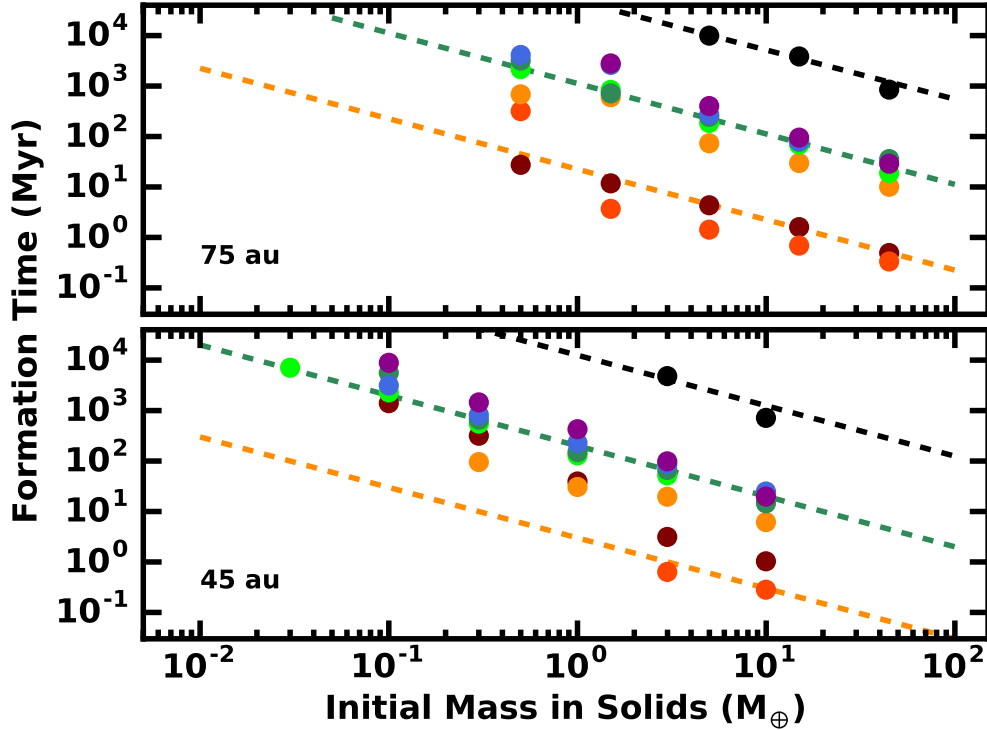


Figure 17. Evolution time t_{1k} to form objects with $r_{max} \gtrsim 1000$ km for each calculation in Table 1 (lower panel) and Table 2 (upper panel). Filled circles indicate results for $f = 1$ (black), 0.3 and 0.5 (purple), 0.1 (blue), 0.01 (dark green), 0.001 (light green), 0.0001 (orange), 0.00001 (orange-red), and 0 (maroon). Dashed lines show the relation $t_{1k} \propto M_0^{-1}$ discussed in the text.

$t_c \propto (rP/\Sigma)(v/v_{esc})^2$. To evaluate $(v/v_{esc})^2$, there are two regimes (e.g., Goldreich et al. 2004; Rafikov 2005). In the ‘dispersion regime’, collision velocities exceed the Hill velocity, $v_H = \Omega R_H$, where Ω is the angular velocity. Analytic results then yield $(v/v_{esc})^2 \propto f$. In the ‘shear regime’, $v < v_H$; then $(v/v_{esc})^2 \propto f^{1/2}$.

These theories predict the sense of the results in Tables 1–2, but not the clustering of t_{1k} for $10^{-4} \lesssim f \lesssim 0.5$ and the second cluster of results for smaller f . When f is roughly zero, growth is in the shear regime and very rapid as summarized in the main text. Larger f places growth more in the dispersion regime, where growth is somewhat slower. Our results suggest that the boundary between rapid and extremely rapid growth is $f \approx 10^{-5} - 10^{-4}$. However, current theory is insufficient to isolate this boundary. At the same time, theory suggests that the growth time should scale with f for intermediate f between 0 and 1 rather than a common growth time for a range of f . Because relating t_{1k} to the initial properties of rings of solids is not a central goal of this project, we leave a detailed investigation of this issue to a separate study.

D. COMPARISONS WITH PREVIOUS CALCULATIONS

To illustrate the impact of differences between the calculations in this paper and those in Kenyon & Bromley (2010), we consider several examples. In Kenyon & Bromley (2010), solids with radii $r \gtrsim 1$ m evolve within 64 annuli extending from an inner radius of 30 au to an outer radius of 150 au. Solids interact with a gaseous disk; gas drag circularizes orbits while radial drift removes smaller particles from the grid. Initially, the gas-to-solid ratio is roughly 1:100; during the evolutionary sequence, the gas mass declines exponentially with an e-folding time scale of 10 Myr. Although Kenyon & Bromley (2010) consider a broad range of initial conditions, here we focus on calculations starting with a mono-disperse set of solids and a total mass roughly comparable with the minimum mass solar nebula (solid and gas mass).

In the calculations for this paper, the minimum size of solids is 1 μm instead of 1 m. Interactions with gas are ignored. The smaller size allows collisional damping to play a role during the collisional cascade (e.g., Kenyon & Bromley 2015, 2016b,a, see also Figs. 15–16). When damping is important, the mass in 0.1 mm to 10 cm particles may

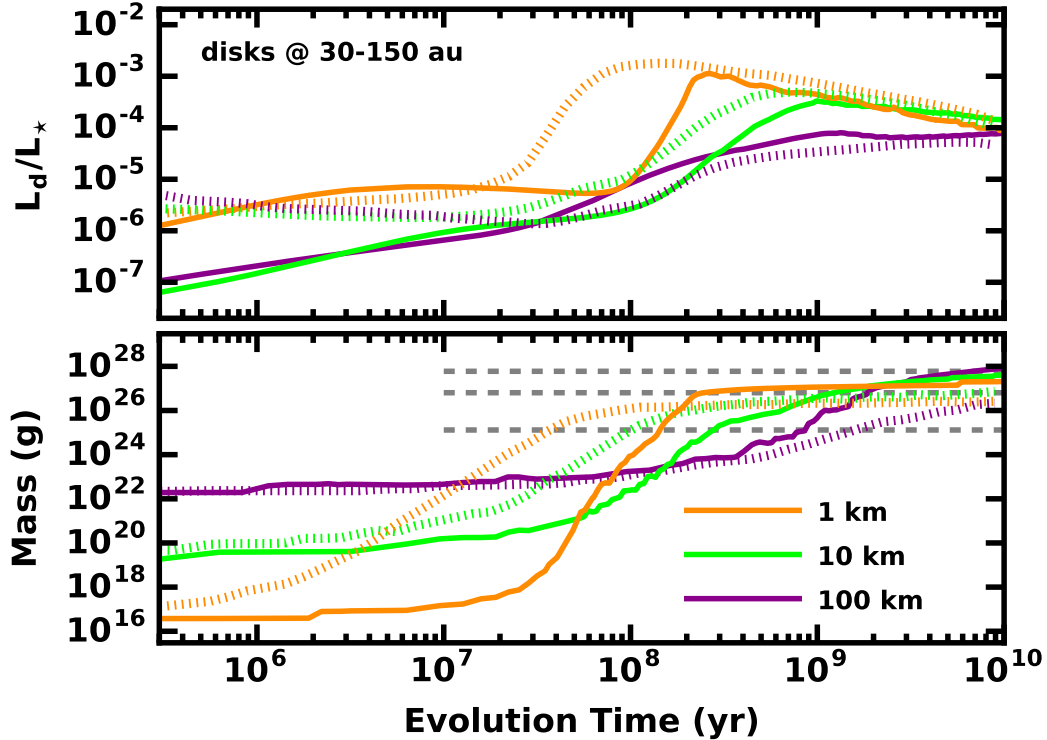


Figure 18. Evolution of the largest protoplanets (lower panel) and the relative disk luminosity L_d/L_* (upper panel) in disks of solids at 30–150 au. Dotted curves show results from [Kenyon & Bromley \(2010\)](#); solid curves follow growth with $1 \mu\text{m}$ and larger particles but without gas drag. In the lower panel, the legend indicates the initial radius for swarms of monodisperse solids; dashed lines show the masses of Pluto (lower), Mars (middle), and the Earth (upper). Systems with 1–10 km objects evolve faster when gas is included in the calculations but reach roughly the same maximum L_d/L_* . Addition of small particles in the new calculations allows planets to reach larger radii.

grow with time and allow a second phase of runaway growth for the largest particles. Thus, some solids reach larger masses than in calculations without the small particles. The lack of interactions with gas tends to slow the growth of the largest particles when their initial sizes are 1–10 km.

The lower panel of Fig. 18 compares results for calculations starting with only 1 km, 10 km, or 100 km objects. At the start of each calculation, planetesimals grow slowly. Over 1–3 Myr of evolution, gas drag gradually results in larger gravitational focusing factors for the largest objects. Despite the loss of collisional debris from radial drift, 1–10 km objects reach Pluto masses in 30–100 Myr. After this spurt, gravitational interactions between the swarm of Plutos and smaller planetesimals initiates a collisional cascade, which grinds the leftovers into smaller and smaller objects. The loss of material slows growth considerably. The largest objects approach the mass of Mars but rarely grow larger.

When gas drag is not included, 1–10 km objects grow more slowly. It takes them about three times longer to reach the mass of Pluto. Once they initiate the collisional cascade, a modest amount of mass collects in mm- and cm-sized objects which are stronger and more resistant to the cascade than m-sized and larger solids. This reservoir allows Pluto-mass objects to grow beyond the mass of Mars and reach the mass of the Earth. The time scale to reach Earth-mass is $\sim 1\text{--}2$ Gyr.

Gaseous disks have little impact on the collisional evolution of 100 km planetesimals. On time scales of 100–300 Myr, these objects reach masses comparable to Charon, Pluto’s binary partner. At this point, collisions initiate a modest collisional cascade. In calculations with no sub-meter-sized particles, the cascade effectively removes debris from the grid. Although growth continues, the largest objects reach roughly the mass of Mars on 5–10 Gyr time scales. When the small particles are included, mass removal is less efficient. Mars (Earth) mass planets then form on 1–2 Gyr (5–7 Gyr) time scales.

Despite differences in approach, the evolution of the dust luminosity is similar in the two sets of calculations (Fig. 18, upper panel). In [Kenyon & Bromley \(2010\)](#), a second calculation uses the loss rate of sub-meter-sized particles from

the main coagulation calculation to derive the time evolution of 1 μm to 1 m particles; the surface area (and thus reprocessed stellar luminosity) of these particles is therefore completely distinct from the evolution of the largest particles in the grid. In the calculations for this paper, the smallest particles evolve together with the largest particles. This approach should provide a better measure of the evolution of the dust luminosity.

The Figure illustrates that the dust luminosity follows the growth of the largest objects in each set of calculations. early on, the largest particles grow slowly; collisions generate little debris. In turn, the dust luminosity is fairly small. As planetesimals grow more rapidly, collisions produce copious amounts of dust; the dust luminosity rises in step with the growth of the largest planetesimals. As the collisional cascade proceeds, there is less and less solid mass in the grid. Growth slows; debris production declines; the dust luminosity begins to fade.

For each pair of calculations, the maximum dust luminosity correlates well with the initial sizes of planetesimals; $L_d/L_\star \approx 10^{-3}$ for 1 km planetesimals, $L_d/L_\star \approx 3 \times 10^{-4}$ for 10 km planetesimals, and $L_d/L_\star \approx 10^{-4}$ for 100 km planetesimals. The timing of this peak is earlier for systems with gas drag and 1–10 km planetesimals and is independent of gas drag for 100 km planetesimals. Independent of the approach, all of the calculations have the same dust luminosity at 10 Gyr, $L_d/L_\star \sim 10^{-4}$.

Although we do not compare these evolutionary tracks with the data in Fig. 3 for clarity, a simple comparison shows that the evolution of full disks provides a poor match to the data. At 100 Myr, these models have $L_d/L_\star \sim 10^{-5} - 10^{-3}$, as in observed systems. With $L_d/L_\star \approx 10^{-4}$ at 10 Gyr, all disk models decline much more slowly than the observations where $L_d/L_\star \sim 10^{-5}$ for most sources. As discussed in the main text, rings of solids evolve in a similar way as the observed systems.

REFERENCES

- Abod, C. P., Simon, J. B., Li, R., et al. 2019, *ApJ*, 883, 192, doi: [10.3847/1538-4357/ab40a3](https://doi.org/10.3847/1538-4357/ab40a3)
- Adachi, I., Hayashi, C., & Nakazawa, K. 1976, *Progress of Theoretical Physics*, 56, 1756
- Akeson, R. L., Jensen, E. L. N., Carpenter, J., et al. 2019, *ApJ*, 872, 158, doi: [10.3847/1538-4357/aaff6a](https://doi.org/10.3847/1538-4357/aaff6a)
- Alexander, R. D., & Armitage, P. J. 2009, *ApJ*, 704, 989, doi: [10.1088/0004-637X/704/2/989](https://doi.org/10.1088/0004-637X/704/2/989)
- Alibert, Y., Venturini, J., Helled, R., et al. 2018, *Nature Astronomy*, 2, 873, doi: [10.1038/s41550-018-0557-2](https://doi.org/10.1038/s41550-018-0557-2)
- ALMA Partnership, Brogan, C. L., Pérez, L. M., et al. 2015, *ApJL*, 808, L3, doi: [10.1088/2041-8205/808/1/L3](https://doi.org/10.1088/2041-8205/808/1/L3)
- Andrews, S. M. 2015, *PASP*, 127, 961, doi: [10.1086/683178](https://doi.org/10.1086/683178)
- Andrews, S. M., Czekala, I., Wilner, D. J., et al. 2010, *ApJ*, 710, 462, doi: [10.1088/0004-637X/710/1/462](https://doi.org/10.1088/0004-637X/710/1/462)
- Avenhaus, H., Quanz, S. P., Garufi, A., et al. 2018, *ApJ*, 863, 44, doi: [10.3847/1538-4357/aab846](https://doi.org/10.3847/1538-4357/aab846)
- Bacciotti, F., Girart, J. M., Padovani, M., et al. 2018, *ApJL*, 865, L12, doi: [10.3847/2041-8213/aadf87](https://doi.org/10.3847/2041-8213/aadf87)
- Backman, D. E., Dasgupta, A., & Stencel, R. E. 1995, *ApJL*, 450, L35, doi: [10.1086/309660](https://doi.org/10.1086/309660)
- Bae, J., Pinilla, P., & Birnstiel, T. 2018, *ApJL*, 864, L26, doi: [10.3847/2041-8213/aadd51](https://doi.org/10.3847/2041-8213/aadd51)
- Basu, S. 1998, *ApJ*, 509, 229, doi: [10.1086/306494](https://doi.org/10.1086/306494)
- Benz, W., & Asphaug, E. 1999, *Icarus*, 142, 5, doi: [10.1006/icar.1999.6204](https://doi.org/10.1006/icar.1999.6204)
- Birnstiel, T., Fang, M., & Johansen, A. 2016, *SSRv*, 205, 41, doi: [10.1007/s11214-016-0256-1](https://doi.org/10.1007/s11214-016-0256-1)
- Bitsch, B., Izidoro, A., Johansen, A., et al. 2019, *A&A*, 623, A88, doi: [10.1051/0004-6361/201834489](https://doi.org/10.1051/0004-6361/201834489)
- Bitsch, B., Johansen, A., Lambrechts, M., & Morbidelli, A. 2015, *A&A*, 575, A28, doi: [10.1051/0004-6361/201424964](https://doi.org/10.1051/0004-6361/201424964)
- Blum, J., & Wurm, G. 2008, *ARA&A*, 46, 21, doi: [10.1146/annurev.astro.46.060407.145152](https://doi.org/10.1146/annurev.astro.46.060407.145152)
- Bodenheimer, P., Stevenson, D. J., Lissauer, J. J., & D’Angelo, G. 2018, *ApJ*, 868, 138, doi: [10.3847/1538-4357/aae928](https://doi.org/10.3847/1538-4357/aae928)
- Brauer, F., Dullemond, C. P., & Henning, T. 2008, *A&A*, 480, 859, doi: [10.1051/0004-6361:20077759](https://doi.org/10.1051/0004-6361:20077759)
- Brittain, S. D., Najita, J. R., & Carr, J. S. 2019, *ApJ*, 883, 37, doi: [10.3847/1538-4357/ab380b](https://doi.org/10.3847/1538-4357/ab380b)
- Bromley, B. C., & Kenyon, S. J. 2006, *AJ*, 131, 2737, doi: [10.1086/503280](https://doi.org/10.1086/503280)
- . 2011a, *ApJ*, 731, 101, doi: [10.1088/0004-637X/731/2/101](https://doi.org/10.1088/0004-637X/731/2/101)
- . 2011b, *ApJ*, 735, 29, doi: [10.1088/0004-637X/735/1/29](https://doi.org/10.1088/0004-637X/735/1/29)
- . 2013, *ApJ*, 764, 192, doi: [10.1088/0004-637X/764/2/192](https://doi.org/10.1088/0004-637X/764/2/192)
- . 2020, *AJ*, 160, 85, doi: [10.3847/1538-3881/ab9e6c](https://doi.org/10.3847/1538-3881/ab9e6c)
- Bryden, G., Beichman, C. A., Carpenter, J. M., et al. 2009, *ApJ*, 705, 1226, doi: [10.1088/0004-637X/705/2/1226](https://doi.org/10.1088/0004-637X/705/2/1226)
- Carpenter, J. M., Bouwman, J., Mamajek, E. E., et al. 2009, *ApJS*, 181, 197, doi: [10.1088/0067-0049/181/1/197](https://doi.org/10.1088/0067-0049/181/1/197)
- Carrera, D., Simon, J. B., Li, R., Kretke, K. A., & Klahr, H. 2020, arXiv e-prints, arXiv:2008.01727, <https://arxiv.org/abs/2008.01727>

- Chalmers, D., Lacy, G., Islam, M., et al. 2020, in Society of Photo-Optical Instrumentation Engineers (SPIE) Conference Series, Vol. 11445, Society of Photo-Optical Instrumentation Engineers (SPIE) Conference Series, 114450M, doi: [10.1117/12.2562977](https://doi.org/10.1117/12.2562977)
- Chambers, J. 2021, arXiv e-prints, arXiv:2104.10704. <https://arxiv.org/abs/2104.10704>
- Chambers, J. E. 2001, *Icarus*, 152, 205
- Chambers, J. E., Wetherill, G. W., & Boss, A. P. 1996, *Icarus*, 119, 261, doi: [10.1006/icar.1996.0019](https://doi.org/10.1006/icar.1996.0019)
- Chen, K., & Lin, M.-K. 2020, *ApJ*, 891, 132, doi: [10.3847/1538-4357/ab76ca](https://doi.org/10.3847/1538-4357/ab76ca)
- Chiang, E., & Youdin, A. N. 2010, *Annual Review of Earth and Planetary Sciences*, 38, 493, doi: [10.1146/annurev-earth-040809-152513](https://doi.org/10.1146/annurev-earth-040809-152513)
- Chiang, E. I., & Goldreich, P. 1997, *ApJ*, 490, 368, doi: [10.1086/304869](https://doi.org/10.1086/304869)
- Cieza, L., Padgett, D. L., Stapelfeldt, K. R., et al. 2007, *ApJ*, 667, 308, doi: [10.1086/520698](https://doi.org/10.1086/520698)
- Cieza, L. A., Ruíz-Rodríguez, D., Hales, A., et al. 2019, *MNRAS*, 482, 698, doi: [10.1093/mnras/sty2653](https://doi.org/10.1093/mnras/sty2653)
- Corder, S., Carpenter, J. M., Sargent, A. I., et al. 2009, *ApJL*, 690, L65, doi: [10.1088/0004-637X/690/1/L65](https://doi.org/10.1088/0004-637X/690/1/L65)
- Cuzzi, J. N., Hogan, R. C., & Shariff, K. 2008, *ApJ*, 687, 1432, doi: [10.1086/591239](https://doi.org/10.1086/591239)
- D'Angelo, G., Weidenschilling, S. J., Lissauer, J. J., & Bodenheimer, P. 2014, *Icarus*, 241, 298, doi: [10.1016/j.icarus.2014.06.029](https://doi.org/10.1016/j.icarus.2014.06.029)
- . 2021, *Icarus*, 355, 114087, doi: [10.1016/j.icarus.2020.114087](https://doi.org/10.1016/j.icarus.2020.114087)
- Davis, D. R., Chapman, C. R., Weidenschilling, S. J., & Greenberg, R. 1985, *Icarus*, 63, 30. http://adsabs.harvard.edu/cgi-bin/nph-bib_query?bibcode=davis:vesta&db_key=AST
- Di Ruscio, A., Fienga, A., Durante, D., et al. 2020, *A&A*, 640, A7, doi: [10.1051/0004-6361/202037920](https://doi.org/10.1051/0004-6361/202037920)
- Dominik, C., & Decin, G. 2003, *ApJ*, 598, 626, doi: [10.1086/379169](https://doi.org/10.1086/379169)
- Dominik, C., & Tielens, A. G. G. M. 1997, *ApJ*, 480, 647, doi: [10.1086/303996](https://doi.org/10.1086/303996)
- Dullemond, C. P., Birnstiel, T., Huang, J., et al. 2018, *ApJL*, 869, L46, doi: [10.3847/2041-8213/aaf742](https://doi.org/10.3847/2041-8213/aaf742)
- Eiroa, C., Marshall, J. P., Mora, A., et al. 2013, *A&A*, 555, A11, doi: [10.1051/0004-6361/201321050](https://doi.org/10.1051/0004-6361/201321050)
- Esplin, T. L., & Luhman, K. L. 2019, *AJ*, 158, 54, doi: [10.3847/1538-3881/ab2594](https://doi.org/10.3847/1538-3881/ab2594)
- Facchini, S., van Dishoeck, E. F., Manara, C. F., et al. 2019, *A&A*, 626, L2, doi: [10.1051/0004-6361/201935496](https://doi.org/10.1051/0004-6361/201935496)
- Facchini, S., Benisty, M., Bae, J., et al. 2020, *A&A*, 639, A121, doi: [10.1051/0004-6361/202038027](https://doi.org/10.1051/0004-6361/202038027)
- Faherty, J. K., Bochanski, J. J., Gagné, J., et al. 2018, *ApJ*, 863, 91, doi: [10.3847/1538-4357/aac76e](https://doi.org/10.3847/1538-4357/aac76e)
- Gagné, J., David, T. J., Mamajek, E. E., et al. 2020, *ApJ*, 903, 96, doi: [10.3847/1538-4357/abb77e](https://doi.org/10.3847/1538-4357/abb77e)
- Gagné, J., Faherty, J. K., & Mamajek, E. E. 2018, *ApJ*, 865, 136, doi: [10.3847/1538-4357/aadaed](https://doi.org/10.3847/1538-4357/aadaed)
- Gerbig, K., Murray-Clay, R. A., Klahr, H., & Baehr, H. 2020, *ApJ*, 895, 91, doi: [10.3847/1538-4357/ab8d37](https://doi.org/10.3847/1538-4357/ab8d37)
- Gladman, B. 1993, *Icarus*, 106, 247, doi: [10.1006/icar.1993.1169](https://doi.org/10.1006/icar.1993.1169)
- Goldreich, P., Lithwick, Y., & Sari, R. 2004, *ARA&A*, 42, 549
- Gole, D. A., Simon, J. B., Li, R., Youdin, A. N., & Armitage, P. J. 2020, *ApJ*, 904, 132, doi: [10.3847/1538-4357/abc334](https://doi.org/10.3847/1538-4357/abc334)
- Gundlach, B., & Blum, J. 2015, *ApJ*, 798, 34, doi: [10.1088/0004-637X/798/1/34](https://doi.org/10.1088/0004-637X/798/1/34)
- Haffert, S. Y., Bohn, A. J., de Boer, J., et al. 2019, *Nature Astronomy*, 3, 749, doi: [10.1038/s41550-019-0780-5](https://doi.org/10.1038/s41550-019-0780-5)
- Hardy, A., Caceres, C., Schreiber, M. R., et al. 2015, *A&A*, 583, A66, doi: [10.1051/0004-6361/201526504](https://doi.org/10.1051/0004-6361/201526504)
- Hartlep, T., & Cuzzi, J. N. 2020, *ApJ*, 892, 120, doi: [10.3847/1538-4357/ab76c3](https://doi.org/10.3847/1538-4357/ab76c3)
- Hashimoto, J., Muto, T., Dong, R., et al. 2021, arXiv e-prints, arXiv:2102.05905. <https://arxiv.org/abs/2102.05905>
- Hennebelle, P., Commerçon, B., Chabrier, G., & Marchand, P. 2016, *ApJL*, 830, L8, doi: [10.3847/2041-8205/830/1/L8](https://doi.org/10.3847/2041-8205/830/1/L8)
- Hillenbrand, L. A., Carpenter, J. M., Kim, J. S., et al. 2008, *ApJ*, 677, 630, doi: [10.1086/529027](https://doi.org/10.1086/529027)
- Homma, K. A., Okuzumi, S., Nakamoto, T., & Ueda, Y. 2019, *ApJ*, 877, 128, doi: [10.3847/1538-4357/ab1de0](https://doi.org/10.3847/1538-4357/ab1de0)
- Huang, J., Andrews, S. M., Dullemond, C. P., et al. 2018, *ApJL*, 869, L42, doi: [10.3847/2041-8213/aaf740](https://doi.org/10.3847/2041-8213/aaf740)
- Hughes, A. M., Duchêne, G., & Matthews, B. C. 2018, *ARA&A*, 56, 541, doi: [10.1146/annurev-astro-081817-052035](https://doi.org/10.1146/annurev-astro-081817-052035)
- Hyodo, R., Ida, S., & Charnoz, S. 2019, *A&A*, 629, A90, doi: [10.1051/0004-6361/201935935](https://doi.org/10.1051/0004-6361/201935935)
- Ida, S., & Guillot, T. 2016, *A&A*, 596, L3, doi: [10.1051/0004-6361/201629680](https://doi.org/10.1051/0004-6361/201629680)
- Johansen, A., & Bitsch, B. 2019, *A&A*, 631, A70, doi: [10.1051/0004-6361/201936351](https://doi.org/10.1051/0004-6361/201936351)
- Johansen, A., Oishi, J. S., Mac Low, M.-M., et al. 2007, *Nature*, 448, 1022, doi: [10.1038/nature06086](https://doi.org/10.1038/nature06086)
- Johansen, A., & Youdin, A. 2007, *ApJ*, 662, 627, doi: [10.1086/516730](https://doi.org/10.1086/516730)
- Johansen, A., Youdin, A., & Mac Low, M.-M. 2009, *ApJL*, 704, L75, doi: [10.1088/0004-637X/704/2/L75](https://doi.org/10.1088/0004-637X/704/2/L75)

- Joos, M., Hennebelle, P., & Ciardi, A. 2012, *A&A*, 543, A128, doi: [10.1051/0004-6361/201118730](https://doi.org/10.1051/0004-6361/201118730)
- Kataoka, A., Tanaka, H., Okuzumi, S., & Wada, K. 2013, *A&A*, 557, L4, doi: [10.1051/0004-6361/201322151](https://doi.org/10.1051/0004-6361/201322151)
- Kelling, T., Wurm, G., & Köster, M. 2014, *ApJ*, 783, 111, doi: [10.1088/0004-637X/783/2/111](https://doi.org/10.1088/0004-637X/783/2/111)
- Kennedy, G. M., & Wyatt, M. C. 2010, *MNRAS*, 405, 1253, doi: [10.1111/j.1365-2966.2010.16528.x](https://doi.org/10.1111/j.1365-2966.2010.16528.x)
- Kenyon, S. J. 2002, *PASP*, 114, 265, doi: [10.1086/339188](https://doi.org/10.1086/339188)
- Kenyon, S. J., & Bromley, B. C. 2004, *AJ*, 127, 513, doi: [10.1086/379854](https://doi.org/10.1086/379854)
- . 2006, *AJ*, 131, 1837, doi: [10.1086/499807](https://doi.org/10.1086/499807)
- . 2008, *ApJS*, 179, 451, doi: [10.1086/591794](https://doi.org/10.1086/591794)
- . 2009, *ApJL*, 690, L140, doi: [10.1088/0004-637X/690/2/L140](https://doi.org/10.1088/0004-637X/690/2/L140)
- . 2010, *ApJS*, 188, 242, doi: [10.1088/0067-0049/188/1/242](https://doi.org/10.1088/0067-0049/188/1/242)
- . 2012, *AJ*, 143, 63, doi: [10.1088/0004-6256/143/3/63](https://doi.org/10.1088/0004-6256/143/3/63)
- . 2015, *ApJ*, 806, 42, doi: [10.1088/0004-637X/806/1/42](https://doi.org/10.1088/0004-637X/806/1/42)
- . 2016a, *ApJ*, 825, 33, doi: [10.3847/0004-637X/825/1/33](https://doi.org/10.3847/0004-637X/825/1/33)
- . 2016b, *ApJ*, 817, 51. <https://arxiv.org/abs/1512.01273>
- . 2017, *ApJ*, 839, 38, doi: [10.3847/1538-4357/aa6982](https://doi.org/10.3847/1538-4357/aa6982)
- . 2020, *The Planetary Science Journal*, 1, 40, doi: [10.3847/PSJ/aba8a9](https://doi.org/10.3847/PSJ/aba8a9)
- . 2021, *AJ*, 161, 211, doi: [10.3847/1538-3881/abe858](https://doi.org/10.3847/1538-3881/abe858)
- Kenyon, S. J., & Hartmann, L. 1987, *ApJ*, 323, 714, doi: [10.1086/165866](https://doi.org/10.1086/165866)
- Kenyon, S. J., & Luu, J. X. 1999, *AJ*, 118, 1101, doi: [10.1086/300969](https://doi.org/10.1086/300969)
- Kepler, M., Benisty, M., Müller, A., et al. 2018, *A&A*, 617, A44, doi: [10.1051/0004-6361/201832957](https://doi.org/10.1051/0004-6361/201832957)
- Klahr, H., & Schreiber, A. 2020, *ApJ*, 901, 54, doi: [10.3847/1538-4357/abac58](https://doi.org/10.3847/1538-4357/abac58)
- Kobayashi, H., & Tanaka, H. 2010, *Icarus*, 206, 735, doi: [10.1016/j.icarus.2009.10.004](https://doi.org/10.1016/j.icarus.2009.10.004)
- Kobayashi, H., Tanaka, H., Krivov, A. V., & Inaba, S. 2010, *Icarus*, 209, 836, doi: [10.1016/j.icarus.2010.04.021](https://doi.org/10.1016/j.icarus.2010.04.021)
- Kokubo, E., & Ida, S. 1995, *Icarus*, 114, 247
- . 1998, *Icarus*, 131, 171
- Krapp, L., Youdin, A. N., Kratter, K. M., & Benítez-Llambay, P. 2020, *MNRAS*, 497, 2715, doi: [10.1093/mnras/staa1854](https://doi.org/10.1093/mnras/staa1854)
- Krasnopolsky, R., & Königl, A. 2002, *ApJ*, 580, 987, doi: [10.1086/343890](https://doi.org/10.1086/343890)
- Krist, J. E., Stapelfeldt, K. R., Bryden, G., & Plavchan, P. 2012, *AJ*, 144, 45, doi: [10.1088/0004-6256/144/2/45](https://doi.org/10.1088/0004-6256/144/2/45)
- Krist, J. E., Stapelfeldt, K. R., Bryden, G., et al. 2010, *AJ*, 140, 1051, doi: [10.1088/0004-6256/140/4/1051](https://doi.org/10.1088/0004-6256/140/4/1051)
- Krivov, A. V., Müller, S., Löhne, T., & Mutschke, H. 2008, *ApJ*, 687, 608, doi: [10.1086/591507](https://doi.org/10.1086/591507)
- Krivov, A. V., & Wyatt, M. C. 2021, *MNRAS*, 500, 718, doi: [10.1093/mnras/staa2385](https://doi.org/10.1093/mnras/staa2385)
- Kruss, M., Teiser, J., & Wurm, G. 2017, *A&A*, 600, A103, doi: [10.1051/0004-6361/201630251](https://doi.org/10.1051/0004-6361/201630251)
- Kruss, M., & Wurm, G. 2020, *The Planetary Science Journal*, 1, 23, doi: [10.3847/PSJ/ab93c4](https://doi.org/10.3847/PSJ/ab93c4)
- Lambrechts, M., & Johansen, A. 2012, *A&A*, 544, A32, doi: [10.1051/0004-6361/201219127](https://doi.org/10.1051/0004-6361/201219127)
- Lambrechts, M., Morbidelli, A., Jacobson, S. A., et al. 2019, *A&A*, 627, A83, doi: [10.1051/0004-6361/201834229](https://doi.org/10.1051/0004-6361/201834229)
- Leinhardt, Z. M., & Stewart, S. T. 2012, *ApJ*, 745, 79, doi: [10.1088/0004-637X/745/1/79](https://doi.org/10.1088/0004-637X/745/1/79)
- Lenz, C. T., Klahr, H., & Birnstiel, T. 2019, *ApJ*, 874, 36, doi: [10.3847/1538-4357/ab05d9](https://doi.org/10.3847/1538-4357/ab05d9)
- Levison, H. F., Thommes, E., & Duncan, M. J. 2010, *AJ*, 139, 1297, doi: [10.1088/0004-6256/139/4/1297](https://doi.org/10.1088/0004-6256/139/4/1297)
- Li, R., Youdin, A. N., & Simon, J. B. 2018, *ApJ*, 862, 14, doi: [10.3847/1538-4357/aaca99](https://doi.org/10.3847/1538-4357/aaca99)
- . 2019, *ApJ*, 885, 69, doi: [10.3847/1538-4357/ab480d](https://doi.org/10.3847/1538-4357/ab480d)
- Lin, J. W., Lee, E. J., & Chiang, E. 2018, *MNRAS*, 480, 4338, doi: [10.1093/mnras/sty2159](https://doi.org/10.1093/mnras/sty2159)
- Lissauer, J. J. 1987, *Icarus*, 69, 249, doi: [10.1016/0019-1035\(87\)90104-7](https://doi.org/10.1016/0019-1035(87)90104-7)
- Lissauer, J. J., Hubickyj, O., D'Angelo, G., & Bodenheimer, P. 2009, *Icarus*, 199, 338, doi: [10.1016/j.icarus.2008.10.004](https://doi.org/10.1016/j.icarus.2008.10.004)
- Liu, B., & Ji, J. 2020, *Research in Astronomy and Astrophysics*, 20, 164, doi: [10.1088/1674-4527/20/10/164](https://doi.org/10.1088/1674-4527/20/10/164)
- Liu, B., Ormel, C. W., & Johansen, A. 2019, *A&A*, 624, A114, doi: [10.1051/0004-6361/201834174](https://doi.org/10.1051/0004-6361/201834174)
- Lodato, G., Dipierro, G., Ragusa, E., et al. 2019, *MNRAS*, 486, 453, doi: [10.1093/mnras/stz913](https://doi.org/10.1093/mnras/stz913)
- Löhne, T., Krivov, A. V., & Rodmann, J. 2008, *ApJ*, 673, 1123, doi: [10.1086/524840](https://doi.org/10.1086/524840)
- Long, F., Pinilla, P., Herczeg, G. J., et al. 2018, *ApJ*, 869, 17, doi: [10.3847/1538-4357/aae8e1](https://doi.org/10.3847/1538-4357/aae8e1)
- Long, F., Herczeg, G. J., Harsono, D., et al. 2019, *ApJ*, 882, 49, doi: [10.3847/1538-4357/ab2d2d](https://doi.org/10.3847/1538-4357/ab2d2d)
- Loomis, R. A., Öberg, K. I., Andrews, S. M., & MacGregor, M. A. 2017, *ApJ*, 840, 23, doi: [10.3847/1538-4357/aa6c63](https://doi.org/10.3847/1538-4357/aa6c63)
- Lovell, J. B., Wyatt, M. C., Ansdell, M., et al. 2021, *MNRAS*, 500, 4878, doi: [10.1093/mnras/staa3335](https://doi.org/10.1093/mnras/staa3335)
- Luhman, K. L. 2018, *AJ*, 156, 271, doi: [10.3847/1538-3881/aae831](https://doi.org/10.3847/1538-3881/aae831)
- Luhman, K. L., Allen, P. R., Espaillat, C., Hartmann, L., & Calvet, N. 2010, *ApJS*, 186, 111, doi: [10.1088/0067-0049/186/1/111](https://doi.org/10.1088/0067-0049/186/1/111)
- Mamajek, E. E., & Hillenbrand, L. A. 2008, *ApJ*, 687, 1264, doi: [10.1086/591785](https://doi.org/10.1086/591785)

- Marino, S., Carpenter, J., Wyatt, M. C., et al. 2018, *MNRAS*, 479, 5423, doi: [10.1093/mnras/sty1790](https://doi.org/10.1093/mnras/sty1790)
- Marino, S., Zurlo, A., Faramaz, V., et al. 2020, *MNRAS*, 498, 1319, doi: [10.1093/mnras/staa2386](https://doi.org/10.1093/mnras/staa2386)
- Marshall, J. P., Löhne, T., Montesinos, B., et al. 2011, *A&A*, 529, A117, doi: [10.1051/0004-6361/201116673](https://doi.org/10.1051/0004-6361/201116673)
- Martin, R. G., & Livio, M. 2012, *MNRAS*, 425, L6, doi: [10.1111/j.1745-3933.2012.01290.x](https://doi.org/10.1111/j.1745-3933.2012.01290.x)
- . 2014, *ApJL*, 783, L28, doi: [10.1088/2041-8205/783/2/L28](https://doi.org/10.1088/2041-8205/783/2/L28)
- Matrà, L., Marino, S., Kennedy, G. M., et al. 2018, *ApJ*, 859, 72, doi: [10.3847/1538-4357/aabcc4](https://doi.org/10.3847/1538-4357/aabcc4)
- Matsumoto, T., Hanawa, T., & Nakamura, F. 1997, *ApJ*, 478, 569, doi: [10.1086/303822](https://doi.org/10.1086/303822)
- Matsumura, S., Brasser, R., & Ida, S. 2017, *A&A*, 607, A67, doi: [10.1051/0004-6361/201731155](https://doi.org/10.1051/0004-6361/201731155)
- Matthews, B., Greaves, J., Kennedy, G., et al. 2018, arXiv e-prints, arXiv:1810.06719. <https://arxiv.org/abs/1810.06719>
- Matthews, B. C., Krivov, A. V., Wyatt, M. C., Bryden, G., & Eiroa, C. 2014, in *Protostars and Planet VI*, ed. Beuther, H., Klessen, R. S., Dullemond, C. P., & Henning, T. (The University of Arizona Press, Tucson, AZ), 521–544
- McNally, C. P., Lovascio, F., & Paardekooper, S.-J. 2021, *MNRAS*, 502, 1469, doi: [10.1093/mnras/stab112](https://doi.org/10.1093/mnras/stab112)
- Michel, A., van der Marel, N., & Matthews, B. 2021, arXiv e-prints, arXiv:2104.05894. <https://arxiv.org/abs/2104.05894>
- Montesinos, B., Eiroa, C., Krivov, A. V., et al. 2016, *A&A*, 593, A51, doi: [10.1051/0004-6361/201628329](https://doi.org/10.1051/0004-6361/201628329)
- Morbidelli, A. 2020, *A&A*, 638, A1, doi: [10.1051/0004-6361/202037983](https://doi.org/10.1051/0004-6361/202037983)
- Mordasini, C., Mollière, P., Dittkrist, K.-M., Jin, S., & Alibert, Y. 2015, *International Journal of Astrobiology*, 14, 201, doi: [10.1017/S1473550414000263](https://doi.org/10.1017/S1473550414000263)
- Najita, J., & Williams, J. P. 2005, *ApJ*, 635, 625, doi: [10.1086/497159](https://doi.org/10.1086/497159)
- Najita, J. R., & Kenyon, S. J. 2014, *MNRAS*, 445, 3315, doi: [10.1093/mnras/stu1994](https://doi.org/10.1093/mnras/stu1994)
- Nakamura, F. 2000, *ApJ*, 543, 291, doi: [10.1086/317113](https://doi.org/10.1086/317113)
- Nederlander, A., Hughes, A. M., Fehr, A. J., et al. 2021, arXiv e-prints, arXiv:2101.08849. <https://arxiv.org/abs/2101.08849>
- Nimmo, F., Kretke, K., Ida, S., Matsumura, S., & Kleine, T. 2018, *SSRv*, 214, 101, doi: [10.1007/s11214-018-0533-2](https://doi.org/10.1007/s11214-018-0533-2)
- O’Brien, D. P., & Greenberg, R. 2003, *Icarus*, 164, 334
- Ohtsuki, K. 1992, *Icarus*, 98, 20, doi: [10.1016/0019-1035\(92\)90202-I](https://doi.org/10.1016/0019-1035(92)90202-I)
- Ohtsuki, K., Stewart, G. R., & Ida, S. 2002, *Icarus*, 155, 436, doi: [10.1006/icar.2001.6741](https://doi.org/10.1006/icar.2001.6741)
- Oka, A., Nakamoto, T., & Ida, S. 2011, *ApJ*, 738, 141, doi: [10.1088/0004-637X/738/2/141](https://doi.org/10.1088/0004-637X/738/2/141)
- Okuzumi, S., Tanaka, H., Kobayashi, H., & Wada, K. 2012, *ApJ*, 752, 106, doi: [10.1088/0004-637X/752/2/106](https://doi.org/10.1088/0004-637X/752/2/106)
- Ormel, C. W., Dullemond, C. P., & Spaans, M. 2010, *ApJL*, 714, L103, doi: [10.1088/2041-8205/714/1/L103](https://doi.org/10.1088/2041-8205/714/1/L103)
- Pan, L., Padoan, P., Scalo, J., Kritsuk, A. G., & Norman, M. L. 2011, *ApJ*, 740, 6, doi: [10.1088/0004-637X/740/1/6](https://doi.org/10.1088/0004-637X/740/1/6)
- Pan, L., & Yu, C. 2020, *ApJ*, 898, 7, doi: [10.3847/1538-4357/ab9cab](https://doi.org/10.3847/1538-4357/ab9cab)
- Pawellek, N., Wyatt, M., Matrà, L., Kennedy, G., & Yelverton, B. 2021, *MNRAS*, 502, 5390, doi: [10.1093/mnras/stab269](https://doi.org/10.1093/mnras/stab269)
- Pinilla, P., Benisty, M., & Birnstiel, T. 2012, *A&A*, 545, A81, doi: [10.1051/0004-6361/201219315](https://doi.org/10.1051/0004-6361/201219315)
- Pitjeva, E. V., & Pitjev, N. P. 2018, *Celestial Mechanics and Dynamical Astronomy*, 130, 57, doi: [10.1007/s10569-018-9853-5](https://doi.org/10.1007/s10569-018-9853-5)
- Rafikov, R. R. 2001, *AJ*, 122, 2713, doi: [10.1086/323451](https://doi.org/10.1086/323451)
- . 2004, *AJ*, 128, 1348, doi: [10.1086/423216](https://doi.org/10.1086/423216)
- . 2005, *ApJL*, 621, L69, doi: [10.1086/428899](https://doi.org/10.1086/428899)
- Ricci, L., Carpenter, J. M., Fu, B., et al. 2015, *ApJ*, 798, 124, doi: [10.1088/0004-637X/798/2/124](https://doi.org/10.1088/0004-637X/798/2/124)
- Riols, A., & Lesur, G. 2018, *A&A*, 617, A117, doi: [10.1051/0004-6361/201833212](https://doi.org/10.1051/0004-6361/201833212)
- Rucska, J. J., & Wadsley, J. W. 2021, *MNRAS*, 500, 520, doi: [10.1093/mnras/staa3295](https://doi.org/10.1093/mnras/staa3295)
- Safronov, V. S. 1969, *Evoliutsiia doplanetnogo oblaka. (Evolution of the Protoplanetary Cloud and Formation of the Earth and Planets, Nauka, Moscow [Translation 1972, NASA TT F-677] (1969).* http://adsabs.harvard.edu/cgi-bin/nph-bib_query?bibcode=1969QB981.S26.....&db_key=AST
- Sallum, S., Eisner, J. A., Close, L. M., et al. 2015, *ApJ*, 801, 85, doi: [10.1088/0004-637X/801/2/85](https://doi.org/10.1088/0004-637X/801/2/85)
- Schäfer, U., Yang, C.-C., & Johansen, A. 2017, *A&A*, 597, A69, doi: [10.1051/0004-6361/201629561](https://doi.org/10.1051/0004-6361/201629561)
- Schlichting, H. E., Fuentes, C. I., & Trilling, D. E. 2013, *AJ*, 146, 36, doi: [10.1088/0004-6256/146/2/36](https://doi.org/10.1088/0004-6256/146/2/36)
- Sekiya, M., & Onishi, I. K. 2018, *ApJ*, 860, 140, doi: [10.3847/1538-4357/aac4a7](https://doi.org/10.3847/1538-4357/aac4a7)
- Shadmehri, M., & Ghoreyshi, S. M. 2019, *MNRAS*, 488, 4623, doi: [10.1093/mnras/stz2025](https://doi.org/10.1093/mnras/stz2025)
- Shannon, A., & Wu, Y. 2011, *ApJ*, 739, 36, doi: [10.1088/0004-637X/739/1/36](https://doi.org/10.1088/0004-637X/739/1/36)
- Shannon, A., Wu, Y., & Lithwick, Y. 2015, *ApJ*, 801, 15, doi: [10.1088/0004-637X/801/1/15](https://doi.org/10.1088/0004-637X/801/1/15)

- Shibaike, Y., & Alibert, Y. 2020, *A&A*, 644, A81, doi: [10.1051/0004-6361/202039086](https://doi.org/10.1051/0004-6361/202039086)
- Sibthorpe, B., Kennedy, G. M., Wyatt, M. C., et al. 2018, *MNRAS*, 475, 3046, doi: [10.1093/mnras/stx3188](https://doi.org/10.1093/mnras/stx3188)
- Simon, J. B., Armitage, P. J., Li, R., & Youdin, A. N. 2016, *ApJ*, 822, 55, doi: [10.3847/0004-637X/822/1/55](https://doi.org/10.3847/0004-637X/822/1/55)
- Simon, M., Guilloteau, S., Di Folco, E., et al. 2017, *ApJ*, 844, 158, doi: [10.3847/1538-4357/aa78f1](https://doi.org/10.3847/1538-4357/aa78f1)
- Squire, J., & Hopkins, P. F. 2018, *MNRAS*, 477, 5011, doi: [10.1093/mnras/sty854](https://doi.org/10.1093/mnras/sty854)
- . 2020, *MNRAS*, 498, 1239, doi: [10.1093/mnras/staa2311](https://doi.org/10.1093/mnras/staa2311)
- Steinpilz, T., Joeris, K., Jungmann, F., et al. 2019, *Nature Physics*, 16, 225, doi: [10.1038/s41567-019-0728-9](https://doi.org/10.1038/s41567-019-0728-9)
- Teiser, J., Kruss, M., Jungmann, F., & Wurm, G. 2021, *ApJL*, 908, L22, doi: [10.3847/2041-8213/abddc2](https://doi.org/10.3847/2041-8213/abddc2)
- Terebey, S., Shu, F. H., & Cassen, P. 1984, *ApJ*, 286, 529, doi: [10.1086/162628](https://doi.org/10.1086/162628)
- Tobin, J., Sheehan, P., Johnstone, D., & Sharma, R. 2018, arXiv e-prints, arXiv:1810.07174, <https://arxiv.org/abs/1810.07174>
- Tomida, K., Okuzumi, S., & Machida, M. N. 2015, *ApJ*, 801, 117, doi: [10.1088/0004-637X/801/2/117](https://doi.org/10.1088/0004-637X/801/2/117)
- Tscharnuter, W. M., Schönke, J., Gail, H. P., Trieloff, M., & Lüttjohann, E. 2009, *A&A*, 504, 109, doi: [10.1051/0004-6361/200912120](https://doi.org/10.1051/0004-6361/200912120)
- Ujjwal, K., Kartha, S. S., Mathew, B., Manoj, P., & Narang, M. 2020, *AJ*, 159, 166, doi: [10.3847/1538-3881/ab76d6](https://doi.org/10.3847/1538-3881/ab76d6)
- Umurhan, O. M., Estrada, P. R., & Cuzzi, J. N. 2020, *ApJ*, 895, 4, doi: [10.3847/1538-4357/ab899d](https://doi.org/10.3847/1538-4357/ab899d)
- van der Marel, N., Matthews, B., Dong, R., Birnstiel, T., & Isella, A. 2018, in *Astronomical Society of the Pacific Conference Series*, Vol. 517, *Science with a Next Generation Very Large Array*, ed. E. Murphy, 199
- van der Marel, N., & Mulders, G. D. 2021, *AJ*, 162, 28, doi: [10.3847/1538-3881/ac0255](https://doi.org/10.3847/1538-3881/ac0255)
- Vican, L. 2012, *AJ*, 143, 135, doi: [10.1088/0004-6256/143/6/135](https://doi.org/10.1088/0004-6256/143/6/135)
- Vitense, C., Krivov, A. V., Kobayashi, H., & Löhne, T. 2012, *A&A*, 540, A30, doi: [10.1051/0004-6361/201118551](https://doi.org/10.1051/0004-6361/201118551)
- Voelkel, O., Klahr, H., Mordasini, C., Emsenhuber, A., & Lenz, C. 2020, *A&A*, 642, A75, doi: [10.1051/0004-6361/202038085](https://doi.org/10.1051/0004-6361/202038085)
- Wahhaj, Z., Cieza, L., Koerner, D. W., et al. 2010, *ApJ*, 724, 835, doi: [10.1088/0004-637X/724/2/835](https://doi.org/10.1088/0004-637X/724/2/835)
- Weidenschilling, S. J. 1977, *MNRAS*, 180, 57
- . 1989, *Icarus*, 80, 179, doi: [10.1016/0019-1035\(89\)90166-8](https://doi.org/10.1016/0019-1035(89)90166-8)
- . 2010, *ApJ*, 722, 1716, doi: [10.1088/0004-637X/722/2/1716](https://doi.org/10.1088/0004-637X/722/2/1716)
- Weidenschilling, S. J., Spaute, D., Davis, D. R., Marzari, F., & Ohtsuki, K. 1997, *Icarus*, 128, 429, doi: [10.1006/icar.1997.5747](https://doi.org/10.1006/icar.1997.5747)
- Weidling, R., Güttler, C., Blum, J., & Brauer, F. 2009, *ApJ*, 696, 2036, doi: [10.1088/0004-637X/696/2/2036](https://doi.org/10.1088/0004-637X/696/2/2036)
- Wetherill, G. W., & Stewart, G. R. 1993, *Icarus*, 106, 190, doi: [10.1006/icar.1993.1166](https://doi.org/10.1006/icar.1993.1166)
- Williams, J. P., & Cieza, L. A. 2011, *ARA&A*, 49, 67, doi: [10.1146/annurev-astro-081710-102548](https://doi.org/10.1146/annurev-astro-081710-102548)
- Windmark, F., Birnstiel, T., Ormel, C. W., & Dullemond, C. P. 2012, *A&A*, 544, L16, doi: [10.1051/0004-6361/201220004](https://doi.org/10.1051/0004-6361/201220004)
- Wurm, G., & Blum, J. 1998, *Icarus*, 132, 125, doi: [10.1006/icar.1998.5891](https://doi.org/10.1006/icar.1998.5891)
- Wyatt, M. C. 2008, *ARA&A*, 46, 339, doi: [10.1146/annurev.astro.45.051806.110525](https://doi.org/10.1146/annurev.astro.45.051806.110525)
- Wyatt, M. C., Clarke, C. J., & Booth, M. 2011, *Celestial Mechanics and Dynamical Astronomy*, 111, 1, doi: [10.1007/s10569-011-9345-3](https://doi.org/10.1007/s10569-011-9345-3)
- Wyatt, M. C., & Dent, W. R. F. 2002, *MNRAS*, 334, 589, doi: [10.1046/j.1365-8711.2002.05533.x](https://doi.org/10.1046/j.1365-8711.2002.05533.x)
- Xiao, L., Niu, R., & Zhang, H. 2017, *MNRAS*, 467, 2869, doi: [10.1093/mnras/stx278](https://doi.org/10.1093/mnras/stx278)
- Yang, C. C., Johansen, A., & Carrera, D. 2017, *A&A*, 606, A80, doi: [10.1051/0004-6361/201630106](https://doi.org/10.1051/0004-6361/201630106)
- Yorke, H. W., & Bodenheimer, P. 1999, *ApJ*, 525, 330, doi: [10.1086/307867](https://doi.org/10.1086/307867)
- Youdin, A. N. 2010, in *EAS Publications Series*, Vol. 41, *EAS Publications Series*, ed. T. Montmerle, D. Ehrenreich, & A.-M. Lagrange, 187–207, doi: [10.1051/eas/1041016](https://doi.org/10.1051/eas/1041016)
- Youdin, A. N., & Goodman, J. 2005, *ApJ*, 620, 459, doi: [10.1086/426895](https://doi.org/10.1086/426895)
- Youdin, A. N., & Kenyon, S. J. 2013, *From Disks to Planets*, ed. T. D. Oswalt, L. M. French, & P. Kalas (Dordrecht: Springer Science & Business Media), 1, doi: [10.1007/978-94-007-5606-9_1](https://doi.org/10.1007/978-94-007-5606-9_1)
- Zhang, Y., & Jin, L. 2015, *ApJ*, 802, 58, doi: [10.1088/0004-637X/802/1/58](https://doi.org/10.1088/0004-637X/802/1/58)
- Zhao, B., Tomida, K., Hennebelle, P., et al. 2020, *SSRv*, 216, 43, doi: [10.1007/s11214-020-00664-z](https://doi.org/10.1007/s11214-020-00664-z)
- Zhu, Z., & Stone, J. M. 2014, *ApJ*, 795, 53, doi: [10.1088/0004-637X/795/1/53](https://doi.org/10.1088/0004-637X/795/1/53)
- Zsom, A., Ormel, C. W., Güttler, C., Blum, J., & Dullemond, C. P. 2010, *A&A*, 513, A57, doi: [10.1051/0004-6361/200912976](https://doi.org/10.1051/0004-6361/200912976)
- Zurlo, A., Garufi, A., Pérez, S., et al. 2021, *ApJ*, 912, 64, doi: [10.3847/1538-4357/abec42](https://doi.org/10.3847/1538-4357/abec42)